DEVELOPMENT OF LIGHT-ACTIVABLE SILVER NANOPARTICLES FOR ELIMINATION OF ANTIBIOTIC-RESISTANT BACTERIA AND BIOFILMS

by

Varsha Sanjay Godakhindi

A dissertation submitted to the faculty of
The University of North Carolina at Charlotte
in partial fulfillment of the requirements
for the degree of Doctor of Philosophy in
Chemistry & Nanoscale Science

Charlotte

2024

Approved by:

_____
Dr. Juan Vivero-Escoto

_____
Dr. Mariya Munir

_____
Dr. Jerry Troutman

_____
Dr. Brittany Johnson

_____
Dr. Rosario Porras-Aguilar

_____
Dr. Tsing Hua- Her

©2024
Varsha Sanjay Godakhindi
ALL RIGHTS RESERVED

ABSTRACT

VARSHA SANJAY GODAKHINDI. Development of light-activable silver nanoparticles for the elimination of antibiotic-resistant bacteria and biofilm (Under the direction of DR. JUAN L. VIVERO-ESCOTO)

With the rise in antibiotic resistance (AR) and multidrug-resistant (MDR) bacteria, there is an urgent need for novel antimicrobials that can exert antibacterial action via multiple mechanisms. Nanoparticles such as silver nanoparticles (AgNP) can be a potential alternative due to their unique optical and physiochemical properties and innate broad-spectrum antibacterial activity. AgNPs antibacterial property is associated with the release of silver ions (Ag^+), a slow process taking up to days to achieve effective antibacterial levels. Recent findings indicate combining photodynamic inactivation (PDI) with AgNP shows antibacterial synergy. This research aims to develop light-activable silver nanoparticles and investigate their light-responsive Ag^+ release kinetics to understand their role in antibacterial synergy.

Herein, protoporphyrin IX (PpIX) conjugated on the AgNP surface (PpIX-AgNP) was developed, and Ag^+ release kinetics were investigated to correlate the Ag+ release kinetics to the antibacterial synergy of PS-AgNP. These PpIX-AgNPs serve as excellent light-activated antimicrobial agents, and this antibacterial action was demonstrated in gram-positive, *Methicillin-resistant Staphylococcus aureus* (MRSA) and gram-negative, multi-drug resistant (MDR) *Escherichia coli*. The antibacterial action of this light-activated PpIX-AgNP was further modulated by adopting a dual-step irradiation strategy to ensure the controlled release of Ag^+. Finally, this research includes a preliminary study demonstrating the transport of nanoparticles within biofilms and light-activated inhibition of *Vibrio cholerae* biofilms. This research provides crucial knowledge for designing light-responsive silver-based antimicrobials for potential wound-healing applications.

ACKNOWLEDGEMENTS

First and foremost, I express my gratitude to my advisor Dr Juan Vivero Escoto for his guidance, mentorship, patience and support throughout my PhD journey. Thank you for providing me with opportunities and a research atmosphere that has helped me learn and grow as a scientist. I'll always be grateful to you for inspiring me to pursue new research ideas and bestowing confidence in me to defend and accomplish my ideas.

I would like to thank my committee members Dr Mariya Munir, Dr Jerry Troutman, Dr Rosario Porras-Aguilar and Dr Brittany Johnson, for their time and expertise. I truly appreciate your critical insights and suggestions that have improved this work.
I have been fortunate to work with great researchers who have contributed to my research. I express gratitude to Dr Adeola Sorinolu, my project partner since first semester, for helping me with the bacterial experiments for Chapter 2. My sincere thanks to Dr Xiuli Lin and Dr Rui He for their expertise and assistance with the ICP-OES instrument. I deeply appreciate the expertise and hands-on training provided by Dr Jessica Shivas with the confocal experiments. A special thank you to Anjumana Jannati Nur, and Manoj Dooda for being my collaborators in bacterial and biofilm experiments. My sincere gratitude to the staff and professors in Chemistry at UNC Charlotte. I am grateful to the funding agencies: (NIH 1R16GM145434) and UNC Charlotte Graduate Summer Fellowship.

I am thankful to the past and present members of V-lab whose infectious energy made lab a great place to come to work every day. I was fortunate to work with wonderful undergraduate students (and girl researchers), Elana Kravitz, Ashvini Dandapani, Atqiya Nafisa, and Anh Nguyen, whose help I truly appreciate. I especially want to thank Dr Mubin Tarannum and Dr Priya Vadarevu for the training sessions and eventful discussions during my early days at V-Lab.

Outside of V-lab, I am eternally grateful to Dr Adam Fessler, for always being a great friend and for troubleshooting all my queries and problems associated to my research. I want to thank Venky, Adeola, Yunesh, Yelizxa, Alex, Damian, Tamanna, Allison, Liuqing, and Mehnaz for their friendship and the conversations. I want to thank my friends in the USA: Rucha, Akash, Niharika, Rahul, Bhasker, Prerna, and Krutika for the laughs and wishes that kept my morale up.

I can't put in words the love, encouragement and support provided by my husband, Ankur. Thank you for always being my cheerleader and keeping me sane throughout the ups and downs of my PhD journey. The journey wouldn't have been worth it without your companionship. Thank you to my family filled with cousins, aunts and uncles back in India for their constant support. A special thank you to my cousin, Sourabh Sindagi, and uncle, K. Prabhakara for always believing in me. Finally, a big thank you to my parents, Sanjay Godakhindi and Gouri Godakhindi. It takes a lot of courage to let your only child go to a new place on her own and I'll always be grateful for that courage and your faith in me.

DEDICATION

This work is dedicated to my parents and Prabhakar uncle.

TABLE OF CONTENTS

LIST OF TABLES

LIST OF FIGURES

LIST OF ABBREVIATIONS

$^1O_2$	Singlet oxygen
AA	Alginic acid
Ag^+	Silver cations
$AgNO_3$	Silver nitrate
AgNP	Silver Nanoparticles
AIE	Aggregation induced emission
AMP	Antimicrobial peptides
AR	Antibiotic resistance
ARB	Antibiotic-resistant bacteria
ARG	Antibiotic resistant gene
$Ca(OH)_2$	Calcium hydroxide
Ca^{2+}	Calcium ions
CDC	Centers for disease control and prevention
Ce6	Chlorin e6
CFU	Colony forming unit
CLSM	Confocal laser scanning microscopy
ConA	Concavalin A

cysPpIX	cysteamine functionalized Protoporphyrin IX
DCM	Dichloromethane
DMA	9,10 dimethylanthracene
DMF	Dimethylformamide
DMSO	Dimethylsulfoxide
DNA	Deoxyribonucleic acid
DPBS	Dulbecco's phosphate buffer saline
eDNA	extracellular Deoxyribonucleic acid
EPS	Extracellular polymeric substance
ESBL	Extended beta-lactamase
FITC	Fluorescein isothiocyanate
FNP	Fluorescent nanoparticles
FT-IR	Fourier Transform Infrared Spectroscopy
HCl	Hydrochloric acid
HGT	Horizontal gene transfer
HNO_3	Nitric acid
ICP-OES	Inductively coupled plasma optical emission spectroscopy
KCl	Potassium chloride

MALDI-MS	Matrix-assisted laser desorption/ionization mass spectrometry
MB	Methylene blue
MDR	Multidrug Resistant
MFI	Mean fluorescent intensity
MIC	Minimum inhibitory concentrations
MIS	Multi-step irradiation setup
MOF	Metal-organic framework
MRSA	Methicillin-resistant *Staphylococcus aureus*
MTS	CellTiter 96 Aqueous Assay
NA	Numerical aperture
NaCl	Sodium Chloride
NHS-EDC	N-Hydroxysuccinimide and 1-Ethyl-3-(3-dimethylaminopropyl)carbodiimide
NIR	Near infrared
NMR	Nuclear magnetic resonance spectroscopy
NP	Nanoparticle
O_2^-	Superoxide radical
OH	Hydroxyl radical
PDI	Photodynamic inactivation

PdI	Polydispersity index
PDT	Photodynamic therapy
PEI	Polyethyleneimine
PES	Polyethersulfone
PM	Polymeric micelle
PMB	Polymyxin B
PMMA	Polymethylmethacrylate
PpIX	Protoporphyrin IX
PS	Photosensitizer
PS-AgNP	Photosensitizer silver nanoparticle conjugates
RB	Rose Bengal
ROS	Reactive oxygen species
SEM	Standard error of mean
sePpIX	succinimide ester derivative of Protoporphyrin IX
SPR	Surface plasmon resonance
TBO	Toluidine blue
TEM	Transmission electron microscopy
TPP	Tetraphenylporphyrin

TRITC	Tetramethylrhodamine
UV-Vis	Ultraviolet–visible spectroscopy
VPS	Vibrio polysaccharide
WHO	World health organization
ζ	Zeta potential
Φ_{Δ}	Singlet oxygen quantum yield

1 CHAPTER 1: INTRODUCTION

1.1 Rise of antibiotic resistance

In the 20th century, antibiotics were credited for playing a pivotal role in advancing medicine and surgery, contributing to the extension of the average US lifespan from 54.6 years to nearly 80 years [1]. Unfortunately, the declining efficacy of antibiotics and the resulting rise in antibiotic resistance (AR) has led to concerns about reverting modern medicine to a pre-antibiotic era [2]. Multiple reports from WHO and CDC have corroborated that AR is an urgent global public health threat facing humanity [3-7]. In 2019, an estimated 4.95 million deaths were associated with AR worldwide with 1.27 million deaths attributable to antibiotic resistance bacteria (ARBs) [8]. CDC has supported the prediction by some researchers that these mortality figures could rise to 10 million per year by 2050 [7, 9, 10]. Over the 21st century, a gradual rise in ARBs associated with infectious disease has made antibiotics class such as carbapenem, vancomycin, methicillin, fluoroquinolone, and cephalosporin less effective for clinical use [10]. More current studies report that in the USA the excess cost of up to ~$29,289 per patient is attributable to ARB infections [11]. The total economic burden in the USA associated with ARBs is estimated to be $20 -55 billion per year [1, 7, 12].

Typically, conventional antibiotics kill or inhibit bacteria by interfering with a specific cellular function or metabolic pathway resulting in their cell death [1, 13, 14]. Common antibiotic targets include inhibition of cell wall synthesis, cell membrane functions, protein or nucleic acid synthesis, folic acid or mycolic acid production, and other metabolic processes [12, 15]. However, multiple bacteria have evolved via mutations, selective pressure, genetic interventions horizontal gene transfer (HGT) to overcome the antibacterial action of these antibiotics, leading to antibiotic

resistance (AR). The prevalence of AR is linked to the overuse, misuse, and underuse of antibiotics in human, animal treatment, and agricultural practices [1, 16, 17]. The resistance mechanism associated with ARBs **(Figure 1.1)** includes, a) active efflux of antibiotics via efflux pumps, b) decrease in bacterial wall permeability, c) modification in the antibiotic pathway or targets, d) overexpression of antibiotic-resistant genes (ARGs) and subsequent enzymes [2, 18-20]. There is evidence of at least one mechanism of bacterial resistance to all the classes of antibiotics available [18, 21].

From the clinical perspective, ARBs entering the human body can evade the host immune response as well as many antibiotics. These persistor ARBs can also form biofilms which can delay the wound-healing process inside the body [22-24]. The AR problem is compounded by the fact that the evolution of ARB strains has been faster than the development of innovative antibiotic classes [13, 21, 25]. The antibiotics development pipeline has been unable to produce viable compounds since the 1980s, leading to a discovery void [10, 12]. As of 2023, only 97 antibacterial agents are in the clinical pipeline and only 12 among these are considered innovative by WHO [6].

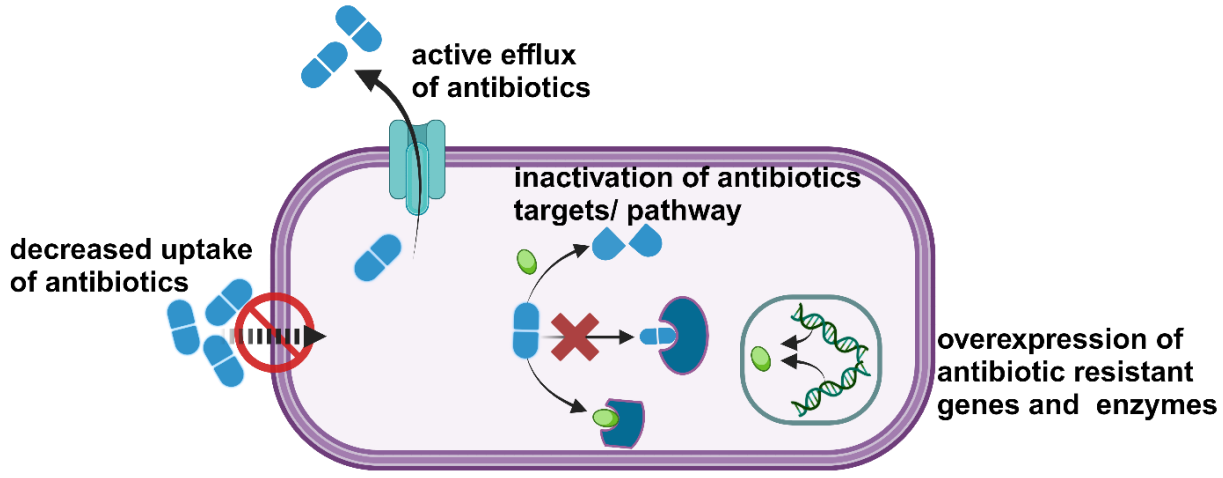

Figure 1.1 Antibiotic resistance mechanisms in bacteria.

1.2 Antibiotic resistance in biofilms

Some bacteria's ability to form communities in a polymeric matrix is one of the many mechanisms of resistance adopted by bacteria to evade antibiotics [26, 27]. IUPAC defines biofilm as "aggregates of microorganisms in which cells, that are frequently embedded within a self-produced extracellular polymeric substance (EPS), adhere to each other and/or to a surface" [28]. Biofilms, prominently growing either on indwelling medical implants or dead/live tissue, account for up to 80% of all human bacterial infections contributing to the high mortality rates [29]. They are the leading cause of delayed wound healing, exacerbating chronic wounds and related infections. The development of biofilm is divided into four stages: initial adhesion, early biofilm formation, biofilm maturation, and dispersion [30]. Adhesion molecules assist in the initial interaction with the surface followed by bacterial cell division and production of EPS. The matrix matures as bacteria multiply providing crucial architectural support to the biofilm [31]. Small channels inside mature EPS transport nutrients, metabolic waste, and water [32]. Post maturation, some bacteria escape the EPS (due to environmental or internal factors) and disperse promoting the formation of new biofilms at a different location [33]. Bacteria outside the biofilm, which may or may not originate from the biofilm, are called as planktonic bacteria [34]. In biofilms, EPS serves as a physical barrier against the entry and antibacterial action of antibiotics. Bacteria within a biofilm are 1000 times more tolerant to antibiotics and require much higher doses for treatment. This contributes to the aggressive use of antibiotics, which may lead to potential new resistance [27, 35, 36].

1.3 Photodynamic inactivation

Photodynamic therapy is a century-old technique that has been applied for anti-cancer therapy, especially melanoma [37]. Researchers in the late 1960s successfully demonstrated that PDT showed antimicrobial activity in gram-positive bacteria [38-40]. Photodynamic inactivation (PDI) is

a non-antibiotic option to eliminate pathogens by using light excitation of photosensitizers (PSs) in the presence of molecular oxygen to generate reactive oxygen species (ROS) such as singlet oxygen ($^1O_2$), superoxide (O_2^-) and hydroxyl radicals (OH) [40-43]. Light excitation (wavelength corresponding to the PS's absorption peak) of any PS molecule to an excited electronic state, is generally followed by fluorescence. In PDI, the excited singlet state of PS undergoes an electronic transition (spin-orbital) to a triplet state, a process called intersystem crossing, where it can undergo one of two reaction pathways i.e. a) Type I pathway, which involves electron transfer between the triplet state photosensitizer molecule and nearby molecules, such as water or biological molecules, to produce a wide range of reactive oxygen species (ROS) and radical ions; b) Type II process that involves energy transfer between the triplet state photosensitizer and molecular oxygen, which has a triplet ground state, resulting in the generation of highly reactive singlet oxygen ($^1O_2$) [41, 44]. The ROS and $^1O_2$ are highly reactive and can nonspecifically attack the cellular membrane, essential enzymes, and cellular nucleic acids, inducing bacterial cell death via oxidative stress [44, 45]. The broad-spectrum antibacterial action serves as an advantage over antibiotics since the development of resistance to photochemical reactions is unlikely [40]. The ROS generation in PDI has shorter lifetimes and a close association with PS and bacteria is crucial to initiate cell death mechanisms [38, 40]. Studies have reported that cationic PSs are more effective at PDI than anionic PSs [40, 46]. In biofilms, cationic PS such as methylene blue, toluidine blue O, phenothiazinium, phthalocyanines have shown 3-6 log inactivation with up to 80% EPS reduction reported [42, 47]. A broad spectrum of cationic PSs as a topical strategy to treat chronic wounds showed a significant reduction in bacterial load in a randomized Phase II clinical trial [48]. PDI can be a viable alternative to antibiotics for both treatment against ARBs and biofilms.

1.4 Role of nanoparticles as antibacterial agents

The rapid decline in antibiotic efficacy against ARBs has led researchers to look for innovative antibacterial alternatives with high antibacterial efficiency and low drug-resistance risks. These non-antibiotic approaches include antimicrobial peptides (AMPs), antibacterial oligonucleotides, monoclonal antibodies, bacteriophages, metal-organic frameworks (MOFs), nanozymes, and nanoparticles [12, 49-52]. Among these, nanoparticles (NPs) have recently aroused great interest as a treatment option for ARBs, owing to their small size, large surface area to volume ratio, surface-altering chemical functionalization, and unique optical properties [12, 22, 53]. These materials show different antibacterial mechanisms than traditional antibiotics and have a lower risk of inducing bacterial resistance.

A nanoparticle has at least one dimension in the nanometer range (1- 100 nm). These NPs show different antibacterial mechanisms than traditional antibiotics and have a lower risk of inducing bacterial resistance. Thus, it holds great promise to employ nanomaterials as an alternative to antibiotics to eliminate drug-resistant bacteria. Nanomaterial's role in antibacterial applications can be categorized into a) Antibacterial nanoparticles such as metal nanoparticles with innate antibacterial properties; b) Nanoparticles aiding delivery of antimicrobials, where they serve as carriers or protective agents.

1.5 Silver Nanoparticles (AgNP) and its antibacterial properties

AgNPs can be synthesized by reducing silver salts to generate stable AgNPs of variable nanostructures [54, 55]. This approach requires a silver precursor, a reducing agent (chemical or biological), and a stabilizing agent to generate colloidal AgNPs. The chemical-reducing agents include sodium citrate, sodium borohydride, ascorbic acid, tannic acid, and glucose [56]. Biological

reducing agents such as bacteria, fungi, and plant extracts allow for exploring environmentally friendly synthetic methods [57].

The antibacterial property of silver, in all its ionic forms, has been known since ancient times and commercially used as "colloidal silver" [58]. Silver cations (Ag^+) are highly reactive species and can effectively bind to various proteins, inducing structural changes in the cells of bacteria and causing their death. Ag^+ can also interfere with the DNA replication process and disassembly of ribosome subunits, resulting in cell death [57, 58]. The antibacterial action of AgNPs is closely associated with the release of Ag^+ ions. However, AgNPs offer unique advantages over bulk silver such as small size, increased surface area to volume ratio, and surface functionalization that allow better interaction with the bacteria and its cellular components [54, 57-59]. AgNPs also exhibit unique optical and catalytic properties. In effect, one can say that AgNPs have a higher antibacterial activity than colloidal silver, whereby the antibacterial properties are attributed to both the physiochemical properties and the elution of Ag^+ [59, 60]. AgNPs are known to kill bacteria via multiple mechanisms (as seen in **Figure 1.2**), such as disrupting the bacterial cell wall, interfering with the metabolic processes, deactivating the enzymes, DNA damage, and generating ROS thereby increasing oxidative stress [54, 58].

The physicochemical properties of AgNPs, such as size, shape, and surface charge, play a crucial role in their antibacterial action. Several studies have confirmed that smaller AgNPs of size < 30 nm have a superior antibacterial effect than larger AgNPs [54, 57, 58, 61]. Some reports have correlated the size (5-30 nm) to the dissolution of AgNPs into Ag^+ ions, which enhances the antibacterial action of AgNPs [54, 62, 63]. Other studies have suggested that AgNPs with cubic-, plate- and rod-shape perform better as antibacterial agents than their spherical counterparts due to the presence of high atom density facets [62-65]. Nevertheless, other reports have suggested that AgNPs

with spherical shapes with increased surface area result in a higher release of Ag^+, making these nanoparticles better antibacterial candidates [66, 67]. Therefore, the impact of AgNPs' shape on their bactericidal activity is still under investigation. On the other hand, AgNPs with positive surfaces have shown a more significant antibacterial effect, presumably due to the increased interaction of AgNPs with the surface of bacteria [54]. It should be noted that the colloidal stability of AgNPs also plays a crucial role wherein lower stability is associated with aggregation, which subsequently reduces the antibacterial activity of AgNPs [68, 69].

Despite these advantages, the key skepticism associated with any antimicrobials is their decreased efficacy over time due to the development of resistance. There have been studies that have identified the elimination of Ag^+ via efflux pumps or reduction of Ag^+ to its less toxic Ag^0 oxidation state as potential resistance mechanisms [70, 71]. It should be noted that most studies attribute AgNP resistance to the premise that AgNPs serve only as reservoirs for Ag^+ and their elimination drives the AgNP resistance. However, as described above in **Figure 1.2**, AgNPs use mechanisms other than releasing Ag^+ to eliminate bacteria. Studies have demonstrated that bacteria can develop resistance against AgNP post-repeated exposure by inducing their aggregation at bacterial surfaces. In gram-negative bacteria, it was observed that repeated exposure led to the development of adhesive flagella that induce the aggregation of AgNPs, reducing their bioavailability [72, 73]. Nevertheless, unlike antibiotics, the AgNP resistance mechanism in bacteria has not yet been associated with a genetic origin [74].

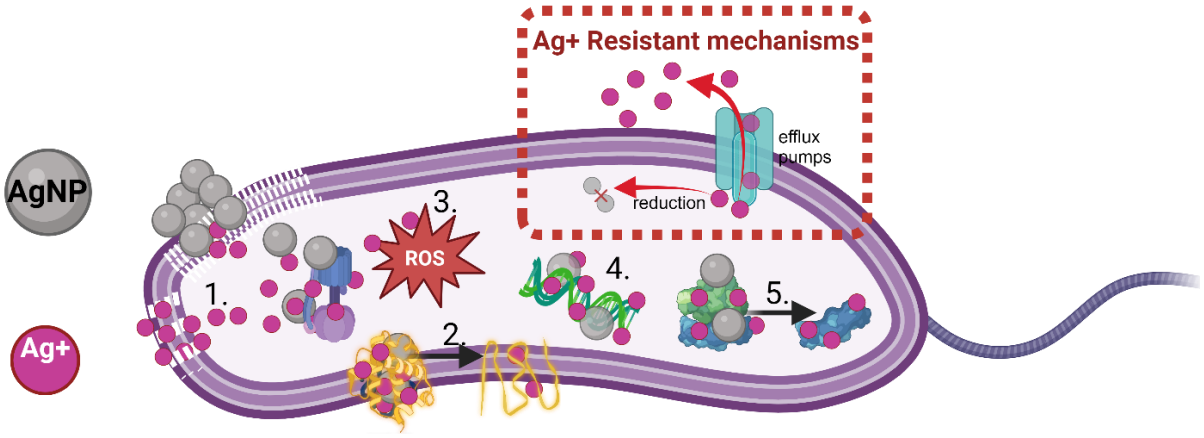

Figure 1.2 The antibacterial mechanisms of AgNP and Ag^+ ions are: 1. Binding and disruption of the cell membrane, 2. Denaturation of thiol-containing protein on the cellular membrane, 3. Interference with the intracellular metabolic pathways and ROS generation, 4. Interfering with the DNA replication process, 5. Disassembly of the ribosomal subunit. Ag^+ resistance in bacteria is associated with the reduction of Ag^+ to less toxic forms and the elimination of intracellular Ag^+ via efflux pumps.

1.6 Combination of PDI and AgNP

AgNPs are among the most used materials worldwide due to their well-known antibacterial activity, which makes them a promising alternative to antibiotics. However, there is a gap in the literature on the antibacterial mechanisms of AgNPs. Moreover, bacterial resistance against AgNPs is growing and is a significant concern. The widespread use of AgNPs is associated with delayed and moderate antibacterial effects, due to the slow release of Ag^+ and improper colloidal stability in biological environments [54, 62]. Additionally, it is important to accelerate the Ag^+ release in a controlled manner to combat any unnecessary cytotoxic effects [60, 75]. Therefore, there is a need to develop novel technologies that combine AgNPs with other approaches to eliminate pathogens efficiently. One of the key advantages of NPs (in this case, AgNP) is that their unique

physiochemical properties allow the combining of multiple antibacterial modes into a single entity. This way, the antimicrobial potency of AgNPs can be increased in a combinatorial system. Multiple reports show that AgNP combined with photodynamic inactivation (PDI) demonstrates antibacterial synergy.

Photosensitizers (PS) are highly reactive to light and can attack the cellular membrane, essential enzymes, and cellular nucleic acids, leading to bacteria cell death by oxidative stress [44, 45]. Generally, NPs are combined with PDI platforms to increase the delivery efficiency of the PSs via surface conjugation [40, 46, 49]. However, AgNPs conjugated/ combined with PS offer an additional advantage in this context due to the increased Ag^+ release and increased ROS generation. The increase in Ag^+ is associated with the generation of an oxidative environment near the AgNP surface [76, 77]. This allows for light-controlled generation of Ag^+ from AgNPs at levels effective enough for bacterial killing but confers minimal toxicity in humans. Another added advantage of using a combination system of PDI and AgNPs with multiple antibacterial mechanisms is that the development of resistance against them is unlikely [53].

The optical properties of AgNPs play a crucial role in exploring the light-mediated antibacterial properties of AgNPs. AgNPs are plasmonic nanoparticles that can generate free electrons post visible light irradiation as a result of their surface plasmon resonance (SPR) effect [78-80]. The SPR wavelength depends on the nanoparticle's size and shape; in the case of AgNPs, it is in the 400-500 nm range. Researchers have generated different shapes of AgNPs to extend this wavelength range to near-infrared (NIR) regions. Bourgonje et al., in a recent report, demonstrated the phototherapeutic activity of triangular AgNPs (tAgNPs) and decahedral AgNPs (dAgNPs) under NIR and blue LED light [78]. These LED lights were selected to overlap with the SPR peak of the respective AgNPs, i.e. tAgNPs showing high absorbance at 800 nm and dAgNPs showing peak

absorbance at 500 nm. In *S.aureus* and *E.coli*, tAgNPs showed exceptional >9 log reduction in bacteria at 20 ppm post 1 min and 15 min NIR irradiation, respectively. This antibacterial action was dependent on concentration and irradiation time, with ~4 logs and ~9 log reduction achieved for 5 ppm and 10 ppm after 15 min of NIR irradiation. In *E.coli*, dAgNPs reached only a 5 log reduction at 20 ppm concentration after 1 min blue light irradiation, whereas dAgNP and tAgNP performed the same in *S. aureus* under the same conditions. Interestingly, tAgNPs and dAgNPs were unresponsive at light sources complementary to their SPR absorption wavelengths. The authors also monitored Ag^+ release post LED irradiation, wherein tAgNPs showed slightly higher leaching than dAgNPs. However, the levels of Ag^+ (0.21 ppm) were too low to contribute to antibacterial action. The reactive oxygen and nitrogen species (ROS/RNS) fluorescent probes indicated increased emission under NIR irradiation. Additionally, the antibacterial response tested in anaerobic conditions showed a reduced response (~2 log reduction). The decrease in antibacterial action in anaerobic conditions points to the importance of oxygen driving the antibacterial mechanism of these NPs. Thus, the authors concluded that the potential antimicrobial mechanism of NIR-activated tAgNPs was associated with increased ROS/RNS generation and plasmonic heating.

Generally, nanoparticles are combined with PDI platforms to increase the delivery efficiency of the photosensitizer via surface conjugation. AgNPs conjugated with PS offer a unique advantage in this context due to Ag^+ release and its intrinsic antibacterial properties. Multiple studies have reported that combining PS with AgNP allows for metal-enhanced PDI effect, optical and plasmonic advantage, “on-demand” release properties, and photocatalytic effect [81-84]. However, this section is limited to the studies that have experimentally demonstrated antimicrobial effects in resistant and non-resistant strains and biofilms. This review focuses mainly on

understanding the design and synthetic strategies for developing light-activated AgNPs for the treatment of resistant and non-resistant bacterial strains and biofilms. First, we provide insights into the intrinsic antimicrobial properties of AgNP. In the second section, we elaborate on the light-mediated antimicrobial properties of AgNPs. In the final section, we summarize the combination of PS with AgNP to eliminate bacteria and biofilms.

1.6.1 Combination of PS and AgNPs for antibacterial applications.

Silver nanoparticles have been physically or chemically combined with PSs such as porphyrins, phthalocyanines, and methylene blue [84-87]. These PS-AgNP combinations serve three main purposes: a) increase the bioavailability of water-insoluble PSs, b) tune the optical properties for PDI via plasmonic coupling with AgNPs or aggregation-induced emission (AIE), c) control the oxidation of the AgNPs surface to enhance the release of Ag^+ ions. In the first role, AgNPs are used as delivery vehicles of PSs, increasing their bioavailability for effective PDI performance at low concentrations [88]. In the second function, AgNPs can tune the optical absorption of PSs according to the electronic overlap between the SPR of the AgNPs and the absorption band of the PS [81, 89-91]. The third role deals with the oxidation effect of singlet oxygen and/or ROS on the surface of AgNPs to afford Ag^+ ions, which improves the antibacterial outcome of the system [76, 92-95]. Overall, it has been demonstrated that a synergistic effect exists between the combination of PS-AgNPs that improves their antibacterial effect [78, 79, 89].

Studies have also explored introducing either PS and AgNP in sequence i.e. PS first followed by AgNP, to demonstrate the synergy between PDI and AgNP [96, 97]. Nakonieczna and group reported that initial inactivation of *S. aureus* via PDI (PpIX) effect makes them susceptive to AgNP antimicrobial action, resulting in up to 7 log reduction [97]. This sequential PDI and AgNP

combination was also demonstrated in methicillin-resistant *Staphylococcus aureus* 4591 (*MRSA*) and extended-spectrum beta-lactamases-producing *Klebsiella pneumonia*e 2486 (ESBL-KP) [96].

The antibacterial synergy of PS-AgNP reported in the literature can be divided into three categories i.e. a) PS physically associated with AgNPs, b) PS chemically conjugated to AgNPs and c) PS and AgNP incorporated into a nano platform termed as PS- AgNP nanocomposites. The details regarding the NP design, bacterial strains tested, and experimental conditions from these PS-AgNP combinations have been summarized in **Table 1.1**. The antibacterial mechanisms demonstrated in ARBs and non-resistant strains for these PS and AgNP combinations have been described in **Figure 1.3**.

PS physically associated with AgNPs

The association of AgNPs and PSs is carried out through different molecular interactions between the surface of the nanoparticles and PSs, including electrostatic and hydrophobic interactions, which results in the adsorption of PS molecules on the AgNPs' surface. There have been multiple reports that show PS physically linked to AgNPs show antibacterial synergy [98-100]. Li et al. reported a study elaborating on the synergy of AgNP/ Ag+ ions and methylene blue in five bacterial strains: *Serratia marcescens* (SM), *Escherichia coli*, *Klebsiella pneumoniae* (KP), *Pseudomonas aeruginosa* (PA), and *Enterobacter cloacae* (EC) as proof of the relevance of this combination [98]. The authors argued that the mechanism behind this synergy is an Ag^+ interaction with the bacterial cell membrane that facilitates better MB uptake.

Elashnikov, Lyutakov, and co-workers have reported two studies wherein meso-tetraphenylporphyrin (TPP), was combined with silver nitrate followed by further interaction with polymethylmethacrylate (PMMA) nanofibers via electrospinning [99, 100]. The presence of AgNPs

was confirmed via TEM images. The authors first tracked the changes in absorbance of soret band of TPP under illumination (405 nm, 110 mW) and concluded that AgNPs/TPP/PMMA demonstrated higher photostability than only TPP/PMMA. These results implied that the AgNPs protected the TPP within the PMMA nanofibers against photobleaching. The antibacterial tests performed on *E. faecalis* and *S. epidermidis* showed that the AgNPs/TPP/PMMA nanofibers exhibited a significantly higher reduction of bacteria than TPP/PMMA. This result was associated with the cumulative release of silver/ AgNP and the production of ROS. In a similar study, they argue that this release of AgNPs from the nanofibers is promoted by the illumination of TPP, inducing heat-related changes in polymer, contributing to the escape of AgNPs.

Peng and co-workers have developed a hybrid core-shell nanoparticle with a silver as the core and mesoporous silica as the shell (Ag@MS). Several photosensitizers such as mesoporphyrin IX (PIX), Hematoporphyrin IX (HPIX), meso-tetra(4-carboxyphenyl) porphine (TCPP), Cu(II) mesotetra(4-carboxyphenyl) porphine (Cu-TCPP), tris(2,20-bipyridyl) dichlororuthenium(II) hexahydrate (RuBPy), and rose Bengal (RB) have been adsorbed to the surface of Ag@MS [89, 101, 102]. Among these PS, all except RB show stronger resonance coupling with AgNP core that positively correlated to the enhanced production of singlet oxygen [89, 102].

Lismont et al. validated this claim wherein PpIX loaded on Ag@MS NP with a larger AgNP core (100 nm) and thin silica coating (5 nm) led to a 5-fold increase in singlet oxygen generation than PpIX [84]. The Ag@MS@HPIX hybrid shows increased singlet oxygen generation and increased antibacterial killing compared to its PS counterpart. In *MRSA*, these Ag@MS@HPIX hybrid nanoparticles resulted in up to ~6 log inactivation at a concentration equivalent to 2 μM of HPIX. In *S. epidermidis* 5-log bacterial killing was seen at a HPIX

concentration of 2 μM. While in both *E. coli* and *A. baumannii* 4-log inactivation was observed at HPIX concentration of 1 μM [89].

PS chemically conjugated to AgNPs

Unlike the physical interaction between PSs and AgNPs approach, the chemical conjugation between PSs and AgNPs ensures stable nanoformulations with minimal leaking. A chemical bond between PS and AgNP also allows control of distance and target delivery to enhance antibacterial synergy [84]. Most reports in the literature have utilized cysteinyl groups, NHS-EDC chemistry, thiol-Ag affinity, polymer-assisted self-assembly, and coordination via COOH and NH_2 groups. Below, we provide representative examples of how the chemical conjugation approach has been used to treat pathogens.

Masilela et al. reported on the antimicrobial response of PS-conjugated spherical, triangular, and cubic AgNPs against *S. aureus*. Phthalocyanines were selected as the PS to utilize the amines (NH_2) and carboxylic group (COOH) of the cysteinyl moiety for coordination with the AgNP surface. All the PS-AgNP conjugates generated an equivalent amount of singlet oxygen; however, the spherically shaped AgNPs gave the highest antimicrobial activity compared to the triangular and cubic structures [85]. The authors accounted for this result based on the increased surface area provided by the spherical AgNPs due to their smaller size (15 nm) compared to triangular (54 nm) and cubic (60 nm) AgNPs. This can be due to increased Ag^+ release associated with the higher surface area of spherical AgNPs, which contributes to their antibacterial action [66].

Elashnikov, and co-workers also synthesized chemically conjugated PS-AgNP systems [86]. These researchers generated porphyrin-AgNPs by reacting thiolated porphyrin on the surface of AgNPs. To achieve this, the authors synthesized 2,7,12,18-tetramethyl-3,8-divinyl-13,17-[bis(((4-

aminothiophenyl)-carbamoyl]ethyl) porphyrin via amide coupling procedure between the free carboxylic acid groups of protoporphyrin IX and the aromatic amine with thiol groups from 4-aminothiophenol. Under 1 h blue LED exposure, this nanoplatform was successfully able to eradicate *S.epidermidis* and *E. coli* completely. This study argued that the ROS generation is enhanced due to the inclusion of AgNPs leading to an elevated antibacterial effect. This can be associated with the plasmonic coupling of AgNP with PpIX, causing an increase in ROS [81, 89-91].

Another crucial aspect of the light-activated PS-AgNPs is the release of Ag^+ cations associated with the oxidation of the AgNPs surface in the presence of PS generated ROS. However, only a couple of studies have elaborated on the porphyrin-mediated enhanced release of Ag^+ ions and their corresponding antibacterial effect [94, 95]. Sorinolu and co-workers reported an in-depth study detailing the release kinetics of Ag^+ post-light irradiation to understand their role in the antibacterial inactivation of PpIX-AgNP conjugates [94]. Cysteamine-modified PpIX derivatives were synthesized, followed by the thiol-Ag reaction to generate PpIX-AgNP conjugates. The results indicated that PpIX-AgNPs showed higher Ag^+ release than AgNPs. Due to its ionic composition, this effect was more pronounced (25-fold) in Dulbecco's phosphate buffer solution (DPBS) than in nanopure water. The study further proved that this light-mediated increase in Ag^+ contributes to the antibacterial synergy resulting in up to ~7-8 log inactivation of methicillin-resistant *Staphylococcus aureus* (MRSA) and a wild-type multidrug-resistant (MDR) *E. coli* in DPBS.

PS and AgNP incorporated into nanoplatforms (PS- AgNP nanocomposites)

Another approach to developing light-activated AgNP-based systems is incorporating PS-AgNP conjugates, physically or chemically loaded with PSs, into hybrid platforms at the nano or micro scale. These systems have been termed PS-AgNP nanocomposites. These nanocomposites

include fabrics, doped nanomaterials, and polymeric nanomaterials [93, 95, 103]. This alternative confers unique benefits such as stability, target delivery, and potential multi-modal antibacterial applications.

Chen et al. developed an antimicrobial cellulose-based fabric embedded with AgNPs and zinc-phthalocyanines (PS) [95]. The PS was first mixed with DMF solution containing N, N'-Carbonyldiimidazole, followed by the introduction of cellulose fabric into the solution to obtain PS/Fabric via an ester bond. This PS/Fabric was further mixed with Ag^+ ions which are reduced in the presence of the hydroxyl groups in the cellulose fabric to generate AgNPs (AgNP/PS/fabric). SEM studies showed that the size of AgNPs embedded in the fabric is ~ 100 nm in diameter. Moreover, the UV-Vis spectrum depicted 420 nm and 600-800 nm peaks, which are associated with AgNPs and the Q-band of phthalocyanines, respectively. The authors tested the physicochemical properties of the system wherein AgNP/PS/fabric demonstrated 2-fold higher Ag^+ ions release under light conditions than dark conditions. In addition, a higher increase in the ROS generation by the AgNP/PS/fabric system than PS/fabric was also observed. These results corroborated that the AgNP/PS/fabric is capable of producing both Ag^+ and ROS. The antimicrobial properties of the material were evaluated; PS/fabric showed only 7.56% inhibition whereas the AgNP/PS/fabric resulted in a significant 3-log or 99.996 % inhibition in *E.coli*, *S. aureus* (non-resistant) and *MRSA* under 10 min irradiation with light. This further provides evidence to support the broad-spectrum application of PS-AgNPs.

Kuthati employed a similar nanocomposite design to demonstrate the synergy between silver nanoparticles (SNP) and PS by combining AgNP-loaded Cu-MSN with curcumin [103]. Three antimicrobial agents play a crucial role in the synergy in this design, i.e., copper ions, silver nanoparticles, and curcumin. The design improved antibacterial activity since curcumin delivery

was enhanced using MSN carriers and the positive charge of AgNP-loaded Cu-MSN facilitated better interaction with bacteria. The Cur-Cu-MSN-SNP hybrid with a curcumin concentration of 1.5 μM resulted in ~90% (5 logs higher than curcumin only) eradication of gram-negative *E. coli*. The authors concluded that blue LED light-mediated bactericidal synergy against *E.coli* was effective due to elevated Ag^+ ions release and ROS generation.

Xu and collaborators developed a photoactive nanocomposite containing AgNPs, chlorin e6 (Ce6), and bacteria-targeting ligands to allow light-controlled elimination of *MRSA* and *E. coli* [93]. The surface of the AgNPs was modified with a polydopamine shell (PDA) to load the Ce6 molecules to obtain Ce6-AgNPs. Following this, a bacteria-targeting ligand (GP) was tethered to the PDA shell of Ce6-AgNPs via a PEG linker containing amine and thiol groups to obtain the final nanocomposites i.e. GP-Ce6-AgNPs (~50 nm size, ~4 nm PDA shell). The authors demonstrated that the continuous 30-minute laser irradiation of GP-Ce6-AgNPs resulted in a gradual release of Ag^+ ions. When these nanocomposites were exposed to short laser pulses in an ON (5 min) and OFF (5- 10 min) pattern, the release of Ag^+ ions increased only during ON, whereas the amount of Ag^+ reached saturation during OFF, followed by a similar pattern in the other two irradiation cycles. The *in-vitro* relative antibacterial rate for GP-Ce6-AgNP in *MRSA* and *E. coli* was reported as 99.6% and 98.8%, respectively. These values were significantly higher than $AgNO_3$ and Ce6 control groups. The authors argued that the presence of bacteria-specific ligands allowed close interaction of the nanocomposites and bacteria surface, followed by triggered Ag^+ release that disrupts the membrane proteins, compromising the bacterial cell membrane permeability.

Hou and group employed polymeric micelles (PM) with PpIX located in the core and AgNPs decorating the polymeric shell (PM@PpIX@AgNP) [76]. The design consisted of

hydrophilic self-assembled amphiphilic diblock copolymer poly(aspartic acid)-block-poly(ε-caprolactone) (PAsp-b-PCL) micellar nanoparticles with a hydrophobic core containing PpIX. The Ag^+ ions were introduced within the shell of these polymeric micelles which were eventually reduced to generate in-situ AgNPs. The zeta potential was reduced from -55 mV (PM only) to -17 mV (PM@PpIX@AgNPs) with a 100-110 nm hydrodynamic size. PM@PpIX and PM@PpIX@AgNP showed similar ROS generation ability evaluated by using a singlet oxygen generation probe. The antibacterial activity assessed in bioluminescent *S.aureus* XEN36 (MDR strain) indicated that PM@PpIX@AgNP showed better antibacterial response than PM@PpIX at concentrations lower than 200 μg/ mL. These results were further validated using a LIVE/DEAD confocal study, which showed that the PM@PpIX@AgNP after irradiation completely eliminated bacteria. The *in vivo* antibacterial activity was further tested using the bioluminescent *S. aureus* Xen36-infected mouse model. PM@PpIX@AgNP + light exhibited the strongest eradication effect of *S.aureus* XEN36 with no area of infection visible post 5 days.

In summary, the PS-AgNPs conjugates synthesis can be accomplished via physical mixing and covalent conjugation. The chemical conjugation offers an advantage in terms of stable conjugates and maintaining distance between AgNPs and PSs. The antibacterial synergy of PS-AgNP is associated with increased generation of ROS and release of Ag^+. Resistant and non-resistant forms of *S. aureus* and *E.coli* were found to be the most studied bacterial species. Finally, incorporation of the PS-AgNP conjugates within a micro or nano-scale platform such as fabric, polymeric nanomaterials, or doped nanomaterials allows for the generation of light-activated nanocomposites for potential multi-modal antibacterial applications.

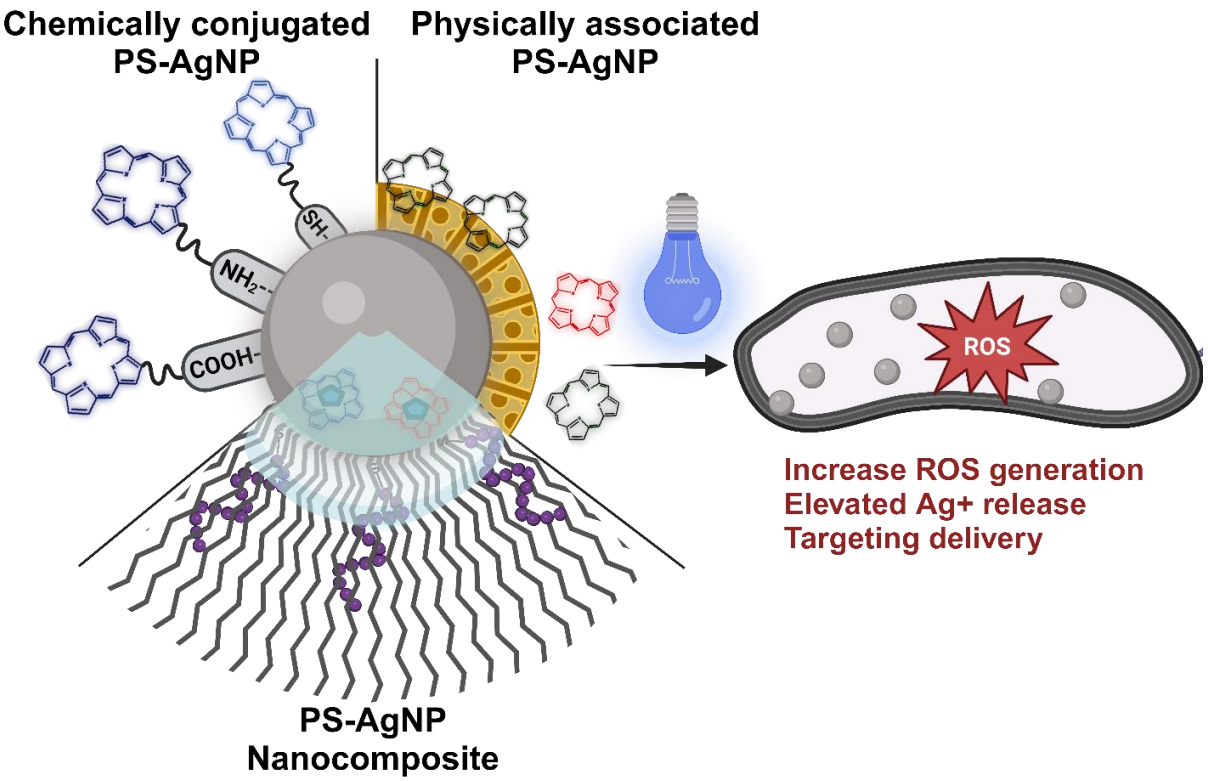

Figure 1.3 Summary of different approaches used to combine PSs and AgNPs, including chemically conjugated PS-AgNPs, physically associated PS-AgNPs, and PS-AgNP composites. All these systems have been tested in non-resistant and resistant bacterial strains.

1.6.2 Combination of PS and AgNPs for inhibition and elimination of biofilms

Biofilm is a slim layer composed of surface-attached aggregates of micro-organisms [28]. Biofilms are more complex environments composed of extracellular polysaccharide substances (EPS), proteins, extracellular DNA, and bacterial cells [34]. AgNPs have been used as a preventative measure in implants and prosthetics to inhibit biofilm formation [58, 104-107]. Reports have suggested that AgNPs tested *in vitro* in planktonic *Klebsiella pneumoniae*, *S. aureus,* and *E. coli* disrupt cell-cell adhesion and inhibit biofilm formation [108, 109]. Incorporating PS into the AgNPs can further assist in EPS disruption, making PS-AgNP conjugates excellent candidates for biofilm inhibition

or elimination. **Table 1.2** summarizes the PS-AgNPs conjugates reported in the literature for inhibition or elimination of biofilms.

Misba et al. were the first ones to test the biofilm inhibition activity of toluidine blue (TBO)-AgNP conjugates in *Streptococcus mutans* using a 630 nm light source (130 mW/cm^2) [110]. Two types of TBO-AgNP conjugates were synthesized by electrostatic interaction of TBO with dextran-capped AgNP ($AgNP_{dex}$) or citrate-capped AgNP ($AgNP_{cit}$). These nanoparticles showed 46% and 62% reduction in biofilm at a concentration of 10 μg/mL, respectively. The authors also reported that both types of TBO-AgNP conjugates inhibited biofilm formation by 99% whereas TBO by itself reduced it by only 70%. Cellular ROS assessment revealed that the TBO-$AgNP_{dex}$ and TBO-$AgNP_{cit}$ mainly generated hydroxyl radical (OH•) and resulted in a 12-fold and 10-fold increase in ROS generation compared with AgNPs. Aydin and co-workers tested a mixture of TBO-AgNP conjugates in 120 teeth samples layered with 3-week-old biofilms. After treatment, a 2.71 average log reduction of bacteria was observed post-60 sec irradiation [111]. However, it should be noted that the control treatment with 2.5% NaOCl showed a higher bacterial reduction of 4.29 log. NaOCl is suggested as the primary irrigation solution in endodontics due to its wide-spectrum antimicrobial efficiency as well as its capability of dissolving organic substances [112].

Methylene blue (MB) is also a phenothiazinium-based cationic dye similar to TBO, which has been widely used to eliminate bacteria. Parasuraman reported a study where MB was physically loaded via electrostatic interactions on the surface of AgNPs. The antibacterial and antibiofilm activity of MB-AgNPs was tested in ESKAPE pathogens such as *S. aureus and P. aeruginosa* biofilms [113]. MB-AgNPs showed a UV-Vis peak at 668 nm associated with MB, confirming its successful conjugation. The bacterial uptake studies showed that MB-AgNPs has greater localization within the bacteria than MB. In *P. aeruginosa* and *S. aureus*, 75.4% and

78.33% of MB was internalized using MB-AgNPs, whereas only 43.6% and 35.5% of MB was internalized. The MIC value in *S. aureus* and *P. aeruginosa* was estimated to be 125 µg/mL. This MIC is two-fold and four-fold higher antimicrobial activity than AgNPs and free MB, respectively. At MIC concentration, 61.41% and 69.15% biofilm inhibition was observed in light-irradiated MB-AgNPs in *P. aeruginosa* and *S. aureus*, respectively. The authors reported that MB-AgNPs showed higher levels of ROS generated by MB-AgNPs, confirming that oxidative stress drove their antibacterial and antibiofilm action.

Curcumin is another PS that has been combined with AgNPs. Ghasemi et al. tested a mixture of curcumin and AgNPs in *P. aeruginosa* planktonic bacteria and biofilms [114]. The mixture containing 200 and 20 µg/mL of curcumin and AgNPs, respectively, was irradiated for 10 min with blue light in the presence of *P. aeruginosa*. An inhibition of 85% of biofilm formation was determined; whereas curcumin and AgNPs only showed 50% and 60% biofilm inhibition, respectively. The mixture of curcumin and AgNPs showed the highest generation of ROS, which contributed to the superior biofilm inhibition capability. The authors reported that the effect induced by this mixture was more effective in inhibiting biofilm formation than removing adhered biofilm.

The above studies have mainly focused on demonstrating the use of PS-AgNP systems for inhibiting biofilm formation. However, Sun and collaborators developed a nanocomposite containing chlorin e6 (Ce6) modified PEI associated with AgNPs to demonstrate the synergistic effect of eliminating biofilms from gram-positive (*S. aureus*) and gram-negative (*E. coli*) bacteria [77]. The authors showed that the presence of AgNPs raised the production of singlet oxygen and ROS due to the SPR effect. The nanocomposite, a size of 60 nm in diameter, was tested in planktonic *S. aureus* and *E. coli* under 660 nm irradiation; 20 mW/cm^2 for 20 min at a 1 mg/mL

concentration. The antibacterial action was more pronounced in *E. coli* with 100% elimination. The authors argued that this is due to the higher sensitivity of Gram-negative bacteria toward Ag^+ ions. In the case of *S. aureus*, 99.9% elimination was achieved, corresponding to ~ 2 log reduction. The penetration of the variable mass ratio of the PEI-Ce6/AgNP, i.e., 0.3 (negative charge, smaller diameter), 1.5 (a positive charge, larger diameter; 240 nm), and 3.0 (a positive charge, smaller diameter: 70 nm) within the *S. aureus* biofilm was evaluated. This approach showed that the highest ratio, i.e., 3.0 with a positive charge (+ 35 mV) and smaller hydrodynamic size (70 nm), showed better infiltration within the EPS matrix than other ratios, indicating that both size and surface charge plays a crucial role. The PEI-Ce6/AgNPs showed increased biofilm elimination in preformed biofilms, resulting in a 2-3 log reduction in bacterial growth in both *S. aureus* and *E.coli*. Nevertheless, in the case of *E. coli,* the authors had to employ a membrane-damaging antibiotic polymyxin B (PMB) in addition to the nanocomposite to show improved results. As a proof of concept for wound healing applications, these nanocomposites were tested *in vivo* in mice models with *S. aureus* skin infection. The nanocomposite and light-treated mice showed faster wound healing, with complete biofilm eradication achieved on the 12^{th} day.

In summary, fewer PS-AgNPs conjugates have been tested in biofilms than bacteria. Most of these PS-AgNP combinations, comprised of photosensitizers such as toluidine blue, methylene blue, and curcumin, reportedly displayed inhibition of biofilm formation (**Figure 1.4**). There has been only one study that has studied penetration of PS-AgNP within biofilms as well as red-light induced eradication of biofilms (*S. aureus and E. coli*) [77]. This study also points to the fact that smaller and positively charged PS-AgNPs show greater penetration within biofilms. The PDI/AgNP synergistic effect has been demonstrated in multiple biofilm-forming bacterial strains such as *Pseudomonas aeruginosa, Enterococcus faecalis*, and *Streptococcus mutans* [110, 111, 113].

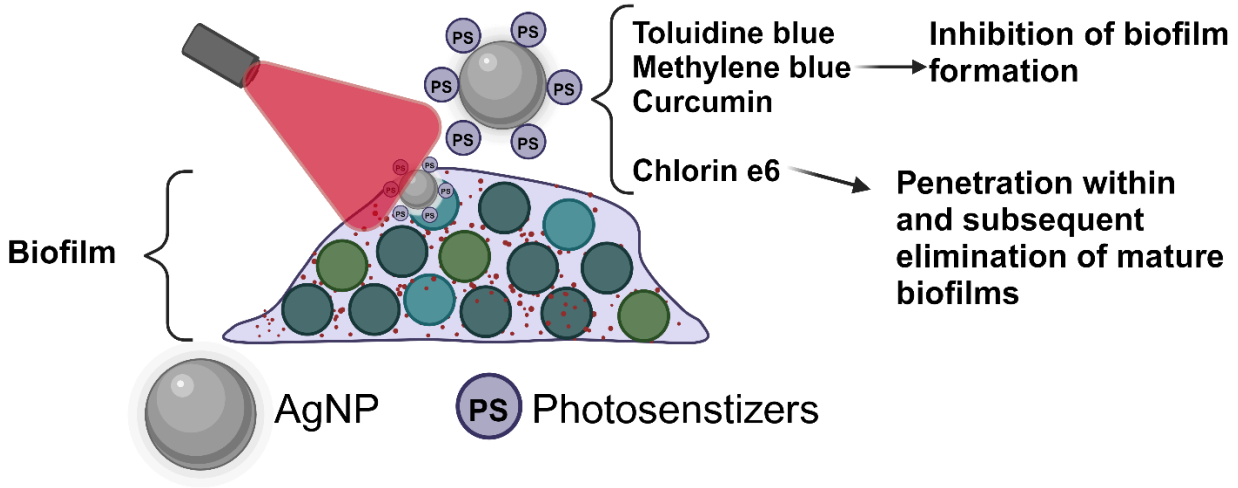

Figure 1.4 Summary of PS-AgNP nanocomposites design for the light-activated inhibition and elimination of bacterial biofilms

Table 1.1 List of PS and AgNP combinations reported for antibacterial applications (antibiotic-resistant bacterial and non-resistant bacterial strains)

Nanoparticle Design	**Photosensitizer**	**Conjugation chemistry**	**Bacterial species tested**	**Light source**	**Reference**
AgNP core with mesoporous silica shell (40-50 nm/ 2-17 nm shell thickness)	Hematoporphyrin IX (HPIX) meso-porphyrin IX (PIX) meso-tetra(4-carboxyphenyl) porphine (TCPP) Cu(II) mesotetra(4-carboxyphenyl) porphine (Cu-TCPP) tris(2,20-bipyridyl) dichlororuthenium (II) hexahydrate (RuBPy)	Adsorption	Methicillin resistant *Staphylococcus .aureus* (MRSA) (ATCC BAA-44) *Staphylococcus epidermidis* (ATCC 35984) *Escherichia coli (E. coli* ATCC 35218) *Acetobacter baumannii* (drug resistant) (ATCC 19606) *Trichophyton rubrum*	White light; 408 mW/cm^2; 300 mW/cm^2	89, 101, 102

	rose bengal (RB)		(ATCC 28188)		
Silver nanoparticles	Methylene blue	Physical mixture	*Streptococci* *Serratia marcescens (SM)*, *Escherichia coli*, *Klebsiella pneumoniae* (KP), *Pseudomonas aeruginosa* (PA), and *Enterobacter cloacae* (EC)	Diode Red laser (660 nm; 180 J/cm^2) LED Red (660 nm; 6.8 mW; 180 J/cm^2)	[98, 115]
Silver Nanoparticles	Zn-meso-5,10,15,20-tetra(4-pyridyl) Zn-meso-5,10,15,20-tetrathienyl Zn-meso-5-(4-hydroxyphenyl)-10,15,20-tris(2-thienyl)	Electrostatic self-assembly	*Staphylococcus aureus*	595 nm LED (15min, 40 J/cm^2)	[116]
Silver nanoparticles	TMPyP (5,10,15,20 – tetrakis(N-methylpyriminium-4-yl) porphyrin)	Physical mixture	*MRSA*, extended-spectrum beta-lactamases-producing (ESBL) *Klebsiella pneumoniae*	LED (414 nm; 54 mW/cm^2	[96]
AgNP (spherical, triangular and cubic)	Phthalocyanines	Coordination via NH2 and COOH groups of cysteinyl moiety	*S. aureus* (ATCC 6538)	Visible light (300W, 90 min)	[85]

AgNP	Protoporphyrin IX	NHS-EDC chemistry for linking cysteamine	*MRSA (*ATCC BAA 44 strain*)* Wild type *MDR E. coli*	White light (400- 700 nm; 56 ± 2 mW/cm^2)	[94]
AgNP in-situ synthesized with cellulose fabric	Zinc pthalocyanines	PS linked to cellulose fabric via EDC chemistry. No direct link with AgNPs	*E. coli*, ATCC 8739) *S. aureus* (ATCC 6538) *methicillin MRSA* (ATCC 33591)	LED light (75 mW/cm^2, 10 min, 660 nm)	[95]
Silver nanoparticles (2 nm) (embedded in PMMA fibers)	Tetraphenylporphyrin (TPP)	Electrospinning; No direct link with AgNPs	*Staphylococcus epidermidis Enterococcus faecalis*	LED (405 nm; 3 hours; 400 mW/cm^2	[99]
Polymeric nanoparticles with PpIX core and AgNP embedded within polymeric shell	Protoporphyrin (located in core)	Self-assembly of PpIX with co-block polymer. No direct link with AgNPs	MDR *S. aureus* Xen36	Laser, 635 nm, 0.25 W/cm^2, 10 min	[76]
Silver nanoparticles + Copper-doped MSN	Curcumin	Adsorption	*E. coli*	Blue LED light 470 nm (72 J/cm^2)	[103]
Silver nanoparticle with polydopamine (PDA) shell	Chlorin e6 (Ce6)	Ce6 functionalized on AgNP via PDA shell	*MRSA (ATCC 29213); E. coli (ATCC 25922)*	Red laser (655 nm, 300 mW/cm^2, 10 min)	[93]

Table 1.2 List of PS and AgNP combinations reported for inhibition and elimination of biofilms

Photosensitizer	**NP design**	**Biofilm strain**	**Type of biofilm tested (Inhibition vs Elimination)**	**Reference**
Toluidine blue O (TBO)	Electrostatic interaction with AgNPs	*Enterococcus Faecalis Streptococcus mutans*	Inhibition (tested in planktonic bacteria)	[110, 111]
Methylene blue	Electrostatic interaction with AgNPs	*S.aureus P. aeruginosa*	Inhibition (tested in planktonic bacteria)	[113]
Curcumin	Physical mixture	*P. aeruginosa*	Inhibition (tested in planktonic bacteria)	[114]
Chlorin e6	PEI conjugated Ce6 electrostatically linked with AgNP	*E. coli S. aureus*	Inhibition (tested in planktonic bacteria) and Elimination (tested in mature biofilm)	[77]

1.7 Summary of the thesis

With the rise in antibiotic resistance (AR) and multidrug-resistant (MDR) bacteria, there is an urgent need for novel antibacterial agents that can exert antibacterial action via multiple mechanisms. Nanoparticles such as silver nanoparticles (AgNP) are an excellent candidate due to their unique optical and physiochemical properties and innate broad-spectrum antibacterial activity. Taking advantage of these properties, recent studies have indicated that photosensitizers (PS) and AgNP combinations result in synergistic antibacterial effects. Based on these studies, the increased ROS production drives the synergistic antibacterial effect of light-activated PS-AgNP conjugates. However, a crucial aspect of these light-activated PS-AgNPs is the release of Ag^{+} cations, which is not investigated in the literature. This thesis is focused on developing light-activated PS-AgNPs and evaluating their light-responsive antibacterial effect in ARBs, *methicillin-resistant Staphylococcus aureus (MRSA),* and multidrug-resistant *Escherichia coli* and inhibit

biofilm formation in *Vibrio cholerae*. The major focus of this thesis is to understand the role of Ag^+ release in the antibacterial synergy PS-AgNP and modulate it for elevated antibacterial effect in ARBs and biofilm inhibition.

Chapter 2 reports the synthesis and characterization of protoporphyrin IX conjugated AgNP (PpIX-AgNP). To evaluate the effect of positive surface charge on the antibacterial properties of these nanomaterials, PpIX-AgNPs were further modified with polyethyleneimine (PEI) to afford PEI-PpIX-AgNPs. The chapter includes an in-depth study detailing the Ag^+ release kinetic post-light irradiation to understand their role in antibacterial synergy. The synergistic effect of this approach was successfully evaluated against Gram-positive and Gram-negative bacteria, an *MRSA* strain, and an *MDR E. coli*, respectively. Finally, the biocompatibility of the synthesized nanoparticles against mammalian cells (HeLa cells) was examined at the observed bacterial inhibitory concentration.

Next in Chapter 3, the effect of bacterial cell culture composition and modulation of light irradiation strategy on Ag^+ release kinetics and subsequent antibacterial activity was studied. The PpIX-AgNPs developed in Chapter 2 are used here and their colloidal stability is evaluated in realistic bacterial culture media, nutrient broth (NB), tryptic soy broth (TSB), and Luria Bertani broth (LB). This chapter also reports on the advantage of introducing a dual-step irradiation setup (2 cycles of irradiation) to increase Ag^+ release efficiency to achieve antibacterial action at lower PpIX-AgNP concentrations. The subsequent antibacterial effect of PpIX-AgNPs against *MRSA* (tested in NB) under single and dual-step irradiation setup is reported here.

Chapter 4 presents preliminary work evaluating PpIX-AgNP, as a light-activated antimicrobials, to inhibit biofilm formation in *V. cholerae*. Additionally, chapter 4 includes an investigation of nanoparticle transport within mock biofilms. The mock biofilm was used to

simulate the extracellular polymeric substance (EPS) structure of the biofilm and fluorescent nanoparticles (FNPs) transport across the mock biofilm was evaluated using z-stack enabled confocal microscopy.

Finally, chapter 5 summarizes the main conclusions drawn from this thesis. This chapter also includes the future direction of these light-activated PpIX-AgNP for ARBs treatment and elimination of biofilms.

2 CHAPTER 2: INFLUENCE OF SILVER ION RELEASE ON THE INACTIVATION OF ANTIBIOTIC-RESISTANT BACTERIA USING LIGHT-ACTIVATED SILVER NANOPARTICLES

2.1 Introduction

With the rise in multidrug-resistant (MDR) bacteria, there is an urgent need for new antibacterial agents with targets that have low possibility of developing resistance through mutation, and that can overcome the latest bacterial resistance mechanisms [13, 21]. It is desired that novel antibacterial agents inhibit bacteria via multiple mechanisms with bactericidal actions that do not involve specific biochemical pathways. In recent years, great attention has been directed to the use of antimicrobial nanoparticles (NPs) as an alternative with novel non-specific low-mutation bacterial targets [13, 117]. Antimicrobial NPs inactivate microorganisms via non-specific pathways with multiple targets involving a combination of cell membrane lysis and reactive oxygen species (ROS) generation to degrade cellular compounds [14, 117]. Thus, antimicrobial NPs have a high barrier against resistance development. Moreover, the use of nanoscale antimicrobials allows for increased bioavailability by promoting transport through the cell membrane to the target site [117-119]. Silver nanoparticles (AgNPs) have gained wide use in different antimicrobial research areas because they significantly inhibit several Gram-positive and Gram-negative bacteria and have a lower tendency for antibacterial resistance development [14, 120, 121]. Consequently, several studies have been conducted to fully understand the antibacterial mechanisms of AgNPs to promote its antimicrobial applications [14, 122, 123]. These studies have elucidated that the antibacterial action of AgNPs is mainly based on the localized release of silver ions (Ag^+) from the surface of AgNPs. The released Ag^+ affords bacterial inactivation due to interaction with enzymes and proteins, and high ROS production [14, 121, 123-125]. Therefore, AgNPs act as a reservoir of Ag^+ that are released by

oxidative dissolution in aerobic or other oxidative conditions [126, 127]. Hence, the design of novel strategies that increase the oxidation of AgNPs to enhance the release of Ag^+ ions can have a major impact on the antimicrobial features of AgNPs.

Photosensitizers (PSs) are molecules that upon the absorption of light generate ROS. PSs have also been used to inactivate bacteria by causing oxidative stress or damage to cellular components when irradiated with visible light, this approach is called photodynamic inactivation (PDI) [120, 121, 125]. Recent studies have shown that the PS-AgNP combination has a synergistic antimicrobial effect. These studies demonstrated that the synergistic antimicrobial effect of PS-AgNP conjugates in bacteria (non-resistant) is concentration dependent and contributed by the oxidative stress due to enhanced ROS production [124, 128-131]. However, there is a lack of understanding of the impact of the light-mediated release of Ag^+ in these systems, which is also a critical parameter that contributes to the antibacterial synergy in PSs and AgNPs conjugates. Herein, we report an in-depth study to understand the role of PS-mediated ROS generation to increase Ag^+ release and its antimicrobial effect against antibiotic resistant bacteria (ARB).

In this chapter, we synthesized PS-modified AgNPs using protoporphyrin IX (PpIX) as PS. PpIX has been extensively used as an effective antimicrobial agent either as single molecule or attached to different materials [132, 133]. The surface of AgNPs were functionalized with a thiol derivative of PpIX to afford conjugated PpIX-AgNPs (**Figure 2.1**). Moreover, to evaluate the effect of positive surface charge on the antimicrobial properties of these nanomaterials, PpIX-AgNPs were further modified with polyethyleneimine (PEI) to afford PEI-PpIX-AgNPs. The physicochemical and photophysical properties of these NPs were characterized. We studied the release of Ag^+ from these materials in the presence or absence of light. The synergistic effect of

this approach was successfully evaluated against Gram-positive and Gram-negative bacteria, a methicillin-resistant *Staphylococcus aureus* (MRSA) strain, and an MDR *Escherichia coli strain*, respectively. It is noteworthy to mention that over 50% of all clinically reported infections from seven organisms are caused by *S. aureus* and *E. coli* [25, 134]. Finally, the biocompatibility of the three nanoparticles against mammalian cells was examined at the observed bacterial inhibitory concentration. We envision that the results obtained in this work will help to optimize the performance of light-activated AgNP platforms. Moreover, it could have a major impact on reducing some of the recent safety concerns associated with colloidal AgNPs such as argyria and other adverse effects leading to human death [121].

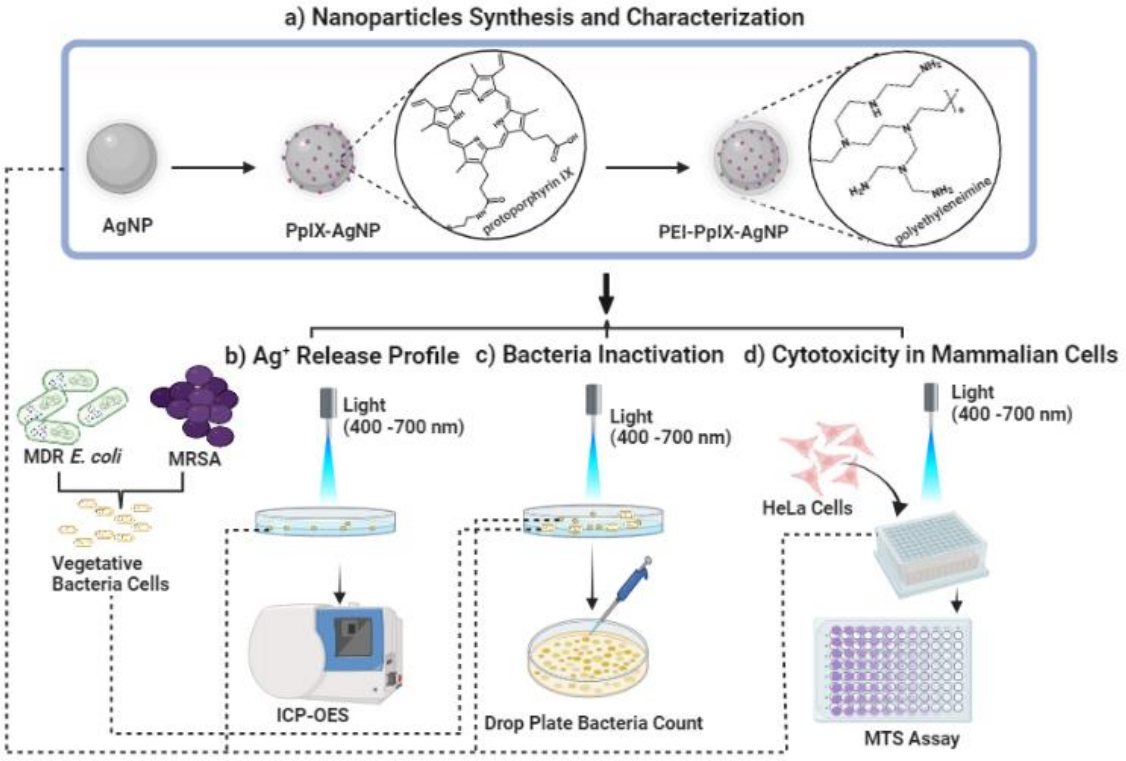

Figure 2.1 A) Synthesis of PpIX-AgNPs and PEI-PpIX-AgNPs. B) Ag+ release profile obtained post-light activation using ICP-OES. C) Antimicrobial activity of the light irradiated nanoparticles

assessed by drop plate colony count method. D) Cytotoxicity in mammalian cells performed via MTS assay.

2.2 Experimental Section

2.2.1 Synthesis and characterization of nanoparticles: AgNPs, PpIX-AgNPs and PEI-PpIX-AgNPs.

Synthesis of AgNPs.

All glassware used for the synthesis of AgNPs were cleaned with aqua regia (3-parts in volume of hydrochloric acid and 1-part in volume of nitric acid) prior to their use.

AgNPs were synthesized based on the co-reduction method using sodium citrate and tannic acid [135]. Briefly, a 100 mL aqueous solution of 5 mM trisodium citrate and 0.25 mM of tannic acid were brought to a boil at 100 °C under vigorous stirring. A condenser was used to prevent loss of water. As the solution starts boiling, 1 mL of aqueous solution of 25 mM silver nitrate was added to the solution in one shot leading to an immediate color change from colorless to yellow. The solution was removed from the heat and cooled at room temperature under constant stirring. The AgNPs were centrifuged at 12000 rpm for 15 min to remove excess of tannic acid and further washed with water three times under the same centrifugation conditions. As-synthesized AgNPs are stored in nanopure water.

Synthesis of PpIX conjugated AgNPs (PpIX-AgNPs).

The PpIX-AgNPs were obtained by reacting AgNPs with cysPpIX (1:0.5 mass ratio) (Scheme S2). A solution of cysPpIX in DMF (1 mg/mL) was prepared. AgNPs (1 mg) were centrifuged down at 12000 rpm for 15 min to remove the water. Following this, 1 mL of DMF was added and sonication was used to disperse the AgNPs. This solution was transferred to a 20 mL

scintillation glass vial and 500 µL of previously prepared cysPpIX solution in DMF was added. An additional 3.5 mL of DMF was added and the reaction mixture was vigorously stirred for 48 h at room temperature. After the reaction, the unreacted cysPpIX was collected via centrifugation at 12000 rpm for 15 min. Nanoparticles were washed three times with DMF and separated under the same centrifugation conditions. The supernatant collected was analyzed using UV-Vis spectrophotometer to determine the amount of PpIX conjugated on AgNPs surface. A typical batch fabricated under the above-mentioned conditions produced 1.2 ± 0.1 mg of PpIX-AgNPs. The PpIX-AgNPs were stored in DMF under dark conditions.

Synthesis of PEI coated PpIX-AgNPs (PEI-PpIX-AgNPs).

The PpIX-AgNPs were coated with polyethyleneimine (PEI; MW = 10 KDa) based on the electrostatic interaction between the polymer and the nanoparticles. An aqueous solution of PpIX-AgNPs and PEI were mixed in a 1:10 mass ratio. Briefly, 1 mg of PpIX-AgNPs were centrifuged down and dispersed in 1 mL of nanopure water using sonication. Separately, 10 mg of PEI was weighed in a scintillation vial and dispersed in 5 mL of nanopure water to get a concentration of 2 mg/mL. Finally, 5 mL of the PEI solution was mixed with 1 mg/mL of PpIX-AgNPs, and the solution was vigorously stirred at room temperature for 24 h. Following this, the material was washed three times with nanopure water and stored at room temperature under dark conditions. PEI coating was confirmed via zeta potential measurement.

2.2.2 Light-mediated release profile of Ag+ ions from nanoparticles.

The Ag^{+} quantification was evaluated using inductively coupled plasma - optical emission spectroscopy (ICP-OES) (Optima 3000, Agilent). Samples obtained from digested and release experiments were introduced into plasma by peristaltic pump and discharged as an aerosol

suspended in argon gas. The data acquisition was performed in triplicates with the torch assembly in the axial mode. The default acquisition parameters used are RF = 1.2 kW; auxiliary gas flow = 1 L/min, nebulizer gas flow = 0.7 L/min; plasma flow = 12 L/min, pump speed = 12 rpm; stabilization time = 15 s; sample uptake time = 25 s; Rinse time = 30 s and Ag analytical line = 328.068 nm.

To determine the total amount of Ag^+ in all samples, aliquots of the nanoparticles were digested by performing a "cold digestion" followed by "hot digestion" [136]. The digestion protocol was optimized and modified in terms of time and volume. Cold digestion includes mixing 50 µg of NPs with 2.5 mL of concentrated HNO_3 and incubating at room temperature for 30 min. Later, this mixture was heated under 150 °C using an oil bath for 4-6 h to allow excess HNO_3 to evaporate (hot digestion). The remaining volume was measured using a graduated cylinder and diluted using 2% HNO_3. The samples were filtered through a 0.22 µm polyethersulfone (PES) membrane before ICP-OES analysis. A calibration curve was obtained using an Ag silver standard diluted in 2% HNO_3 to prepare standard concentrations of 10, 25, 50, 100 µg/L (Figure S5a). A new set of calibration curves were generated for each run. The total amount of Ag^+ digested (in µg) was calculated using the calibration curve and expressed in terms of Ag^+ amount per µg of NP (%) (Table S1). The concentration of AgNPs and PpIX-AgNPs (1.5 µg/mL) used for release and bacterial experiments was also digested using the same protocol to calculate the total Ag^+ digested (Figure S5b).

The release kinetics of Ag^+ was tested in Dulbecco's phosphate buffer solution (DPBS, 1X) and nanopure water. Stock solutions of AgNPs (water), PpIX-AgNPs (DMF) and PEI-PpIX-AgNPs (water) equivalent to 150 µg/mL of AgNPs were prepared for the analysis. The stock

samples were diluted 100 times with the relevant media (PBS or water) to obtain 3 mL of sample. A Petri dish (60 x 15 mm) containing 3 mL of each sample was prepared using the stock solution such that the final concentration is 1.5 μg/mL in terms of AgNPs. Each Petri dish containing the samples was irradiated with a white light source (400-700 nm; 56 ± 2 mW/cm^2) for 20 min. Before irradiation, 200 μL sample was withdrawn indicating the time point as 0 min. Then, 200 μL was collected at specific time points from each sample at 5, 10, 20, 30 min, 1, 2, 4, 6, 12, 24 h. The collected samples were immediately centrifuged for 10 min at 13000 rpm and the supernatant was collected for ICP-OES analysis. The same experiments were repeated in the dark as control by covering the Petri dishes with aluminum foil to avoid unwanted light exposure. The Ag^+ concentration obtained for each time point was normalized based on the lowest initial amount of Ag^+, which is associated with PEI-PpIX-AgNPs. The kinetic release rates were determined by performing linear fit on the Ag^+ release kinetic plots using OriginPro 2021 (Academic version). The R^2 and slope values corresponding to burst and slow release were recorded (Table S4).

2.2.3 Bacterial inactivation experiment.

The antimicrobial activities of AgNPs, PpIX-AgNPs and PEI-PpIX-AgNPs were examined against a MRSA strain (BAA 44) purchased from ATCC and a wild-type MDR *E. coli* strain (accession number PRJNA806466). The MDR *E. coli* was isolated from Class B biosolids amended soil [137]. Details of the MDR *E. coli* sequence protocol and data analysis are provided in the ESI. It was confirmed to be resistant to tetracycline, gentamicin, ampicillin, sulfamethoxazole-trimethoprim and ciprofloxacin using the CLSI M100 Performance Standards [138]. Stock solutions of AgNPs and PpIX-AgNPs were prepared in DMF; while PEI-PpIX-AgNPs was prepared in nanopure water (18 MΩ-cm). A single bacterial colony of each strain was aseptically picked from

the top of a LB agar plate using a sterile loop and inoculated into sterile LB broth media. Bacteria cells were grown overnight (~ 18 h) at 37 °C under continuous gentle shaking at 200 rpm. Overnight cells were harvested the following day by centrifugation at 7000 rpm for 5 min, washed twice with PBS and resuspended in 1X DPBS to achieve an absorbance of 0.5 McFarland turbidity standard (~1.5 x 10^8 CFU/mL). Before light irradiation, 2,970 µL bacteria cells in 1X DPBS were incubated at room temperature in the dark for 30 min with 30 µL of each sample to achieve a working concentration of 1.5 µg/mL for AgNPs, and 1 µM cysPpIX-1.5 µg/mL AgNPs for PpIX-AgNPs. The resulting DMF concentration in the final reaction volume was ≤ 1%. Thereafter, cells were irradiated for 20 min without stirring in a petri dish (60 x 15 mm) with a white light source (400–700 nm; 56 ± 2 mW/cm^2). The surviving cells were counted after 0, 4, and 24 h post irradiation in triplicate using the drop plate colony count method [139]. At specific time point, 100 µL of the sample was withdrawn, serially diluted and 20 µL of each dilution was spotted on LB agar. The bacterial log inactivation was estimated using Equation 1. In all experimental groups, negative control and dark control samples were counted. A physical mixture of $AgNO_3$ and cysPpIX was used as a positive control. The concentration of $AgNO_3$ used corresponds to the amount of maximum Ag^+ (µg/L) released from the conjugate samples.

$$\text{Log inactivation of bacteria } = \log \frac{C_o}{C_t} \quad (1)$$

where C_o is the concentration (CFU/mL) of bacteria without the addition of nanoparticles and C_t is the bacterial concentration after the addition of nanoparticles and (or) light irradiation after time t.

2.2.4 Cytotoxicity in mammalian cells.

AgNPs, PpIX-AgNPs and PEI-PpIX-AgNPs were tested in Hela cells to assess their cytotoxicity in mammalian cells. HeLa cells obtained from ATCC were cultured in RPMI media supplemented with 10% FBS and 1% pen-strep at 37 °C with 5% CO_2 exposure. The *in vitro* cytotoxicity was carried out using the CellTiter 96 Aqueous Assay (MTS assay). HeLa cells were grown in 96-well plate at 1000 cells per well for 24 h before inoculation. Post cell adherence, media was discarded and cell media containing the nanoparticles (1.5 µg/mL) were inoculated. Post 30 min incubation, cells inoculated with nanoparticles were irradiated with Biotable power source with RGB LED array for 20 min (450- 475 nm; 34.5 mW/cm^2) and incubated for 24 h at 37 °C with 5% CO_2 exposure. After incubation, the media was removed, and the cells were washed with PBS. To each well, 100 µL of media was added followed by the addition of 20 µL of CellTiter 96 Aqueous assay. The plates were incubated for 2.5 h at 37 °C and the absorbance at 490 nm was measured using plate reader Multiskan FC. Cell viability was calculated by subtracting absorbance with that of media and using equation 2.

$$\text{Cell Viability (\%)} = \frac{A_{NP}}{A_o} \times 100 \qquad (2)$$

where, A_{Np} is the absorbance of cells treated with nanoparticles and A_o is the absorbance of untreated cells.

2.2.5 Statistical Analysis

Graphs and statistical analyses were performed using OriginPro 2021 (Academic Version). Statistical significance between disinfection trials was assessed by one-way analysis of variance

(ANOVA). All the statistical analyses were performed with $\alpha = 0.05$ and reported as stars assigned to the p-values: ***$p \leq 0.0001$, **$p \leq 0.001$, *$p \leq 0.05$, and ns $p > 0.05$.

2.3 Results and Discussion

2.3.1 Nanoparticles: Synthesis and Characterization.

Synthesis of cysteamine-modified PpIX (cysPpIX)

The synthesis of cysPpIX was carried out through a two-step synthetic approach (Scheme S1). Herein, the carboxylic acid groups on PpIX were activated using NHS rendering ester groups (sePpIX) followed by a nucleophilic acyl substitution reaction with cysteamine to form cysPpIX [140, 141]. The successful generation of the PpIX derivatives (sePpIX and cysPpIX) was confirmed using FT-IR, UV-Vis, ^{1}H NMR and MALDI-MS, (Figures S1-S3). The FT-IR shows a C=O stretching at 1739 cm^{-1} indicative of ester group and C=O stretching at 1810 cm^{-1} and 1778 cm^{-1} associated with NHS molecule confirming the synthesis of sePpIX (Figure S1a). After nucleophilic acyl substitution with cysteamine, a C=O stretching at 1643 cm^{-1} and N-H stretching at 3312 cm^{-1} were observed, which correspond to formation of amide bond (Figure S1a). UV-Vis spectra indicate minimal difference for Soret-band at 405 nm between PpIX, sePpIX and cysPpIX (Figure S1b). However, the Q-bands observed at 510, 550, 625 and 650 nm in PpIX and sePpIX underwent a slight redshift for cysPpIX (Figure S1b). ^{1}H NMR analysis also confirmed the successful synthesis of sePpIX and cysPpIX (ESI and Figure S2). The synthesis of sePpIX and cysPpIX was further confirmed based on the MALDI-MS peaks at 758.44 (calculated=756.30) and 678.90 (calculated = 680.93) respectively (Figure S3).

Synthesis and characterization of AgNPs, PpIX-AgNPs and PEI-PpIX-AgNPs

AgNPs were synthesized following the co-reduction method using sodium citrate and tannic acid [135]. As-synthesized AgNPs were functionalized with cysPpIX following previous protocols that take advantage of the strong Ag-S affinity [142, 143]. Further modification of the platform was carried out with PEI using the electrostatic interaction between the nanoparticles and PEI polymer (Scheme S2). The as-synthesized AgNPs were spherical with a diameter of 42.2 ± 7.8 nm (n = 150) as measured by TEM (**Figure 2.2**). The TEM size of PpIX-AgNP is 42.2 ± 8.9 nm (n = 150) and of PEI-PpIX-AgNP is 37.2 ± 7.3 nm (n = 150), indicating no statistical difference between them and the parent AgNPs (**Figure 2.2a**). The hydrodynamic diameter of AgNPs in PBS is 36.3 ± 1.1 nm with a polydispersity index (PdI) of 0.20 (**Figure 2.2b**). ζ-potential shows that the surface is negatively charged (-49.1 ± 5.5 mV) due to the presence of citrate molecules as capping agents (Table S2). The hydrodynamic diameter of the PpIX-AgNPs slightly increases to 55.6 ± 6.7 nm with PdI of 0.43 in PBS. These values clearly indicate that aggregation can be associated with the presence of PpIX on the surface of AgNPs. ζ-potential also shows minimal difference with a value of -57.3 ± 4.8 mV. Successful synthesis of PEI-PpIX-AgNP was confirmed by the positive ζ-potential value of 27.1 ± 1.7 mV. PEI-PpIX-AgNP further lead to higher hydrodynamic size in PBS with 137.6 ± 4.0 nm and PdI = 0.29. All the DLS and ζ-potential measurements are summarized in Table S2.

UV-Vis spectroscopy of AgNPs depicts an absorption band with a maximum wavelength at 427 nm (**Figure 2.2 d**), which is characteristic of the surface plasmon resonance (SPR) associated with metallic nanoparticles [144]. UV-Vis spectrum of PpIX-AgNPs clearly indicates the presence of PpIX corresponding to the Soret- and Q-bands. PpIX-AgNPs shows a strong absorption band from 350–500 nm with a maximum at 430 nm, which is the result of the overlap between the SPR and the Soret-band of PpIX. The amount of PpIX loaded on the nanoparticle was

determined using a calibration curve of cysPpIX at 500 nm as indicated in the experimental section (Figure S4). The percentage of PpIX loading was found to be around 45 ± 0.57 % (n=6). This value was further confirmed by determining the amount of Ag in the PpIX-AgNPs using ICP-OES (Table S1).

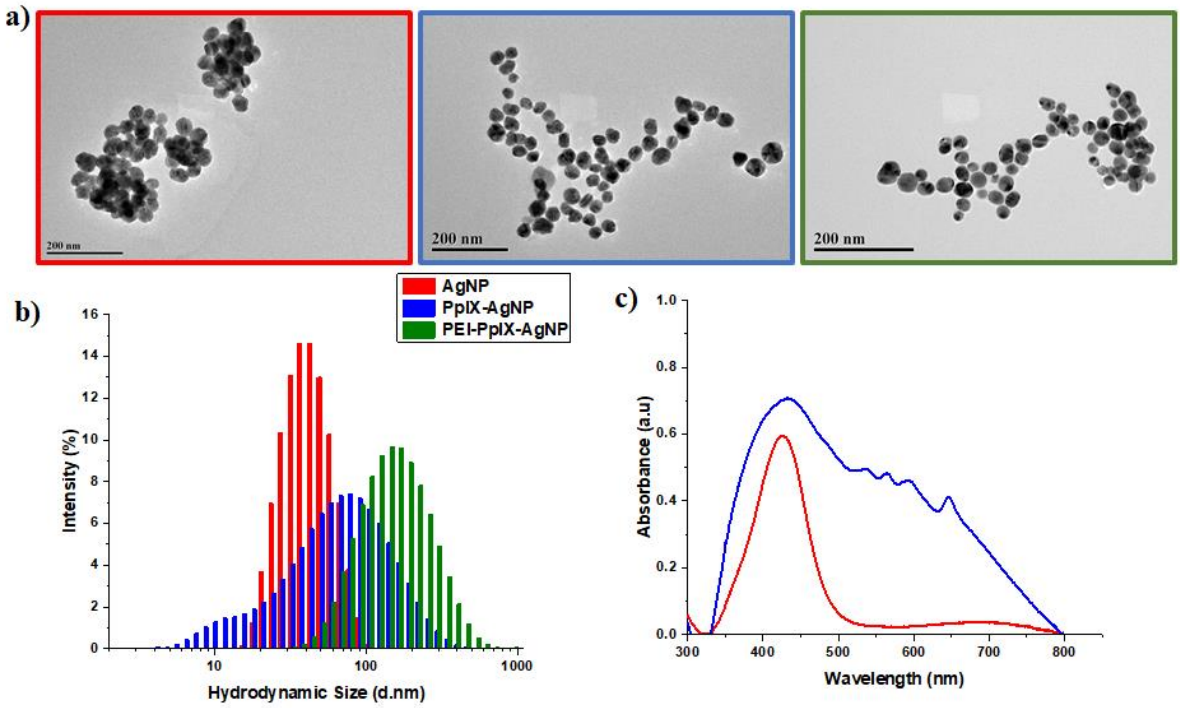

Figure 2.2 Characterization of AgNPs, PpIX-AgNPs, and PEI-PpIX-AgNPs. a) TEM images for AgNPs, PpIX-AgNPs and PEI-PpIX-NPs. b) Dynamic light scattering plot in PBS for AgNPs (red), PpIX-AgNPs (blue) and PEI-PpIX-AgNPs (green). c) UV-Vis spectrum for AgNPs (red) and PpIX-AgNPs (blue).

The ability of PpIX attached to AgNPs to generate singlet oxygen ($^1O_2$) was evaluated by determining the $^1O_2$ quantum yield (Φ_Δ). For this experiment, 9,10 dimethylanthracene (DMA) was used as the $^1O_2$ probe and its decay at 380 nm with respect to the irradiation time was used to calculate Φ_Δ (Table S3) [46, 145]. The lower Φ_Δ value for PpIX-AgNPs (Φ_Δ = 0.01) compared to and

the parent porphyrin cysPpIX ($\Phi_\Delta = 0.38$) could be attributed to the fact that the $^1O_2$ released by PpIX is in close proximity to AgNPs; therefore, it is selectively oxidizing the surface of the nanoparticles to release Ag^+ ions as demonstrated in the section below. This surface effect will leave a very low amount of $^1O_2$ remaining to react with the DMA probe.

2.3.2 Investigation of the release profile of Ag+ from AgNPs, PpIX-AgNPs and PEI-PpIX-AgNPs.

Previous reports have described the combination of PSs with AgNPs [124, 128-131, 146]. Most of these studies are limited to demonstrating the increased antimicrobial effect of PS-AgNPs in terms of enhanced PS photochemical properties. As far as we know, only one study has investigated the oxidative effect of PSs on the release of Ag^+ after light irradiation [146]. In this work, the increase in Ag^+ release from phthalocyanine-AgNPs was analyzed only at 1 h post-irradiation. A synergistic effect was observed for the elimination of bacteria. A kinetic study detailing the Ag^+ release during and post-light irradiation is critical to understanding their role in antibacterial synergy. Herein, we performed an in-depth study of the impact of light-activated generation of ROS through PpIX on the release kinetics of Ag^+. Two different media were investigated; nanopure water and DPBS, and a broad white light (400-700 nm; 56 ± 2 mW/cm^2) was used as a light source. For these experiments, the Ag^+ release kinetics from AgNPs, PpIX-AgNPs and PEI-PpIX-AgNPs was evaluated in two distinctive stages; first, the one associated to light irradiation for 20 min, "burst release"; and the second one, due to the long-term dissolution of Ag^+ in the two different aqueous media, "steady release." As seen in **Figures 2.3a** and S6, after light irradiation in water, PpIX-AgNPs showed a burst release within the first 20 minutes (release rate = 8.56 μg L^{-1} min^{-1}) followed by a constant increase in Ag^+ release in the next 24 h (release rate = 0.02 μg L^{-1} min^{-1}). On the contrary, the minimal release of Ag^+ was observed in water for PEI-PpIX-AgNPs (**Figure**

2.3a). Most likely due to the strong interaction between Ag^+ ions and amine groups in the PEI [147]. Moreover, a reduction in the oxidative effect of the ROS produced by PpIX on the surface of the AgNPs could be also associated to the presence of PEI [148]. In the case of AgNPs, a slow release (release rate = 0.04 μg L^{-1} min^{-1}) was observed after 720 min. The total Ag^+ released achieved for PpIX-AgNPs in water was 22% wt. Control experiment in water without light irradiation show a minimal release of Ag^+ from these nanoparticles (Figure S7a). The release of Ag^+ from AgNPs in water in the absence of a PS has already been studied [149-151]. The presence of oxygen in water affords the oxidation of AgNPs resulting in a slow release of Ag^+ [150, 152, 153]. PpIX-AgNPs platform in the presence of light increases 25-fold the release of Ag^+. The burst release is most likely directly associated with the oxidation of the AgNPs surface in presence of $^1O_2$, which is the main ROS produced by PpIX [154, 155]. The lifetime of $^1O_2$ in water is 3-5 μs with diffusion coefficient 2 x 10^{-5} cm^2/s, which limits their activity to a distance of 125 nm [156, 157]. However, in biologicals systems, this distance further reduces to less than half of the one mentioned above [157, 158]. Therefore, the close proximity of the generation of $^1O_2$ to the surface of AgNPs accounts for the fast Ag^+ release kinetics in the first 20 min during the time of light irradiation.

To take in account the effect of the media, the release of Ag^+ from AgNPs, PpIX-AgNPs and PEI-PpIX-AgNP were also examined in DPBS. DPBS is a buffer solution composed of potassium chloride (KCl), potassium phosphate monobasic (KH_2PO_4), sodium phosphate dibasic (Na_2HPO_4-$7H_2O$) and sodium chloride (NaCl) that is widely used to simulate physiological conditions. A similar trend was observed for the release profile in DPBS associated with PpIX-AgNPs after light irradiation with a burst release in the first 20 minutes (release rate = 19.18 μg L^{-1} min^{-1}) followed by a steady release (release rate = 0.08 μg L^{-1} min^{-1}) during the rest of the experiment (**Figure 2.3b**). In the case of PEI-PpIX-AgNPs, a similar two stages release behavior

was observed; first the burst release (release rate = 13.53 μg L^{-1} min^{-1}) followed by a steady phase (release rate = 0.11 μg L^{-1} min^{-1}) (**Figure 2.3b**, Figure S6). Interestingly, in DPBS the interaction between Ag^+ and amine groups seems that is not strong enough to completely stop the release of the Ag^+ ions. It has been reported that the different ions in DPBS (e.g., KCl, NaCl, KH_2PO_4, and Na_2HPO_4) can have a screening effect on the interaction between Ag^+ and the amines [152, 159, 160]. Finally, a constant release of Ag^+ from AgNPs is observed (release rate = 0.12 μg L^{-1} min^{-1}) during the whole experiment (**Figure 2.3b**). The total amount of Ag^+ released was 25, 60, and 50% wt for AgNPs, PpIX-AgNPs, and PEI-PpIX-AgNPs, respectively (Figure S8). These amounts are at least 2.5 times higher than the one obtained in water, as an indication that different media has a significant impact on the release of Ag^+ [136, 161]. It has been reported that the presence of NaCl in the aqueous media could have an impact on the rate of dissolution of Ag^+ [162]. Therefore, we hypothesize that the presence of Cl^- ions can account for some of the Ag^+ release differences between water and DPBS observed in this work [163]. Control experiments for PpIX-AgNPs and PEI-PpIX-AgNPs in DPBS without light irradiation only show a steady release of Ag^+ ions, which is like the one observed for AgNPs (Figure S7b).

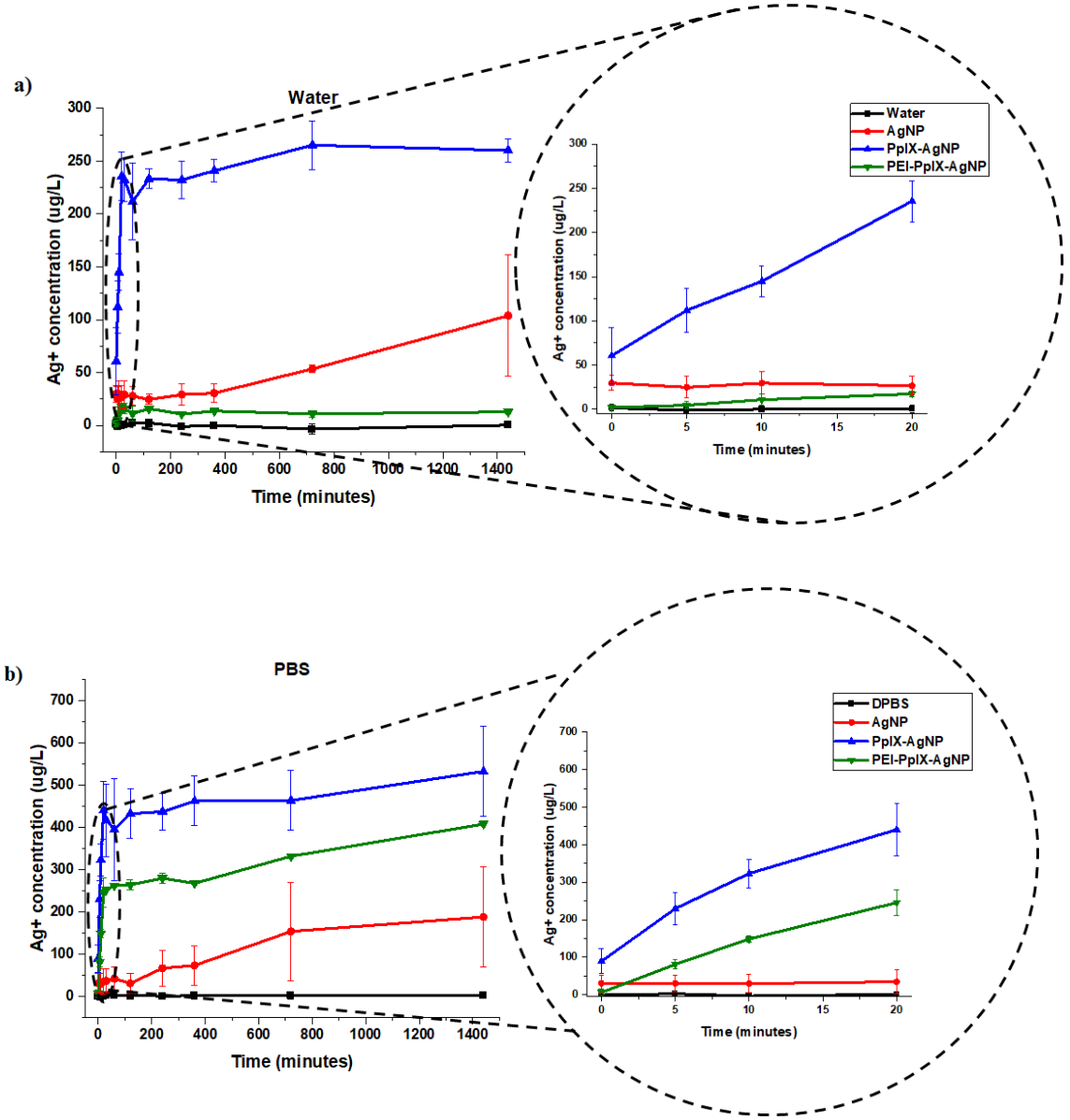

Figure 2.3 Ag^{+} release kinetics for AgNPs, PpIX-AgNPs and PEI-PpIX-AgNPs measured in a) water or b) DPBS. A zoom-in of the first 20 minutes are localized on the right.

2.3.3 Bacteria inactivation

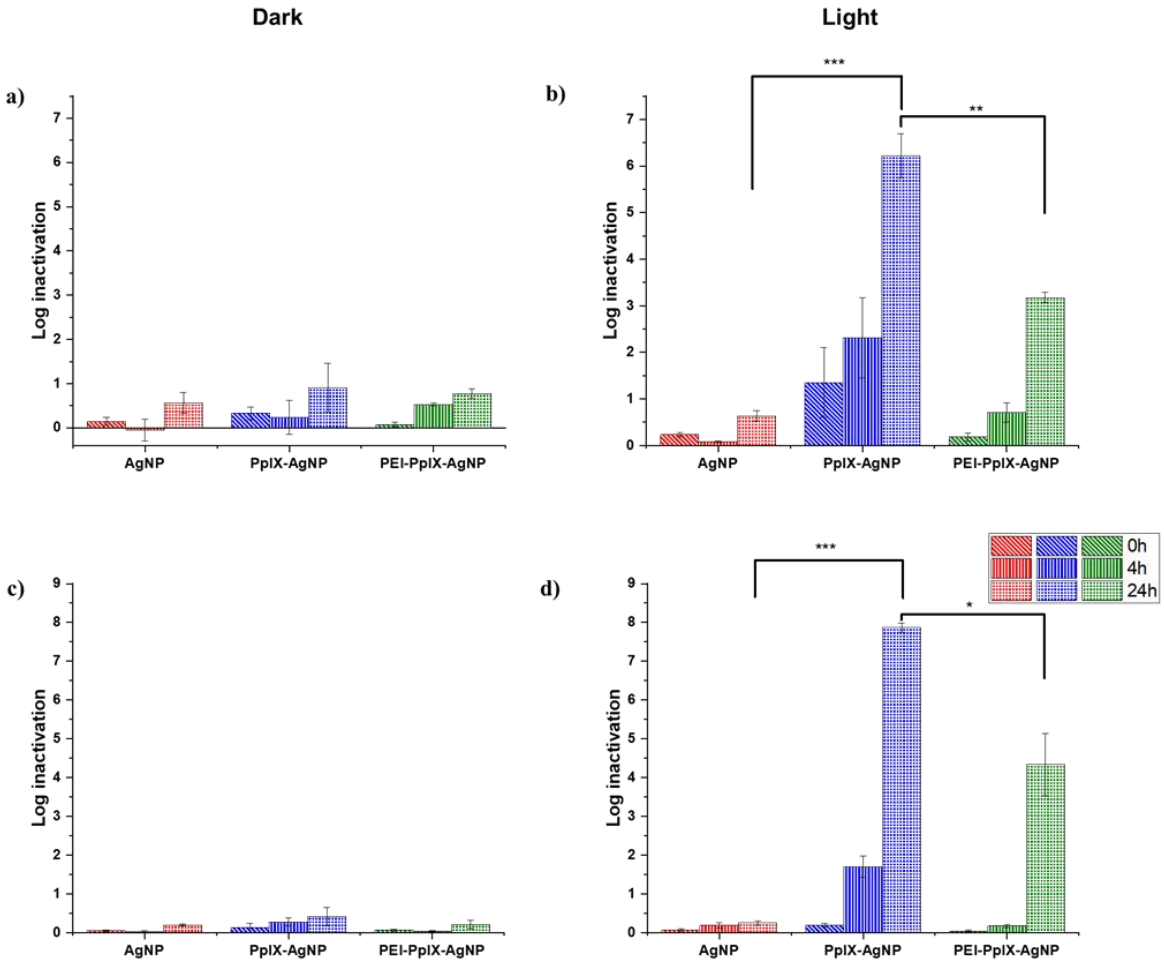

Figure 2.4 Inactivation of MRSA (a-b) and MDR E. coli (c-d) under light-activated conditions (400–700 nm; 56 ± 2 mW/cm2). The time point 0 h indicates the inactivation achieved after light irradiation for 20 min. The other two time points; 4 and 24 h show the bactericidal effect post-irradiation. Error bar is the standard error of mean (SEM) of three independent replicate experiments. All the statistical analyses were performed with α = 0.05 and reported as stars assigned to the p-values: ***$p \leq 0.0001$, **$p \leq 0.001$, *$p \leq 0.05$, and ns $p > 0.05$.

MRSA and MDR *E. coli* are one of the most common causes of human and animal antibiotic resistant infections [25, 125, 164]. These pathogens are considered as serious threats by the Centers for Disease Control and Prevention (CDC) and are part of the "nine bacteria of international concern" [3, 5]. Therefore, MDR *E. coli* and MRSA are ranked in the Priority 1 and 2 of the World Priority List of ARB for R&D of new antibiotics by the World Health Organization (WHO) [3]. The antimicrobial properties of AgNPs, PpIX-AgNPs and PEI-PpIX-AgNPs were tested against MRSA (ATCC BAA 44 strain) and a wild type MDR *E. coli*. The log bacterial inactivation achieved using these NPs under dark and light conditions are presented in **Figure 2.4**. For all cases, the concentration of AgNPs in all samples was kept constant at 1.5 μg/mL while cysPpIX concentration was 1μM in PpIX-AgNPs and PEI-PpIX-AgNPs. These concentrations were chosen based on the results from preliminary concentration optimization experiments. All microbes were incubated with NPs in the dark for 30 min prior to visible light irradiation (400–700 nm; 56 ± 2 mW/cm^2) for 20 min. Subsequently, samples were collected post-irradiation at 0 h (i.e., immediately after irradiation), 4 h and 24 h post-irradiation. A similar protocol was followed for the dark controls. The results indicate that 1.5 μg/mL of AgNPs achieved < 1-log inactivation of MRSA both under light and dark conditions even after 24 h of exposure (**Figures 2.4a** and 3b). For PpIX-AgNPs, under dark conditions at times 0, 4 and 24 h, the log inactivation was like that obtained for AgNPs. This low inactivation by AgNPs at 1.5 μg/mL was expected because typical minimum inhibitory concentrations (MIC) reported for MRSA using AgNPs of similar sizes used in this study are about 3-10 folds higher [131, 165]. However, MRSA inactivation by PpIX-AgNPs increased to ~1.5-log following immediate irradiation for 20 min (i.e., 0 h) and continuously increased to 2.3-log and 6.2-log after 4 h and 24 h contact time, respectively. PpIX-AgNPs achieved the highest inactivation of MRSA amongst the three NPs examined regardless of the

contact time ($p \leq 0.0001$) (**Figure 2.4b**). Control experiments using only the parent porphyrin (cysPpIX) in the presence of light show an inactivation of ~2.5-log following immediate irradiation (Figure S10b). Nevertheless, this effect remained constant during the rest of the experiment. Most likely due to the short half-life ($<10^{-6}$s) of the ROS species generated, which are the antibacterial agents [166, 167].

The inactivation of the Gram-negative MDR *E. coli* showed a similar trend as the inactivation of the Gram-positive MRSA. Under dark conditions, the log inactivation was <0.5-log for all three NPs for time 0, 4 and 24 h (**Figure 2.4c**). Similarly, PpIX-AgNPs achieved the highest inactivation of ~8-logs after 24 h under light conditions ($p \leq 0.0001$), which is the limit of quantification since the starting bacteria concentration ~10^8 CFU/mL (**Figure 2.4d**). Interestingly, control experiments using only cysPpIX in the presence of light showed no inactivation of MDR *E. coli* (Figure S10d) as an indication that for this microbe PDI is not effective. Previous studies have shown that some bacteria show resistance against PDI [139, 160, 168]. The increase in bacterial inactivation of MRSA and MDR *E. coli* by PpIX-AgNPs following light irradiation is consistent with the patterns recorded in literature [124, 128-131, 146]. Also, other studies have reported complete elimination of MRSA and *E. coli* using AgNPs only; however, MIC are at least 5 µg/mL depending on the physiochemical properties of the examined AgNPs [62, 131, 165, 169]. Whereas, in this study, only 1.5 µg/mL of AgNPs in PpIX-AgNPs resulted in complete inactivation of MRSA and MDR *E. coli.* These results confirm the synergistic effect between PpIX and AgNPs to effectively eliminate MRSA and MDR *E. coli*.

To deconvolute the impact on the inactivation of MRSA and MDR *E. coli* by using the nanoparticulate platform PpIX-AgNPs, we evaluated the physical mixture of cysPpIX and Ag^+ ($AgNO_3$) at the same concentrations used for the experiments with the NPs (Figure S9). For

MRSA, under dark conditions, the log inactivation was <0.5-log, <1.0-log, and 4.5-log for times 0, 4, and 24 h. In the presence of light irradiation, the inactivation values for the same times are 4.0-log, 4.0-log, and 6.0-log (Figure S9b). These data show: first, that Ag^{+} ions by themselves require time to produce inactivation on MRSA; and second, that PDI has an additive effect at short times (0 and 4 h) of the experiment. In the case of MDR *E. coli* in the absence of light, the log inactivation was zero, <1.0-log, and 6.5-log for times 0, 4, and 24 h, which are the same inactivation values in the presence of light irradiation (Figure S9d). These results confirmed the lack of PDI effect on the elimination of MDR *E. coli*. PpIX-AgNPs have a similar behavior against MRSA as the physical mixture (Figure S9b); nevertheless, it performs better in the case of MDR *E. coli* (Figure S9d).

The incorporation of positive charges in PSs or NPs has been an important strategy to enhance their antimicrobial properties [139, 170, 171]. The rationale is that electrostatic interaction between the positively charged agents and the negatively charged surface of bacteria will bring them in close proximity, resulting in an improved antimicrobial effect [139, 160]. In this work, we functionalized PpIX-AgNPs with PEI polymer (MW = 10KDa) (PEI-PpIX-AgNPs), which contains amine groups that are protonated under physiological conditions. Therefore, it is expected that this strategy would enhance the antimicrobial effect of PpIX-AgNPs [172, 173]. For MRSA, under dark conditions, the log inactivation was <1.0-log for PEI-PpIX-AgNPs at times 0, 4 and 24 h (Figure 2.4a). In the presence of light, only at 24 h a significant increase of inactivation was observed (3.2-log), but not comparable with the value for PpIX-AgNPs ($p \leq 0.001$) (**Figure 2.4b**). PEI-PpIX-AgNPs depicted a similar performance in the case of MDR *E. coli* with minimal inactivation effect in the absence of light (<0.5-log) (**Figure 2.4c**) and lower increase after light irradiation (4.0-log at 24 h) as compared with PpIX-AgNPs ($p \leq 0.05$) (**Figure 2.4d**). Control

experiments using only PEI polymer depicted ~0.5-log and ~1.0-log inactivation of MRSA and MDR *E. coli*, respectively, under light or dark conditions (Figure S9). The experimental results reveal that by modifying the surface of PpIX-AgNPs with PEI did not enhance their antimicrobial effect; on the contrary, a reduction in the inactivation was observed. This lower antimicrobial activity of PEI-PpIX-AgNPs compared to PpIX-AgNPs can be explained by the lower concentration of Ag^+ released by PEI-PpIX-AgNPs as illustrated in the previous section (**Figure 2.3b**). This unexpected outcome suggests that different considerations other than functionalizing the surface of nanoparticles with groups that can render positive charge to the surface such as amines need to be considered in the case of AgNP-based platforms that depend on the release of Ag^+ to inactivate ARB.

Overall, the log inactivation of MRSA and MDR *E. coli* was in the order PpIX-AgNPs > PEI-PpIX-AgNPs > AgNPs under light conditions irrespective of the contact time (**Figures 2.4b and 2.4d**). The order of bacterial log inactivation correlates with the trend of Ag^+ release profile (PpIX-AgNPs > PEI-PpIX-AgNPs > AgNPs) in DPBS (**Figures 2.3a and 2.3b**) as a clear indication that the antimicrobial activity of this platform is driven by photo-active release of Ag^+.

2.3.4 Cytotoxicity in mammalian cells

Antimicrobial agents should effectively eliminate bacteria without major toxicity toward mammalian cells. This feature is critical in biomedical applications such as wound healing [129]. In this work, an *in vitro* assay was carried out to evaluate the cytotoxicity of AgNPs, PpIX-AgNPs and PEI-PpIX-AgNPs at bacterial inhibitory concentration in HeLa cells. After 30 min incubation with the NPs, cells were irradiated for 20 min, followed by an additional 24 h of incubation at 37 °C. The viability of HeLa cells after treatment with any of the NPs did not show any phototoxic effect at the concentrations used to eliminate MRSA and MDR *E. coli* (**Figure 2.5**). The same

behaviour was observed under dark conditions. Control experiments using cysPpIX, $AgNO_3$ and the physical mixture of both show a major cytotoxic effect for both cysPpIX and the physical mixture in the presence of light (Figure S10). This phototoxic effect is most likely due to the photodynamic therapy (PDT) properties of cysPpIX [174, 175]. Interestingly, neither PpIX-AgNPs nor PEI-PpIX-AgNPs show PDT effect against HeLa cells, most likely because most of the $^1O_2$ generated by the PS reacts with the surface of AgNPs. Similar "quenching" effects have been observed in other NPs carrying PSs [129, 130, 146, 176]. Control experiments also demonstrate that the concentration of Ag^+ used to eliminate bacteria is not toxic to HeLa cells. It is reported that the IC_{50} of Ag^+ is usually higher for mammalian cells than for bacteria [129-131, 146]. Therefore, the PpIX-AgNP platform not only offers an effective approach to eliminate MRSA and MDR *E. coli*, but also shows improved biocompatibility properties against mammalian cells.

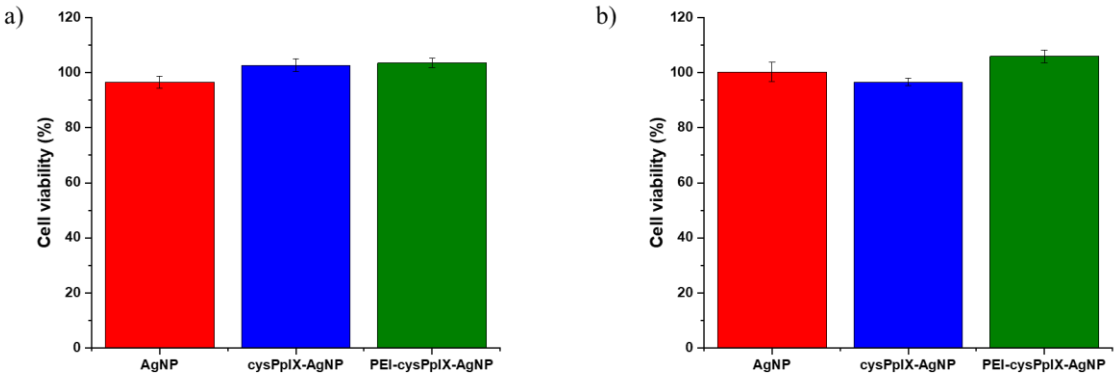

Figure 2.5 Cytotoxicity in mammalian cancer cells (Hela) in the (a) absence and (b) presence of light.

2.4 Conclusions

In this work, we synthesized, characterized and applied a light-activated PpIX-AgNP platform for elimination of ARB. PpIX-AgNPs demonstrated broad-spectrum antibacterial action

resulting in > 7 log inactivation of MRSA and MDR *E. coli*. The bacterial inactivation achieved was independent of the Gram-stain classification of the examined bacterial strains. The ROS generated, mainly $^1O_2$, due to the irradiation of PpIX increased the release of Ag^+ from the surface of the PpIX-AgNPs. We also investigated the influence of the media composition on the release kinetics of Ag^+. The ionic composition of DPBS increased Ag^+ release with light activated PpIX-AgNPs than in nanopure water. The cationic surface charge associated with PEI-PpIX-AgNP did not improve bacterial inactivation since it did not allow similar Ag^+ release in comparison with PpIX-AgNP. The amount of released Ag^+ drives the inactivation of MDR *E. coli* and MRSA over electrostatic interaction from PpIX-AgNPs. In addition, PpIX-AgNPs overcame the limitations of PpIX molecules in the PDI of MDR *E. coli*. All NPs showed negligible cytotoxicity to HeLa cells at the bacterial inhibitory concentration after 24 h exposure. The successful formulation of light-activated PpIX-AgNPs with increased potential for Ag^+ release would reduce the MIC of AgNPs for therapeutic applications.

2.5 Appendix A (Supporting Information)

Materials and Methods

The following chemicals and biological media were purchased from various suppliers: concentrated hydrochloric acid (Macron chemicals), nitric acid (Macron chemicals), protoporphyrin IX (Enzo Lifesciences). Polyethyleneimine (PEI) (branched, 10 kDa; Beantown chemicals), 1-Ethyl-3-(3-dimethylaminopropyl) carbodiimide hydrochloride (EDC) (Oakwood Chemicals), silver nitrate (AgNO3), silver standard, cysteamine hydrochloride, N-hydroxysuccinimide (NHS), dimethylamino pyridine (DMAP), N,N-Diisopropylethylamine (DIPEA), trisodium citrate dihydrate, 9,10 dimethyl anthracene, 1X phosphate buffer saline solution (10 mM) (all from Sigma Aldrich), tannic acid (95%, Acros Organics), dimethyl sulfoxide,

dimethylformamide (VWR chemicals) and dichloromethane (Alfa aesar), Nano-W negative stain (NanoProbes), Roswell Park Memorial Institute (RPMI) media, Fetal Bovine Serum (FBS), penicillin-streptomycin (pen-strep), 1X Dulbecco's phosphate buffer saline (DPBS) (all from Corning), Luria Bertani (LB) broth, LB agar (VWR Life Science). All chemicals were of reagent grade purity or higher and were used as received. Biological media are certified nuclease-free.

Synthesis of thiol functionalized PpIX (cysPpIX).

The synthesis of cysPpIX is carried through a two-steps reaction as illustrated in Scheme S1. PpIX was initially modified to obtain the succinimide ester derivative (sePpIX) according to the following protocol; 112.5 mg of PpIX (0.2 mmol), 184.2 mg of N-hydroxysuccinimide (NHS) (1.6 mmol), 48.9 mg of dimethylamino pyridine (DMAP) (0.4 mmol) and 306.8 mg of 1-Ethyl-3-(3-dimethylaminopropyl) carbodiimide (EDC) (1.6 mmol) were dissolved in a mixture of 10 mL dimethylsulfoxide and dichloromethane (DMSO:DCM; 1:1 vol.) and stirred at room temperature for 48 h. The sePpIX was obtained via precipitation of the reaction using a mixture of ethanol: water (20:80 %v) and separated using vacuum filtration. The obtained precipitate was dried under vacuum condition and stored at –20 °C.

The sePpIX was further functionalized with cysteamine to afford a thiol functionalized PpIX. Briefly, 40 mg of sePpIX (0.05 mmol), 23 µL of N, N-Diisopropylethylamine (DIPEA) (0.132 mmol) and 15 mg of cysteamine-HCl (0.132 mmol) were mixed in 672 µL of DMSO. This mixture was stirred at 80 °C for 96 h. Following this, the desired product (cysPpIX) was purified using a mixture of ethanol:water (20:80 %v) and dried under vacuum condition.

Characterization

The size and morphology of the synthesized nanoparticles were analyzed using transmission electron microscopy (TEM, JEM 1230) operating at an accelerating voltage of 200 kV. The samples were prepared by dispersing AgNPs and PpIX-AgNPs in 50 µL of ethanol. Then, 10 µL of the sample was placed on the carbon coated copper grid and air dried for 1-2 h. The nanoparticle size and its distribution were calculated using ImageJ software. Sample size of 150 nanoparticles was considered for analysis and size was finally reported as average ± sd.

PEI-PpIX-AgNP (15 ng/µL) in water was well sonicated and 10 µL of the sample was placed on the carbon coated copper grid. After 1-minute, excess sample was wicked off (not to dryness) using filter paper. A single drop (5 uL) of Nano-W stain was added to the grid and excess sample was wicked off after 1-minute. This step was repeated again, and the final grid was air dried for 24 h at room temperature. The nanoparticle size and its distribution were calculated using ImageJ software. Sample size of 100 nanoparticles was considered for analysis and final distribution was plotted as a histogram.

Post-irradiation TEM analysis was performed for AgNPs, PpIX-AgNPs and PEI-PpIX-AgNPs in water and PBS at time points: 0 h, 20 min and 24 h. Petri dishes containing individual samples were irradiated with a white light source (400-700 nm; 56 ± 2 mW/cm2) for 20 min. Then, 200 µL of aliquots were collected at time points 20 min and 24 h. The collected aliquots were immediately centrifuged for 10 min at 13000 rpm and the pellet was used for TEM analysis. The pellet obtained was sonicated for 5 min and 10 µL of this sample was placed on the carbon-coated copper grid. After 5 min, excess volume was wicked off using filter paper and the grids were dried in the oven for 2 h at 150 °C.

Hydrodynamic size, polydispersity index (PdI) as well surface charge determination was performed using Malvern ZetaSizer. UV-Vis spectra were obtained using Cary 300 Bio UV-Visible

spectrophotometer (Varian). 3 mL of sample and reference solvent (DMF) was used to obtain absorbance spectra from 200-800 nm. Furthermore, chemical changes confirming PpIX modifications were analyzed using MALDI-MS, 1H NMR and FTIR.

sePpIX: 1H NMR (300 MHz, DMSO-d6, ppm): δ 2.74 (s, 8H), 3.17 (t, 4H), 3.64-3.77 (s, 12H), 4.50 (t, 4H), 6.44-6.50 (dd, 4H), 8.48-8.60 (m, 2H), 10.27-10.38 (4s, 4H). FT-IR (cm-1): 3318 (N-H), 2947 (C-H), 1810 (C=O), 1778 (C=O), 1739 (C=O), 1627 (CN); MALDI-MS (m/z): Calculated: [M]+ = 756.30; Observed: [M+2]+ = 758.44.

cysPpIX: 1H NMR (300 MHz, DMSO-d6, ppm): 3.19 (t, 4H), 3.59-3.63 (dd, 12H), 3.72 (m, 4H), 4.03 (m, 2H), 4.34 (t, 4H), 6.19-6.44 (dd, 4H), 8.16-8.43 (m, 2H), 10.18-10.29 (d, 4H). IR (cm-1): 3312 (N-H), 2913 (C-H), 1741 (C=O), 1643 (C-N). Calculated: [M]+ = 680.29; Observed: [M-2] + = 678.90.

Photophysical characterization of PpIX conjugated AgNPs was performed by determining the 1O2 quantum yield (ΦΔ). Singlet oxygen generation was quantified by monitoring the absorbance decay of 9,10 dimethylanthracene (DMA). The following protocol was carried put; 1 mL of 5 µM of PS in DMF (PpIX, cysPpIX and PpIX-AgNPs) was mixed with 1 mL of 50 µM of DMA in DMF in quartz cuvettes (1cm x 1cm). Extreme care was taken to not expose the mixture to any light. This mixture was irradiated at 515 nm for varying time interval (0, 1, 2, 5, 10, 20 and 30 min) using a spectrofluorometer (Shimadzu RF 5301). The decay in absorbance 380 nm was monitored by measuring its UV-Vis spectra immediately after light irradiation and was plotted against the irradiation time. TPP in DMF was used as the reference (ΦΔ = 0.62).

2.5.1 Supporting Schemes

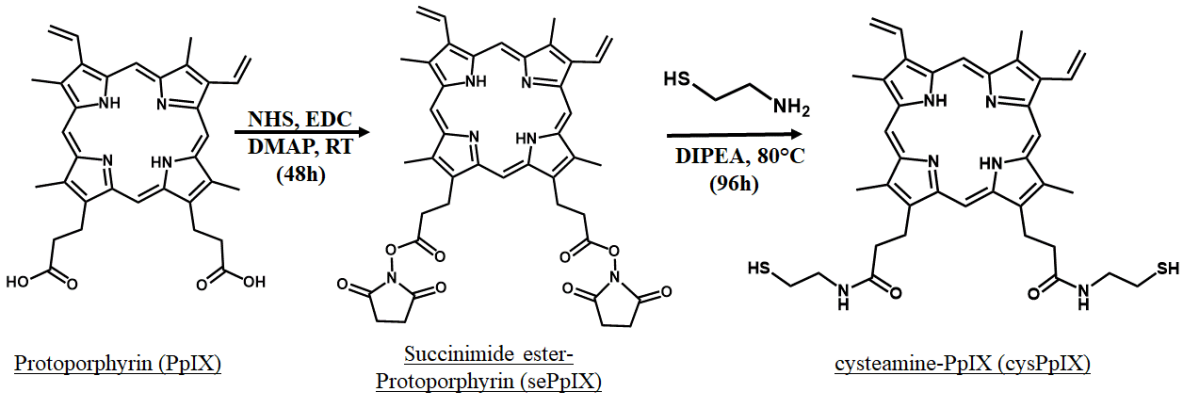

Scheme S1: Synthesis of cysPpIX following a two-steps approach. First, the carboxylic acid groups in PpIX were activated using NHS followed by the nucleophilic acyl substitution reaction using cysteamine.

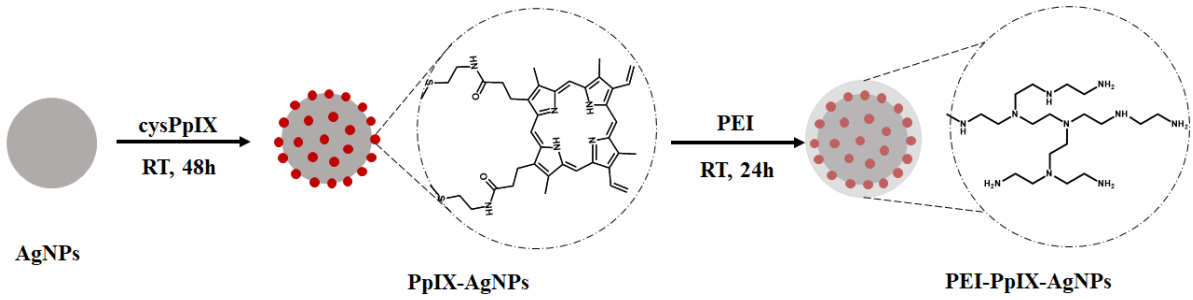

Scheme S2. Fabrication of PpIX-AgNPs and PEI-PpIX-AgNPs.

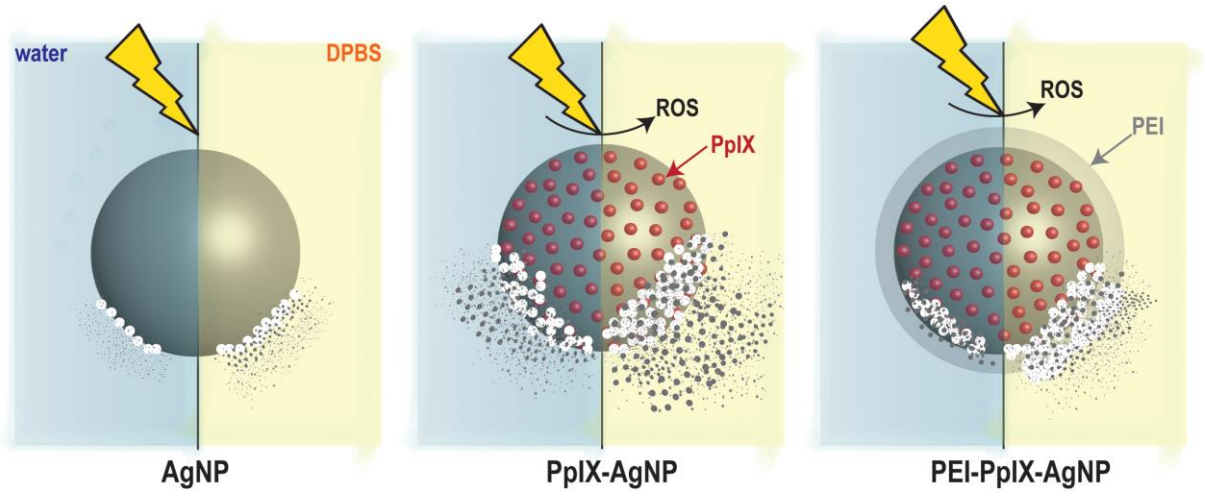

Scheme S3. Schematic representation of the degradation of AgNPs, PpIX-AgNPs and PEI-PpIX-AgNPs in the presence of light in water or DPBS conditions. AgNPs are usually degraded by the medium regardless the presence or absence of light. The ions in DPBS in increase the solubility of Ag+, which results in the enhancement of the degradation of AgNPs. The presence of the PpIX photosensitiser upon light irradiation accelerates the degradation of AgNPs. The presence of PEI polymer partially inhibits the degradation of AgNPs

2.5.2 Supporting Figures

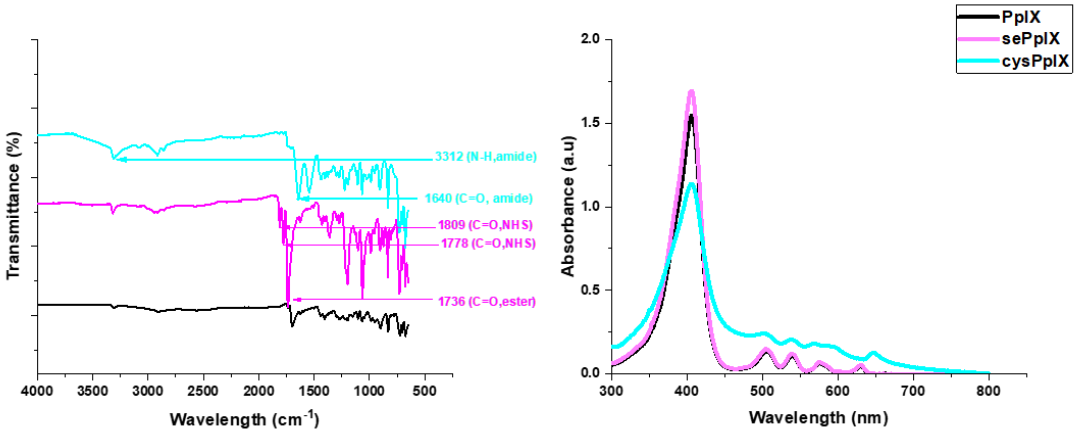

Figure S1. (a) FT-IR and (b) UV-Vis (DMF) spectra for PpIX (black), sePpIX (pink) and cysPpIX (blue).

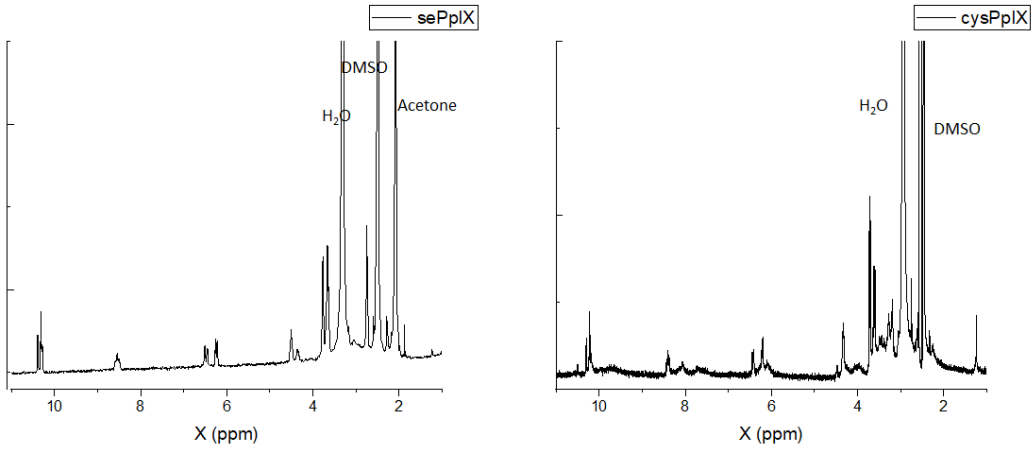

Figure S2. ^{1}H-NMR spectra for sePpIX and cysPpIX.

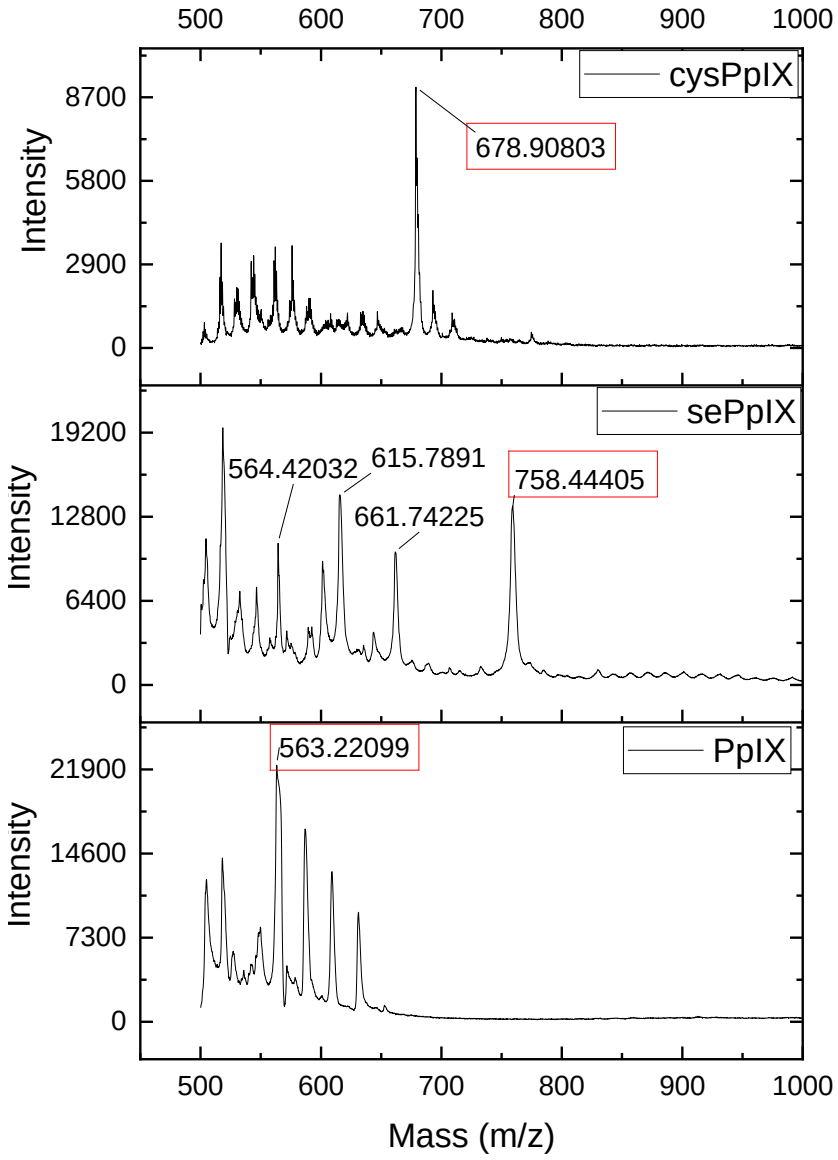

Figure S3. MALDI-MS spectra for PpIX, sePpIX and cysPpIX. Expected m/z: $[PpIX]^+$ = 562.25 / Observed: m/z: $[PpIX+1]^+$ = 563.22; Expected m/z: $[sePpIX]^+$ = 756.30/Observed: m/z: $[sePpIX+2]^+$ = 758.44; Expected m/z: $[cysPpIX]^+$ = 680.29/ Observed: m/z: $[cysPpIX-2]^+$ = 678.90.

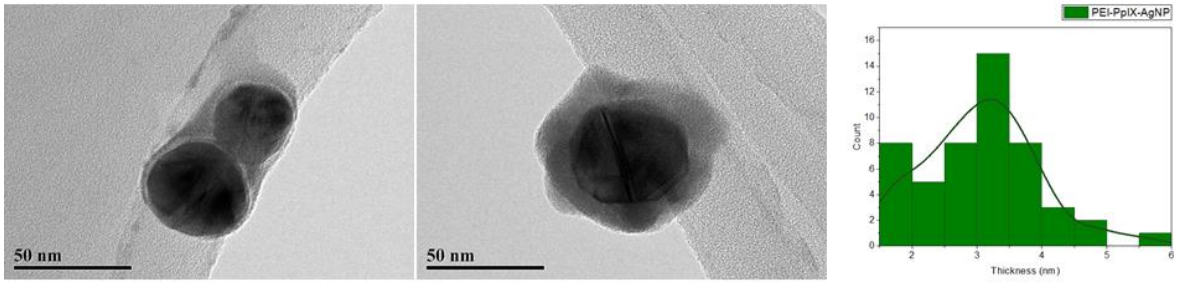

Figure S4. TEM image of PEI-PpIX-AgNPs negatively stained to show the presence of PEI. The thickness of PEI shell was measured using the TEM images obtaining an average of 3.0 ± 0.9 nm (n=50).

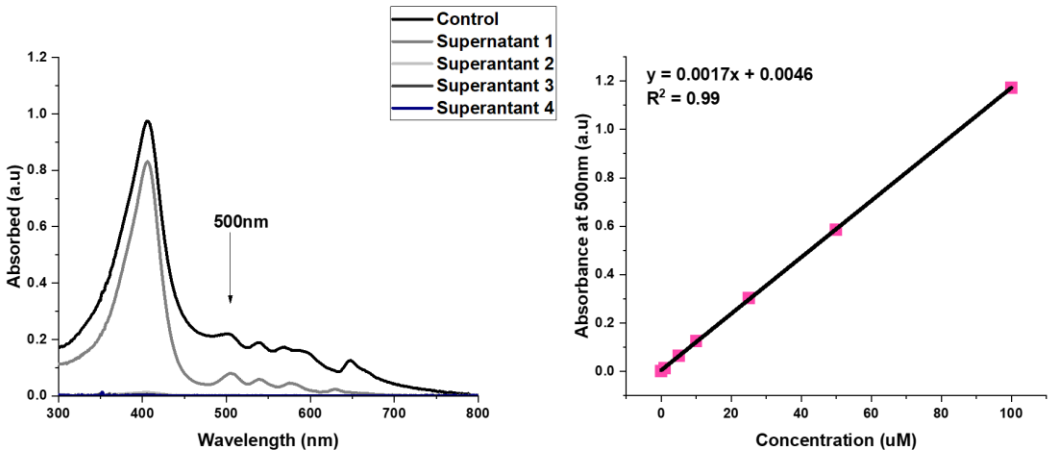

Figure S5. (left) UV-Vis plot for supernatants collected before (control) and after (Supernatant 1-4) the reaction between cysPpIX and AgNP. (right) Calibration curve for the quantification of cysPpIX on AgNP.

Equation 1

$$\%\ PpIX\ loaded = \frac{cysPpIX\ before\ reaction(mg) - cysPpIX\ in\ the\ supernatants, S1 - S4\ (mg)}{cysPpIX\ before\ reaction\ (mg)}$$

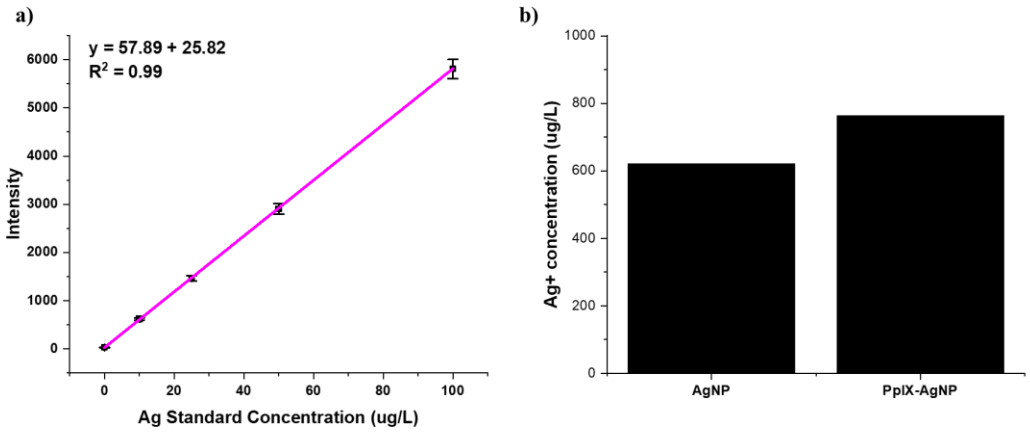

Figure S6. a) Calibration curve for Ag^+ digestion and release experiments. b) Maximum Ag^+ in 1.5 µg/mL of AgNP and PpIX-AgNP obtained after digestion.

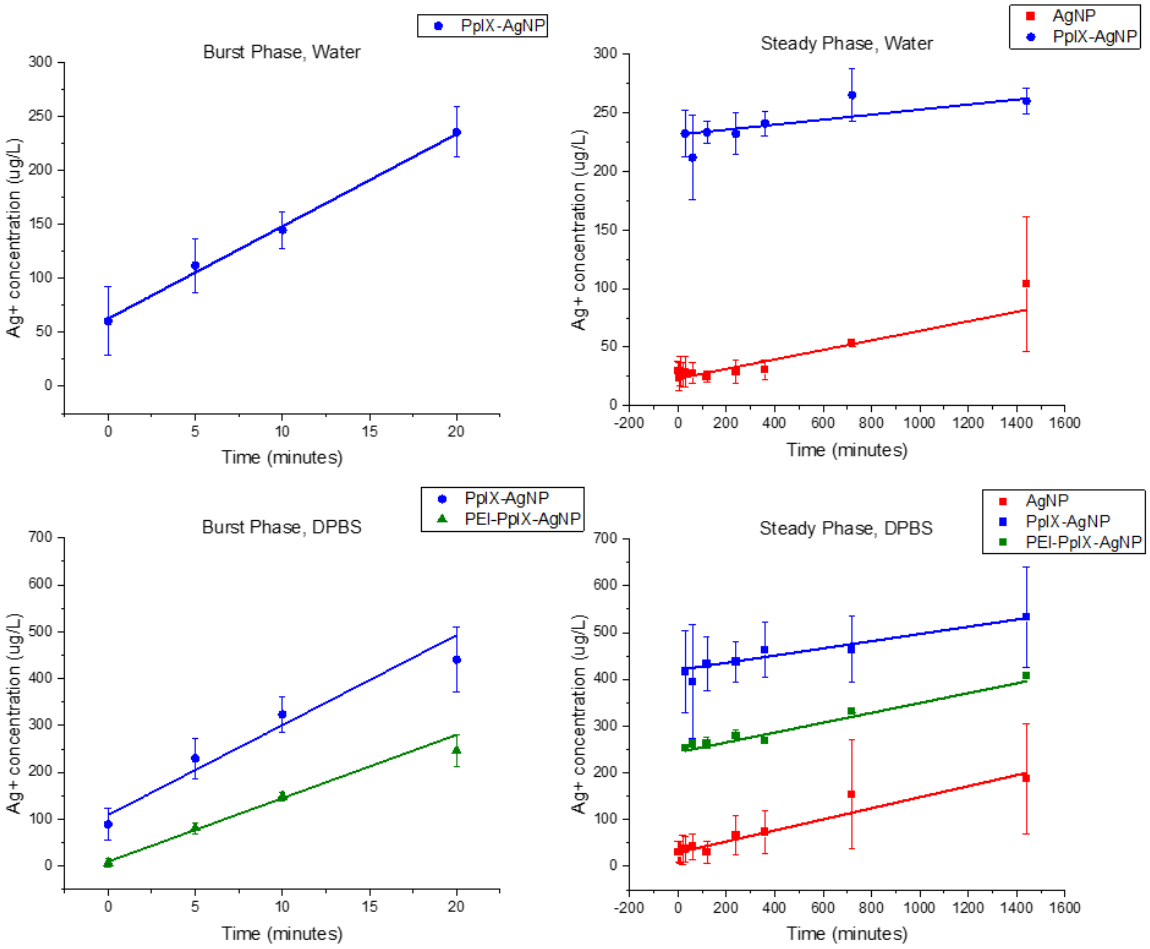

Figure S7. Kinetic release linear fitted plots for AgNP, PpIX-AgNP and PEI-PpIX-AgNP in water and DPBS represented as burst and steady release phase.

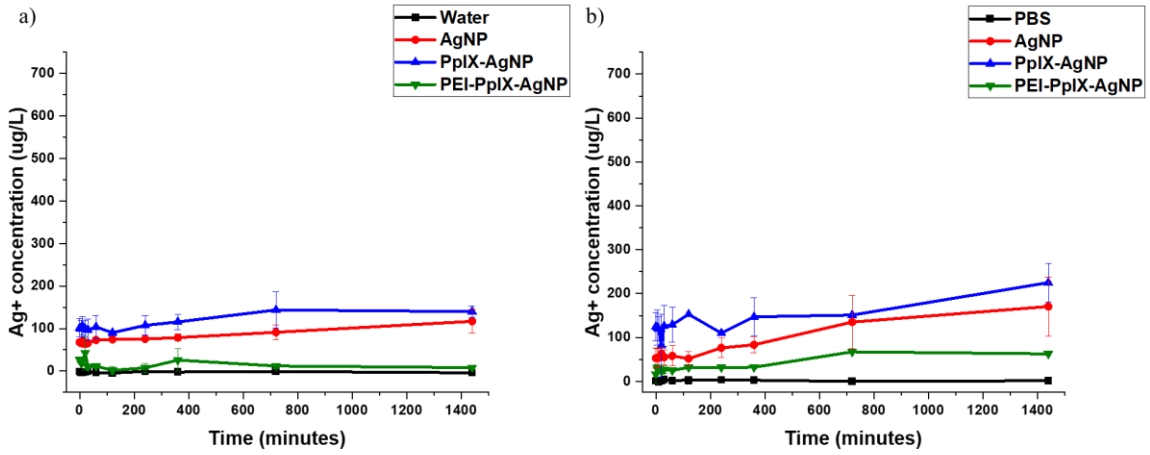

Figure S8. Ag^{+} release kinetics in the absence of light for AgNPs, PpIX-AgNPs and PEI-PpIX-AgNPs measured in a) water and b) DPBS.

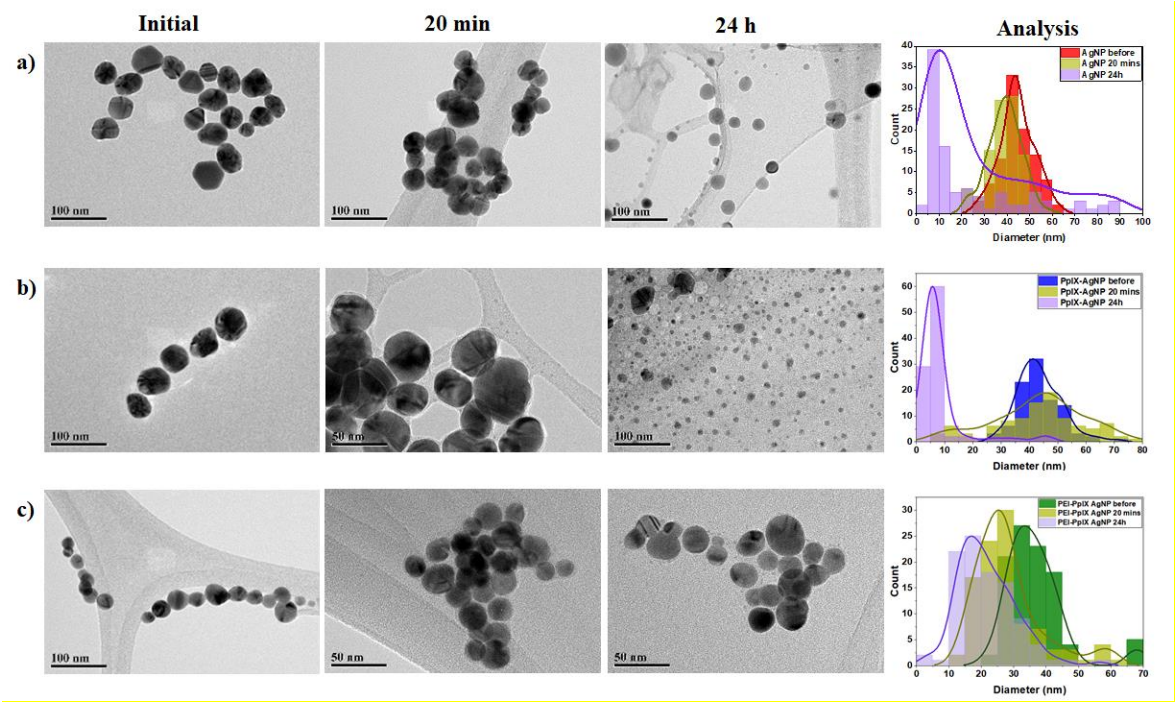

Figure S9. TEM images and quantification of the degradation of a) AgNPs, b) PpIX-AgNPs and c) PEI-PpIX-AgNPs in water post-light irradiation at 20 min and 24 h. Nanoparticles diameter was measured using Image J and plotted to determine the change in size distribution (n = 100).

Equation 2

$$\%\ Ag + release = \frac{Ag + released\ at\ time\ point\ 't'\ (\frac{\mu g}{L})}{Total\ Ag + digested\ (\frac{\mu g}{L})}$$

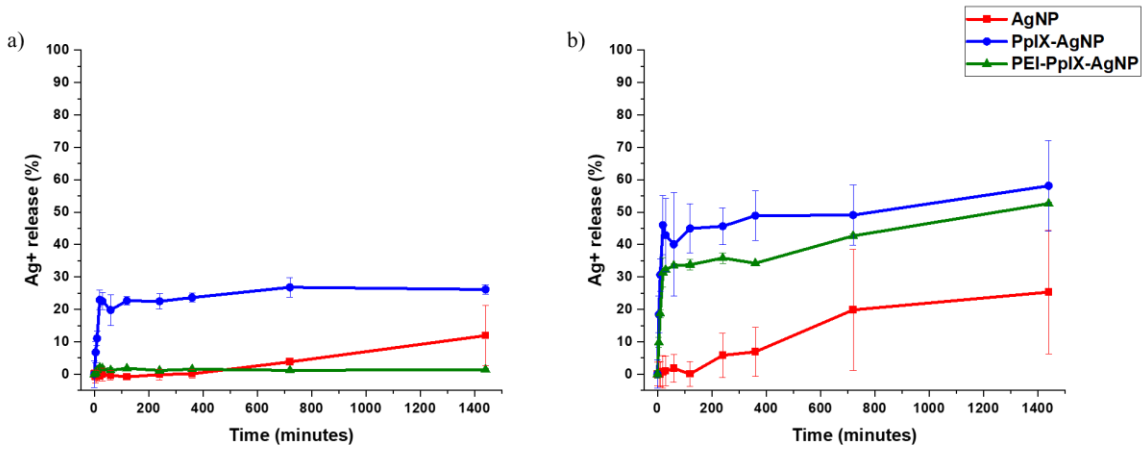

Figure S10. Ag^{+} release kinetic in a) water and b) DPBS expressed in % using the total amount of Ag in the nanoparticles for AgNPs, PpIX-AgNPs and PEI-PpIX-AgNPs. Ag+ release percentage was calculated using equation 2.

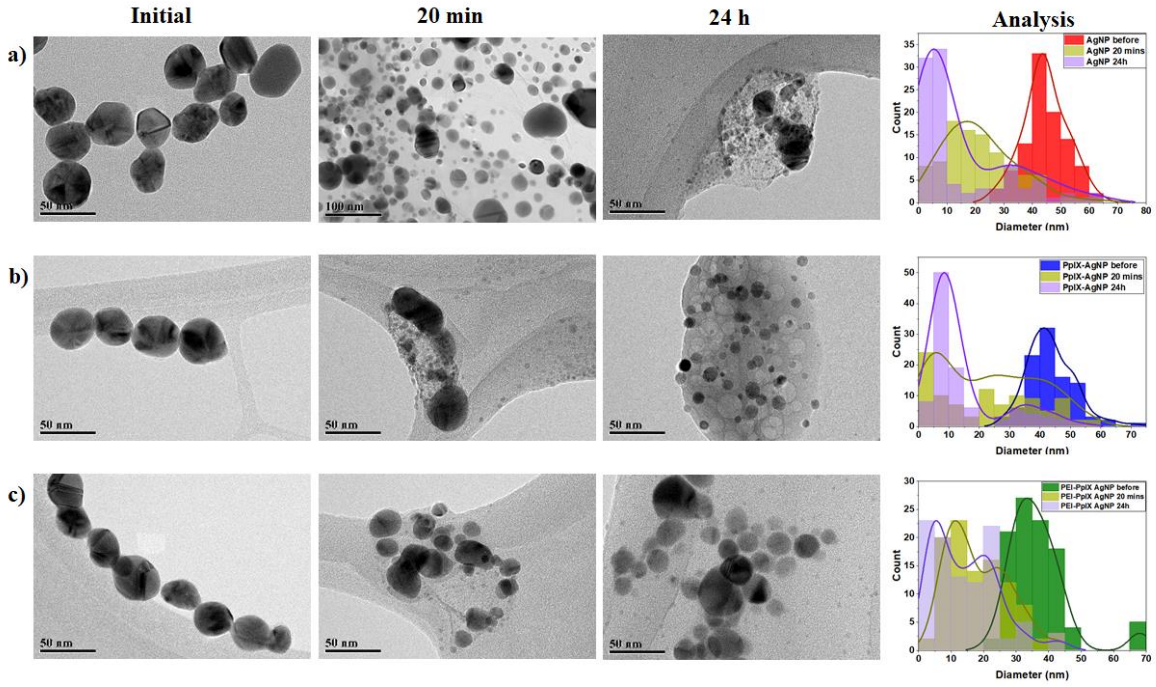

Figure S11. TEM images and quantification of the degradation of a) AgNPs, b) PpIX-AgNPs and c) PEI-PpIX-AgNPs in DPBS post-light irradiation at 20 min and 24 h. Nanoparticles diameter was measured using Image J and plotted to determine the change in size distribution (n = 100).

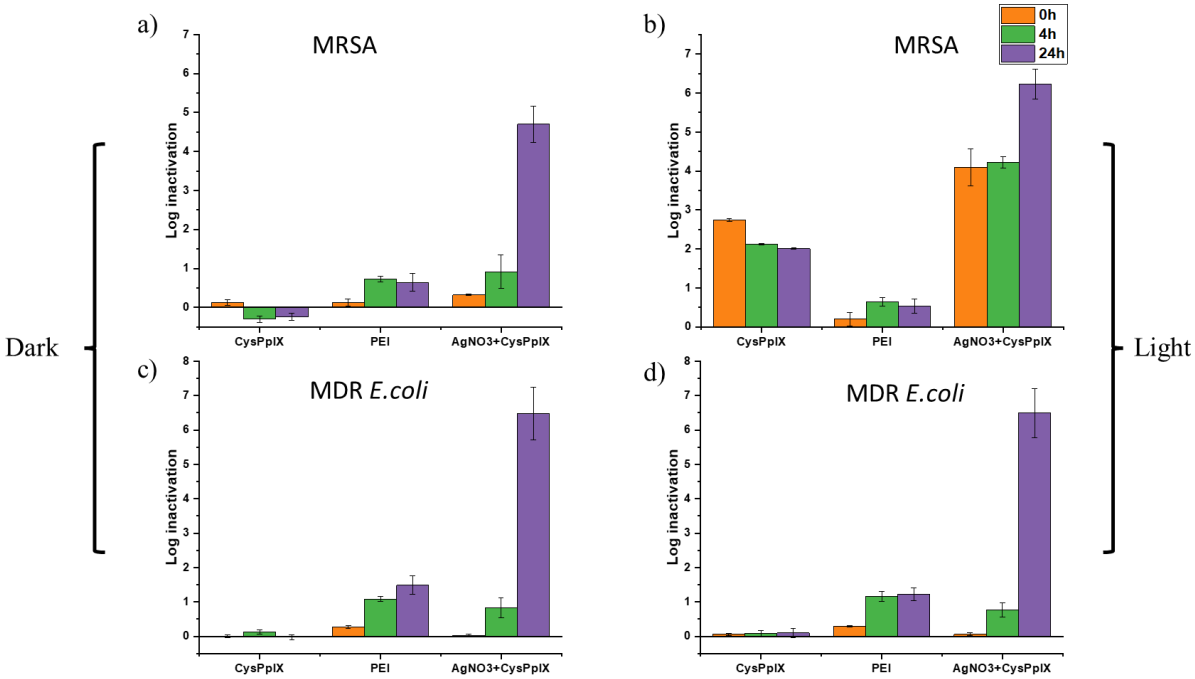

Figure S12. Antibacterial activity of controls tested in MRSA and MDR *E. coli* under light and dark conditions.

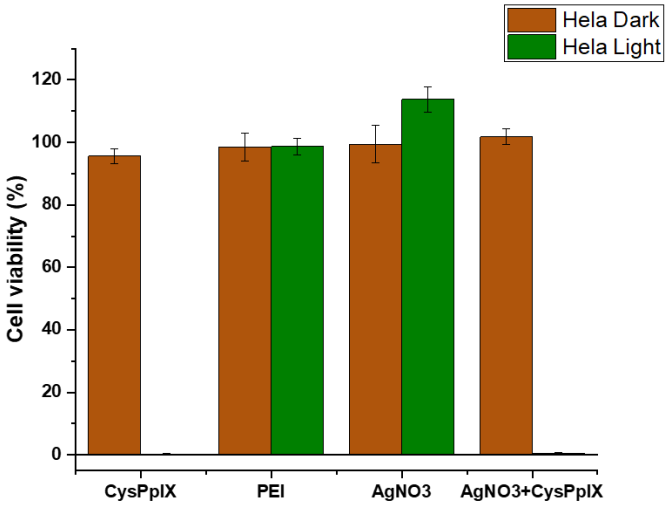

Figure S13. Cytotoxicity of the controls (cysPpIX, AgNO3, cysPpIX+AgNO3, PEI) tested in Hela cells in the presence (light) and absence (dark) of blue light.

2.5.3 TABLES

Table S1. ICP-OES digestion results for AgNPs, PpIX-AgNPs and PEI-PpIX-AgNPs.

Sample	**Digested Ag^+ (ug)**	**Ag^+ per ug of NP (%)**
AgNP	48.9 ± 1.8	97.77
PpIX-AgNP	28.8 ± 2.6	57.60
PEI-PpIX-AgNP	15.0 ± 0.7	29.92

Table S2. Summary of hydrodynamic size/polydispersity index (PdI) and ζ-potential for AgNPs, PpIX-AgNPs and PEI-PpIX-AgNPs.

Sample Name	Hydrodynamic Size (nm)	PdI	ζ- potential (mV)
AgNP	36.34 ± 1.11	0.2	-49.08 ± 5.48
PpIX-AgNP	55.60 ± 6.68	0.43	-57.28 ± 4.77
PEI-PpIX-AgNP	137.59 ± 3.99	0.29	27.11 ± 1.71

Table S3. Singlet oxygen quantum yield analysis (Φ_Δ) using TPP (DMF) as the reference (Φ_Δ = 0.62). λ_{ex} = 515nm.

Sample	**Φ_Δ**
PpIX	0.60
CysPpIX	0.38
AgNP-PpIX	0.01

Table S4. Summary of linear fitting parameters for AgNP, PpIX-AgNP and PEI-PpIX-AgNP.

			Slope	R^2
AgNP	Water		0.04	0.92
	DPBS		0.12	0.87
PpIX-AgNP	Water	Burst Phase	8.56	0.99
		Steady Phase	0.02	0.81
	DPBS	Burst Phase	19.18	0.95
		Steady Phase	0.08	0.87
PEI-PpIX-AgNP	DPBS	Burst Phase	13.53	0.99
		Steady Phase	0.11	0.92

3 CHAPTER 3: IMPACT OF PROTEIN CORONA AND LIGHT MODULATION ON THE ANTIBACTERIAL ACTIVITY OF LIGHT-ACTIVATED SILVER NANOPARTICLES

3.1 Introduction

The rise of antibiotic-resistant bacteria (ARBs) has become one of the prevalent public health threats worldwide. In 2019, ARBs were directly responsible for 1.27 million deaths [7, 8]. The persistent failure of antibiotics and their pipeline crisis have compelled researchers to look at non-antibiotic alternatives. Nanomaterials have aroused a great interest in the field of antibacterials [177]. Metal nanoparticles, nanozymes, and metal-organic complexes have been rationally designed and developed for antibacterial applications [50-52, 59, 178, 179]. Among them, silver nanoparticles (AgNPs) have shown promising outcomes due to broad-spectrum antibacterial activity reactive oxygen species (ROS) generation, disruption of the bacterial cell membrane, interference in the metabolic and DNA replication pathways, and denaturation of sulfur-containing proteins [52, 54, 58]. The release of silver ions (Ag^+) plays an essential role in contributing to the antibacterial activity of AgNPs [92]. The Ag^+ release from AgNPs can be regulated based on the physiochemical properties of NP, environmental conditions, and external triggers such as light [92]. Among the environmental conditions, nutrient-rich medium, pH, or ionic strength affects the AgNP colloidal stability and Ag^+ release. Proteins in bacterial medium tend to associate with the surface of nanoparticles, forming a protein layer around it, a phenomenon termed “protein corona” [180]. This NP-protein interaction is a dynamic process affecting the stability and biological identity of the NP. It is governed by the physicochemical properties of NP, such as size, morphology, and surface coating [181]. Proteins with high affinity to the surface of the NPs are typically associated with the innermost hard corona. However, the ones with low affinity are localized in the outermost soft corona [182]. In

the case of AgNPs, several studies have also reported that protein corona impacts the release of silver ions and their colloidal stability, thereby hindering AgNP's antibacterial activity [68, 180, 183-185]. Vasquez detailed the role of various bacteria culture media on the stability of AgNPs and their subsequent antibacterial activity [68]. The authors emphasized that the "chemical complexity" (diversity in the range of culture components) and composition of the bacterial medium can be correlated to the minimum inhibitory concentration (MIC) in the *E. coli* strain. Therefore, at lower peptone concentrations and minimal "chemical complexity" in the bacterial medium, the MIC of *E. coli* in the presence of AgNPs reaches the lowest value, which means a more substantial bactericidal effect. However, a systematic investigation is needed to understand the correlation of Ag^+ release to the culture conditions.

Recently, some studies have reported the synergistic antibacterial effect of combining a photosensitizer (PS) with AgNPs (PS-AgNPs) [86, 96, 101, 114, 116]. PSs are molecules that absorb light at specific wavelengths, which later transfer that energy to oxygen to generate ROS [40, 41, 43]. The studies assert that the antibacterial synergy of PS-AgNPs mainly originates from enhanced light-mediated ROS generation. However, only a few studies have shown that light-induced ROS also increases Ag^+ release due to the oxidation of the AgNP surface [77, 95]. Our group reported on the Ag^+ release kinetic from light-activated AgNPs in aqueous media to understand the role of Ag^+ in the antibacterial outcome [94]. We concluded that the Ag^+ release was more pronounced in with higher ionic strength (Dulbecco's phosphate buffer saline, DPBS) than in nanopure water, resulting in up to ~7-8 log inactivation of methicillin-resistant *Staphylococcus aureus* strain (MRSA) and a wild-type multidrug-resistant (MDR) *E. coli.* This showed that environmental conditions could have a major impact on the bactericidal performance of PS-AgNPs; nevertheless, as far as we know, no reports of the effects of cell culture medium on the antibacterial behavior of PS-AgNPs

have been published. Another advantage of light-activable PS-AgNPs is that the light can be modulated on intensity, time, or irradiation cycles to maximize the generation of ROS and, as a direct consequence, the Ag^+ release efficiency. For example, one study employed dual-step irradiations to effectively generate ROS to kill cancer cells [186]. Another study demonstrated that the continuous 30-minute laser irradiation of PS-AgNPs (Ce6-AgNP) results in a gradual Ag^+ release. The authors showed that light can be modulated to control the Ag+ release with short laser pulses in an ON (5 min) and OFF (5- 10 min) pattern. The release of Ag^+ increased only during ON stage, whereas the amount of Ag^+ reached saturation during OFF. This pattern repeats in the subsequent irradiation cycles [93]. However, in this study, the therapeutic outcome of this ON/OFF approach was not evaluated. Thus, modulating the number of light irradiation cycles of PS-AgNPs can be a promising strategy to control the release of Ag^+ and maximize the bactericidal effect.

Herein, we used protoporphyrin IX (PpIX) as a PS that absorbs in the visible spectra (400-700 nm) to synthesize PpIX-AgNPs. In this study, we assessed the role of culture media and light irradiation conditions affecting the antibacterial activity of PpIX-AgNPs **(Figure 3.1)**. First, we elucidate the critical role of the environmental conditions on the colloidal stability of PpIX-AgNPs by assessing the hydrodynamic size, UV-Vis spectrum, and zeta potential in different bacterial cell culture media, including Dulbecco Phosphate buffer saline (DPBS), Nutrient Broth (NB), Tryptic Soy Broth (TSB), and Luria- Broth (LB). We hypothesized that exposing PpIX-AgNP in a multi-step irradiation setup (MIS) (Figure S1) could maximize the Ag^+ release and promote effective antibacterial action at lower concentrations. The dual-step irradiation setup for PpIX-AgNPs in DPBS increased the Ag^+ release, even at lower concentrations. Next, we determined the impact of the culture media on the light-activated Ag^+ release kinetics under single and dual-step light irradiation setup. The protein and salt content affect colloidal stability and Ag^+ release kinetics

under variable culture media. The PpIX-AgNP was most stable in NB media, whereas Ag^+ release kinetics was highest in DPBS. Finally, we tested the antibacterial action of PpIX-AgNPs in DPBS and NB under the dual-step irradiation strategy in *Methicillin-resistant Staphylococcus aureus (MRSA)*. In DPBS, the dual-step irradiation resulted in a 6-log and 5-log reduction in the MRSA population at PpIX-AgNP concentrations that were 33% (1 µg/mL) and 67% (0.5 µg/mL) lower than the original concentration, i.e., 1.5 µg/mL. However, the antibacterial actions in NB were attenuated and required a higher PpIX concentration (5.0 µg/mL) and dual-step irradiation strategy at reduced bacterial load to achieve ~ 5-log reduction in MRSA population.

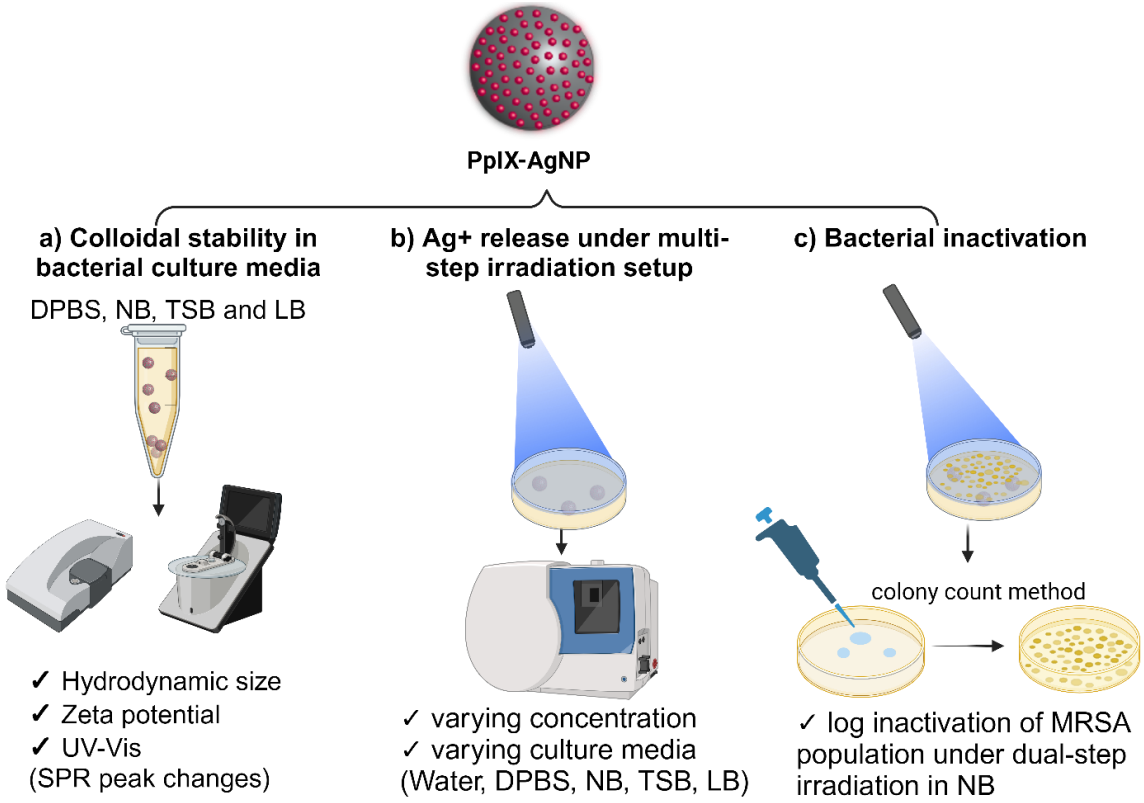

Figure 3.1 Schematic summarizing the objectives of Chapter 3. a) Examine the colloidal stability of PpIX-AgNP in bacterial culture media; b) Generate the Ag^+ release under multi-step irradiation

setup in various bacterial culture media; c) Evaluate the bacterial log inactivation in MRSA under multi-step irradiation condition in NB.

3.2 Experimental Section:

3.2.1 Materials:

The following chemicals were purchased from the respective suppliers and used without modifications. Hydrochloric acid (Macron chemicals), nitric acid (Macron chemicals), protoporphyrin IX (Enzo Lifesciences), 1-Ethyl-3-(3-dimethylaminopropyl) carbodiimide hydrochloride (EDC) (Oakwood Chemicals), tannic acid (95%, Acros Organics), dimethyl sulfoxide, dimethylformamide (VWR), dichloromethane (Alfa Aesar). Silver nitrate ($AgNO_3$), silver standard for ICP, cysteamine hydrochloride, N-hydroxysuccinimide (NHS), dimethylamino pyridine (DMAP), N, N Diisopropylethylamine (DIPEA), trisodium citrate dihydrate were purchased from Sigma Aldrich.

The following bacterial broths were obtained from the respective suppliers: 1X Dulbecco's phosphate buffer saline (DPBS) (Corning), Luria Bertani (LB) broth (VWR), Nutrient broth (NB) (Sigma-Aldrich) and Tryptic soy broth (TSB) (BD Biosciences). All the broth cultures were autoclaved before use and stored at 4 ºC.

3.2.2 Synthesis and characterization of AgNP and PpIX-AgNP

All the glassware used for the AgNP synthesis was cleaned with aqua regia before their use. As reported previously, the protoporphyrin-conjugated silver nanoparticles (PpIX-AgNP) were synthesized in a two-step process [94]. In the first step, silver nanoparticles (AgNP) were synthesized using the co-reduction method using sodium citrate and tannic acid.[135] Briefly, a 100 mL aqueous solution of 5 mM trisodium citrate and 0.25 mM of tannic acid was brought to a boil

at 100 °C under vigorous stirring. As the solution started boiling (condenser used to prevent water loss), 1 mL of aqueous solution of 25 mM silver nitrate was added to the solution in one shot and removed from heat when an immediate color change from colorless to yellow was observed. The solution was cooled at room temperature and the AgNPs were centrifuged at 12000 rpm for 15 min to remove excess tannic acid These were further washed with nanopure water three times under the same centrifugation conditions. As synthesized AgNPs are stored in nanopure water.

In the second step, a thiol-functionalized protoporphyrin derivative (cysPpIX) was synthesized using the previously reported protocol.[94, 141] The PpIX-AgNPs were obtained by reacting AgNPs with previously synthesized cysPpIX (1: 0.5 mass ratio) in dimethylformamide (DMF). Briefly, a solution of cysPpIX in DMF (1 mg/mL) was prepared. AgNPs (1 mg) were centrifuged down at 12000 rpm for 15 min to remove the water. Following this, 1 mL of DMF was added and sonication was used to disperse the AgNPs. This solution was transferred to a 20 mL scintillation glass vial and 500 µL of previously prepared cysPpIX solution in DMF was added. An additional 3.5 mL of DMF was added and the reaction mixture was vigorously stirred for 48 h at room temperature. After the reaction, the unreacted cysPpIX was collected via centrifugation at 12000 rpm for 15 min. Nanoparticles were washed three times with DMF and separated under the same centrifugation conditions. The supernatant collected was analyzed using a UV-Vis spectrophotometer to determine the amount of PpIX conjugated on the AgNPs surface. A calibration curve for absorbance at 500 nm and cysPpIX amount (mg) was generated. A typical batch fabricated under the above-mentioned conditions produced 1.2 ± 0.1 mg of PpIX-AgNPs. The synthesized PpIX-AgNPs were stored in DMF under dark conditions.

3.2.3 Ag^+ release kinetics under multi-step irradiation setup (MIS)

The experimental setup was adapted from the previous reports [94]. The release kinetics of Ag^+ were assessed in two experimental irradiation setups: a) Single irradiation mode b) Multi-step irradiation mode (MIS), where the irradiation doses were varied in a step manner. For single irradiation setup, stock solutions of PpIX-AgNP in DMF equivalent to 150 µg/mL AgNP concentration were prepared. The stock solution was diluted 100 times with the relevant media (DPBS, NB, TSB, LB) to obtain a final volume of 4 mL (final concentration = 1.5 µg/mL). A Petri dish (60 x 15 mm) containing 4 mL of diluted solution (conc = 1.5 µg/mL) in relevant media was irradiated with a white light source (400-700 nm; 65 mW/cm^2) for 20 mins. Before irradiation, 100 µL sample was withdrawn indicating the time point as 0 min. Then, 100 µL was collected at specific time points from each sample at 5, 10, 20, 30 min, 1, 2, 4, 6, 12, 24 h. The collected samples were immediately centrifuged for 10 min at 12000 rpm and the supernatant was collected for ICP-OES analysis.

In MIS, two sets of studies were conducted, i.e. release profiles in varying culture media (final conc = 1.5 µg/mL) and release profiles for varying concentrations in DPBS. For these experiments, PpIX-AgNP stock in DMF corresponding to respective AgNP concentrations i.e. 50, 100, 150 µg/mL were prepared. Like in the single irradiation setup, the PpIX-AgNP stock was diluted 100 times in relevant media to obtain a final concentration of 0.5, 1, and 1.5 µg/mL and transferred to the petri dish. The experimental setup used MIS and dual-step irradiation strategy is illustrated in **Scheme S1**. The samples are then irradiated with the white light source for 20 min, followed by 40 mins of incubation at room temperature in dark conditions. This sequence (1 hour duration = 20 mins irradiation + 40 mins resting period) was termed as one irradiation step/cycle (**Scheme S1**). At the end of the 40-minute incubation, the sample was irradiated again following

the same sequence, constituting the 2nd irradiation step. Before irradiation, a 100 µL sample was withdrawn indicating the time point as 0 min. During each irradiation step, 100 µL of the aliquots were collected at time points, 10, 20, 30, 45, and 60 mins. The collected samples were immediately centrifuged for 10 min at 12000 rpm and the supernatant was collected for ICP-OES analysis.

To determine the total amount of Ag^+ in all samples, aliquots of the nanoparticles were digested by performing a "cold digestion" followed by "hot digestion". [136] The digestion protocol was optimized and modified in terms of time and volume. Cold digestion included mixing 50 µg of NPs with 3.0 mL of concentrated HNO3 and incubating at room temperature for 30 min. Later, this mixture was heated under 150 °C using an oil bath for 4-6 h to allow excess HNO_3 to evaporate (hot digestion). The remaining volume was measured using a graduated cylinder and diluted using 2% HNO3. The samples were filtered through a 0.22 µm polyether sulfone (PES) membrane before ICP-OES analysis. A calibration curve was obtained using an Ag silver standard diluted in 2% HNO3 to prepare standard concentrations of 10, 25, 50, and 100 µg/L. A new set of calibration curves were generated for each run. The total amount of Ag+ digested (in µg) was calculated using the calibration curve and expressed in terms of Ag^+ amount per µg of NP (%). The concentration of PpIX-AgNPs (1.5, 1.0, 0.5 µg/mL) used for release were digested using the protocol and the digestion results were expressed in ug/L (Table S5). These values were to calculate % of Ag release using the following equation,

$$\%\ Ag + release = \frac{Ag+released\ at\ time\ point\ 't'\ (\frac{\mu g}{L})}{Total\ Ag+digested\ (\frac{\mu g}{L})} \quad \text{..... Eqn 3.1}$$

The kinetic release rates were determined by performing linear fit on the Ag+ release kinetic plots using OriginPro 2024 (Student version). The R^2 and slope values corresponding to burst and slow release were recorded.

3.2.4 Characterization or Instrumentation:

Hydrodynamic size, polydispersity index (PdI) and zeta potential (ζ-potential) determination were performed using Malvern ZS series. The concentration used for DLS and ζ-potential measurements were fixed at 50 µg/mL. UV-Vis spectra were obtained using Cary 50 UV-Visible spectrophotometer (Varian). 3 mL of sample was used to obtain absorbance spectra from 200-800 nm. The corresponding culture media without nanoparticles were used as blanks and used to normalize the UV-Vis spectra of PpIX-AgNPs in the respective culture medium. The protein content on PpIX-AgNP surface, post-incubation (24 hour) in each bacterial culture media was evaluated using Micro BCA™ Protein Assay Kit (Thermo Scientific). Equal concentration of PpIX-AgNPs were suspended in the respective culture media and were centrifuged for 10 mins at 12000 rpm for 24-hour incubation at 4 ºC. The supernatant was discarded and the PpIX-AgNP (pellet) was resuspended in autoclaved. The NPs were washed two more times with autoclaved water. The washed PpX-AgNP were resuspended in water via sonication and diluted 100-fold for the BCA assay. The protein content was evaluated based on the absorbance recorded at 620 nm.

The Ag^{+} release was quantified using inductively coupled plasma - optical emission spectroscopy (ICP-OES) (Optima 3000, Agilent). Samples obtained from post digestion and release experiments were introduced into plasma via a peristaltic pump and discharged as an aerosol suspended in argon gas. The data acquisition was performed in triplicates with the torch assembly in the axial mode. The default acquisition parameters used are RF = 1.2 kW; auxiliary gas flow = 1 L/min, nebulizer gas flow = 0.7 L/min; plasma flow = 12 L/min, pump speed = 12 rpm; stabilization time = 15 s; sample uptake time = 25 s; Rinse time = 30 s and Ag analytical line = 328.068 nm.

The size and morphology of the synthesized nanoparticles were analyzed using transmission electron microscopy (TEM, JEM 1230) operating at an accelerating voltage of 200 kV. The samples were prepared by dispersing AgNPs and PpIX-AgNPs in 50 µL of ethanol. Then, 10 µL of the sample was placed on the carbon-coated copper grid and air-dried for 1-2 h. The nanoparticle size and its distribution were calculated using ImageJ software. A sample size of 150 nanoparticles was considered for analysis, and the size was finally reported as average ± sd.

3.2.5 Bacterial Inactivation Experiment:

Preparation of Bacterial Strain:

Methicillin resistant *Staphylococcus aureus* (MRSA) strain BAA-44, purchased from ATCC was used as the test organism. LB agar plates were used to subculture the MRSA strain. A single colony from the LB agar plate was inoculated in LB broth and incubated at 37^{o}C for ~18 h, resulting in actively growing cells. The fresh cultures were centrifuged at 7000 rpm for 5 minutes the following day and the collected cells were washed twice with 1xDPBS to remove any residual particles of the broth. The washed cells were then resuspended in relevant media (1xDPBS and NB) to achieve 0.5 McFarland standard, which corresponds to ~1.5 x 10^8 CFU/mL. For NB experiments, the O.D lower than 0.5 McFarland standard was considered, to achieve reduced initial bacterial load (~ 10^7 CFU/mL).

Irradiation of Bacterial Cells:

Before exposure to light, bacterial suspension was incubated in the dark at room temperature for 30 minutes with varying concentrations of AgNPs and PpIX-AgNPs. To achieve the working concentrations 1.5 µg/mL, 1 µg/mL, and 0.5 µg/mL from a stock of 150 µg/mL AgNPs and PpIX-AgNPs, the bacterial and nanoparticles were prepared by mixing 3960 µl of bacterial

suspension (DPBS or NB) with 40 µl of stock sample, 3973 µl of bacterial suspension with 27 µl of stock sample, and 3986 µl of bacterial suspension with 14 µl of stock sample respectively. The suspensions were exposed to the white light source for 20 minutes for the single irradiation experiment. For the multiple irradiation experiment, the cells were exposed to the light source for 20 minutes, followed by 40 minutes of incubation in the dark at room temperature, and then subjected to second irradiation for another 20 minutes. All the experimental sets were conducted in triplicates with negative and dark controls.

Enumeration of Surviving Bacterial Cells:

The survival of the bacterial cells was determined at 3 different time points- immediately after irradiation (0 h), 4 h and 24 h post irradiation in duplicate using the drop plate method where 100 µL of samples from all experimental sets were diluted in 900 µL of respective diluent. Subsequently, 20 µL of each dilution was spotted on the LB agar plate. The log inactivation was calculated using equation 1, which relates bacterial cells' initial and final concentrations.

$$\text{Log inactivation of bacteria} = \log\left(C_o/C_t\right) \qquad \ldots\ldots \text{ (Equation 3.2)}$$

Here, C_o = concentration (CFU/mL) of bacteria without the addition of nanoparticles, and C_t = bacterial concentration after the addition of nanoparticles and (or) light irradiation after time t.

3.2.6 Statistical Analysis

Graphs and statistical analyses were performed using OriginPro 2024 (Academic Version). Statistical significance between each irradiation strategy was assessed by one-way analysis of variance (ANOVA), with the Tukey test performed for mean comparison (for comparing PpIX-AgNP antibacterial log inactivation results in NB for varying bacterial load). All the statistical analyses were performed using OriginPro 2024 (Academic Version) with $\alpha = 0.05$ and reported as

star assigned to the p-values. The exact p values are mentioned in the main paper of the respective experiment.

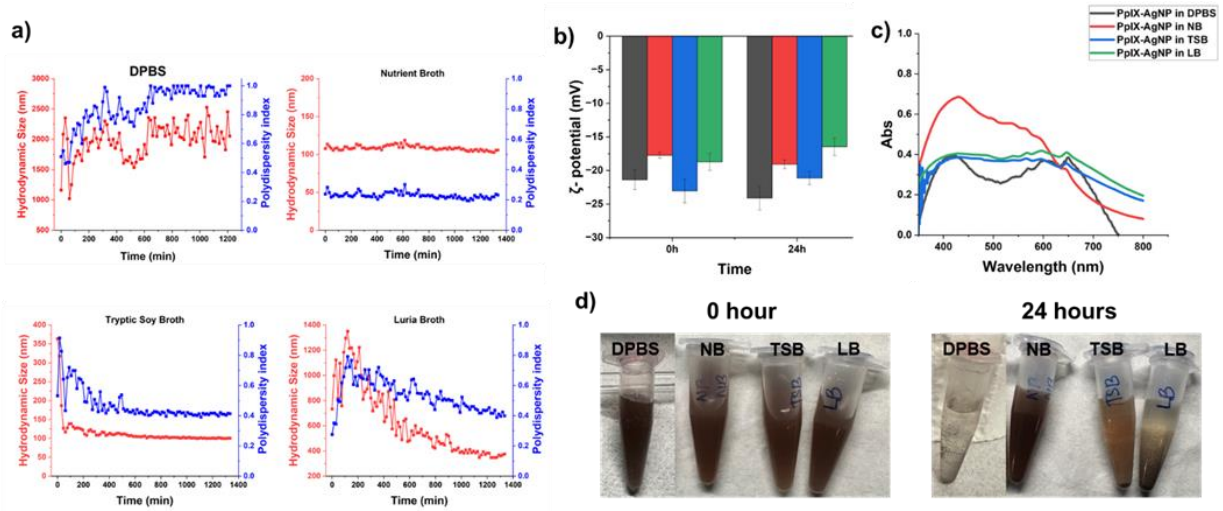

Figure 3.2 Colloidal stability of PpIX-AgNP in DPBS and bacterial culture media, nutrient broth (NB), tryptic soy broth (TSB), and Luria Bertani broth (LB). a) Hydrodynamic size (red) and polydispersity (blue) change over 24 hours for PpIX-AgNPs in DPBS, NB, TSB, and LB (bacterial culture media). b) Effect of bacterial culture media on ζ-potential values. c) UV-Vis spectrum for PpIX-AgNPs in bacterial culture media. d) Visual images of PpIX-AgNP in bacterial culture media at 0 hour and 24 hours.

3.3 Results and Discussion:

3.3.1 Synthesis and characterization of PpIX-AgNPs

Silver nanoparticles (AgNPs) were reacted with cysteamine-modified PpIX (cysPpIX) in DMF based on our previously published work [94]. AgNPs were synthesized based on the co-reduction of silver nitrate ($AgNO_3$) using sodium citrate and tannic acid [135]. The cysPpIX derivative was synthesized in a two-step approach; first, the carboxylic groups were activated using NHS, affording an ester group to obtain succinimide ester PpIX (sePpIX). As a second step,

a nucleophilic acyl substitution was carried out with cysteamine to obtain the final cysPpIX [141]. The successful synthesis of sePpIX and cysPpIX derivatives was confirmed using UV-Vis, FT-IR, and MALDI (Figure S1).

The cysPpIX obtained was further reacted with AgNPs in DMF in the ratio of 0.5:1.0 wt.(cysPpIX:AgNP) to obtain the final PpIX-AgNPs. The final product was characterized by UV-vis spectroscopy to determine the PpIX content, ζ-potential, and dynamic light scattering (DLS). The UV-Vis of AgNPs is generally characterized by an absorption peak around 420-425 nm, associated with the surface plasmon resonance (SPR) peak of silver nanoparticles. As seen in Figure S2, PpIX-AgNP shows a strong absorption band in the 425- 435 nm range related to the Soret- band (S-band) of PpIX and the SPR peak of AgNP. However, unlike AgNPs, PpIX-AgNP also shows absorption in 500- 700 nm regions that are exclusively associated with the Q-band of PpIX (Figure S2), which confirms the successful conjugation of PpIX. Post-reaction, the supernatants 1, 2, 3, and 4 were collected after each PpIX-AgNP wash, and the absorbance at 500 nm was evaluated (Figure S3). The difference in the control and supernatants clearly indicates the successful loading of PpIX on the AgNP surface. The % loading of PpIX on AgNPs was quantified using the calibration curve (Figure S3, inlet) and determined to be 44.8 ± 0.3 wt. % (n=6). Furthermore, TEM images indicated that AgNPs and PpIX-AgNPs have spherical morphology (n= 150) with almost identical diameters of 42.2 ± 7.8 and 42.2 ± 8.9 nm, respectively (Figure S2). As indicated in Table S1, the hydrodynamic size measured by DLS indicated a slight increase from 37.8 ± 0.3 nm (AgNP) to 64.1 ± 0.6 nm (PpIX-AgNP) in DPBS (1 mM), which is due to aggregation of nanoparticles as an indication of the presence of PpIX on the surface of AgNPs. The ζ-potential also showed a slight increase in negative charge from -47.1 ± 3.6 (AgNP) to -56.7 ± 3.0 (PpIX-AgNP).

3.3.2 Colloidal stability of PpIX-AgNP is varying bacterial culture conditions

The colloidal stability of the PpIX-AgNPs was studied in different cell culture media, including DPBS (10 mM), NB, TSB, and LB. The following properties were determined as indicators of colloidal stability: hydrodynamic diameter (D_h), polydispersity index (PdI), ζ-potential, and UV-Vis spectroscopy.

The D_h and ζ-potential of PpIX-AgNPs were monitored at 50 μg/mL concentrations. The changes in D_h of the PpIX-AgNP were evaluated from 0-24 hours in the respective culture media (**Figure 3.2a**). The D_h size at t=0 hour was observed to be lowest in NB (107.8 ± 0.5 nm), followed by TSB (385.2 ± 3.4 nm), LB (772.5 ± 29.7 nm) and finally DPBS (816.1 ± 76.3 nm). PpIX-AgNPs in NB show excellent colloidal stability throughout the 24 h, with D_h varying in the 100-120 nm range and PdI remaining consistent at 0.2. A similar trend was observed in water wherein D_h remains consistent throughout the 24-hour duration at around ~100 nm, indicating good colloidal stability, supported by a PdI = 0.2 (Figure S4). However, in the case of DPBS, TSB, and LB, the Dh shows a significantly higher value at t= 0 hour, which eventually drops from ~370 nm to ~150 nm in TSB and ~1350 nm to ~350 nm. It should be noted that the drop in D_h is abrupt or faster in TSB (within 60 mins), whereas in LB, it is a gradual drop that happens over 16-17 hours. In the case of DPBS, the PpIX-AgNP indicates poor colloidal stability, as demonstrated by the constant fluctuation in Dh (1000- 2000 nm) and the PdI value reaching as high as 1.0. As seen in **Figure 3.2d**, PpIX-AgNP in all media except NB shows visible precipitation after 24 hours of incubation. The changes in the net surface charge of nanoparticles are usually a great indicator of their colloidal stability since the electrophoretic mobility of nanoparticles in a solution is driven by surface charge [187]. As seen in **Figure 3.2b** and Table S2, at t=0 h, the ζ-potential value decreases from -38.4 ± 0.8 mV (1 mM DPBS) to -21.4 ± 1.5 mV (10 mM DPBS) with the reduction in ionic strength of DPBS.

This can be attributed to Debye length, which is inversely related to the higher ionic strength [187, 188]. The ζ- potential value in other media was reportedly similar to DPBS (10 mM), i.e., -17.8 ± 0.4 mV in NB, -23.1 ± 1.8 mV in TSB, and -18.7 ± 1.3 mV in LB. Post 24-hour incubation, there are only minor changes in ζ-potential in DPBS (3-5 mV), while the culture media show only a minuscule difference of 1-2 mV. It is also well-established that the protein corona reduces the surface charge [189].

UV-Vis spectroscopy is also a good indicator of colloidal stability for metal nanoparticles such as gold and silver NPs because the shift in SPR peak is associated with AgNPs surface coating, surrounding environment, and NP plasmonic coupling [190-192]. Redshift is related to a shift in the SPR peak at longer wavelengths, whereas blueshift is associated with a shift in the peak to shorter wavelengths. Blueshift is linked to a decrease in the NP size [193], and redshift corresponds to changes in NP surface coating or aggregation [191, 194]. We measured the UV-Vis spectrum for PpIX-AgNPs in different conditions: Water, DPBS (10 mM), NB, TSB, and LB. As seen in **Figure 3.2c** and Figure S4, the UV-Vis spectra in water and DPBS indicate that peak wavelength is observed at 420 nm; however, this peak wavelength undergoes red-shift in all the media conditions, i.e., NB, TSB, and LB with location at 429 nm (NB), 432 nm (TSB), and 433 nm (LB), respectively. A distinct red shift is observed compared to DPBS and water, which can be associated with the interaction of protein content in media with the surface of AgNPs.

To thoroughly analyze the influence of bacterial culture medium on the colloidal stability of PpIX-AgNPs, it is essential to analyze the composition of each media formulation to account for protein and salt content (w/v %; Table S3). The percentage of salt content and protein (w/v %, respectively) for DPBS and each bacterial culture media are listed in Table S4. Based on time-resolved hydrodynamic size analysis (**Figure 3.2d**), PpIX-AgNP remains the most stable in NB,

while the colloidal stability deteriorates in DPBS, TSB, and LB. These trends in colloidal stability, i.e., NB> TSB> LB > DPBS, could be attributed to the reducing salt content in LB (1%), DPBS (0.95%), TSB (0.8%), and NB (0.6%). The high salt content drives this colloidal stability, correlated to the precipitation observed in LB and TSB (**Figure 3.2d**). Furthermore, DPBS and LB display variable stability despite containing similar salt content. This can be attributed to the high protein content in LB (1.5%) that may render some colloidal stability to the NPs despite high salt content (1%). It should be noted that NB has the intermediate protein content (1.8%) and lowest salt content (0.6%), which contributes to its superior colloidal stability. NPs undergo precipitation/ aggregation more in DPBS, LB, and TSB than in NB, which can be attributed to salt content. Overall, salt content plays a dominant role in driving colloidal stability. These findings partially support the previous studies expanding on the role of bacterial culture media on AgNP colloidal stability [162].

Based on the UV-Vis results, all NPs showed redshift, which can be attributed to the higher protein content in all culture media. Higher protein content may also lead to the formation of protein corona on the AgNP surface, which can promote precipitation. As seen in Table S4, the trends based on protein content are TSB (2%) > NB (1.8%) > LB (1.5%) > DPBS (0%). This was confirmed using a colorimetric BCA assay, which followed a similar trend to Table S4. The protein content of PpIX-AgNP in varying media was evaluated using BCA assay (monitored at 620 nm). PpIX-AgNPs were dispersed in media for 24 hours and further washed 3 times via centrifugation, and BCA assay was performed on these respective NPs. As seen in Figure S5, PpIX-AgNPs in TSB show the highest protein content, followed by LB, then NB. This indicates that significant changes in colloidal stability in TSB can be attributed to higher protein content. In contrast, the

changes in LB can be attributed to protein content and salt content. These results prove that NB is the most promising media regarding colloidal stability among the tested bacterial culture media.

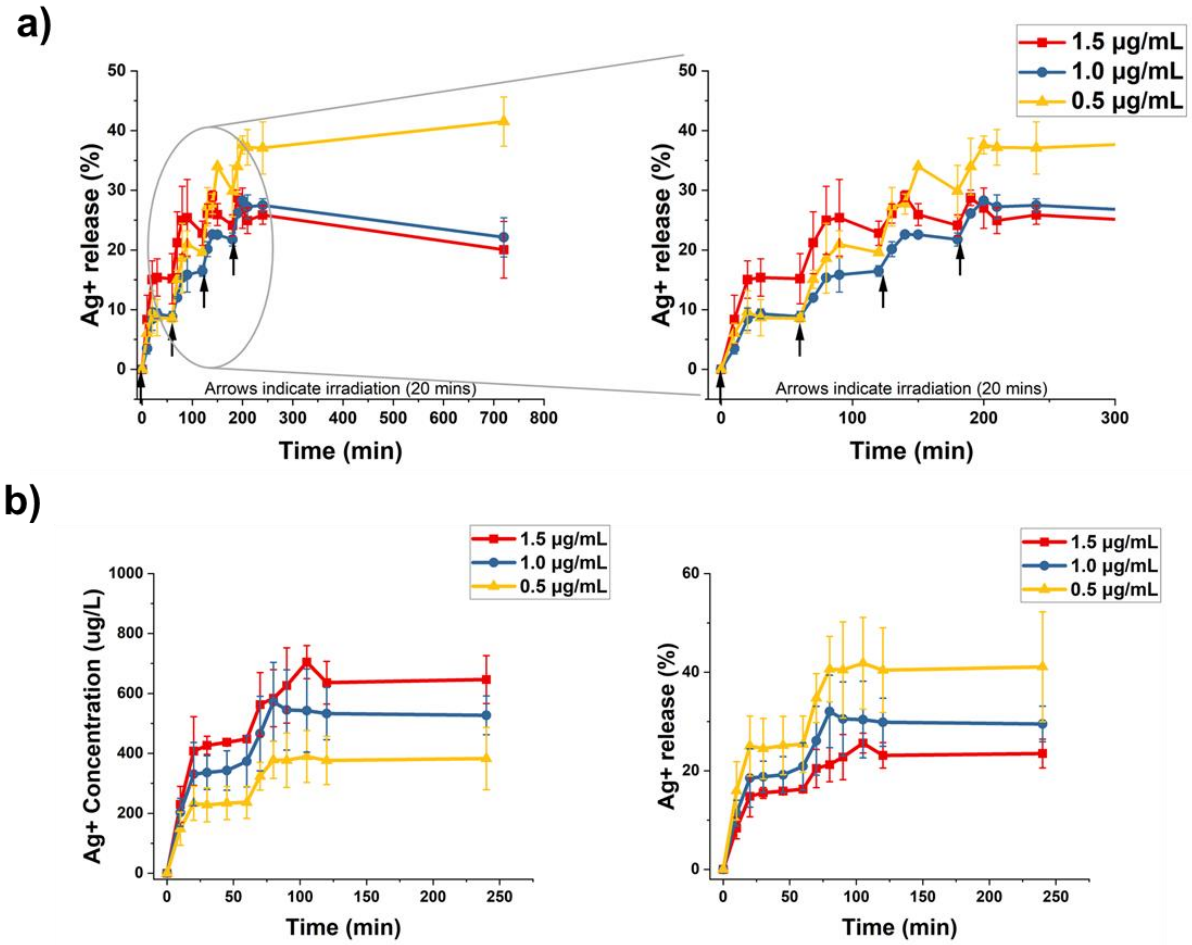

Figure 3.3 Ag^{+} release kinetics for varying concentrations of PpIX-AgNP tested in a) multi-step irradiation (MIS) and b) dual-step irradiation strategy- cumulative Ag+ concentration and Ag+ release efficiency (%). The arrows indicate the start of a MIS irradiation

The protein content of PpIX-AgNP in varying media was qualitatively assessed using BCA assay (monitored at 620 nm). PpIX-AgNPs were dispersed in media for 24 hours and further washed 3 times via centrifugation, and BCA assay was performed on these respective NPs. As seen in Figure S3, PpIX-AgNPs in TSB show a comparatively higher protein content, followed by LB,

then NB. This indicates that major changes in colloidal stability in TSB can be attributed to higher protein content. In contrast, the changes in LB can be attributed to protein content and NaCl content. Among the tested bacterial culture media, NB is the most promising media in terms of colloidal stability.

3.3.3 Investigation of Ag^+ release profile under multi-step irradiation setup (MIS)

The PS attached to AgNPs under light irradiation is known to enhance the generation of Ag^+ by oxidizing the AgNPs' surface [77, 99]. Our group previously demonstrated that the light-activated Ag^+ release kinetics after single irradiation are composed of a burst and steady phase [94]. The burst phase was associated with the irradiation time, followed by a steady phase representing the long-term passive release of Ag^+. Our study showed that the media used for the release has a significant impact; for example, the ionic composition of DPBS drastically favors Ag^+ release compared with nanopure water. In this work, we hypothesized that the release of Ag^+ can be further enhanced by applying multiple irradiation cycles.

Each irradiation cycle (1 hour) for the MIS setup is composed of 20-minute irradiation with white light (400 -700 nm, 19 mW/cm^2), followed by 40 minutes of a resting period in the absence of light at room temperature (**Scheme S1**). We tested the MIS experiment setup for PpIX-AgNP at different concentrations (1.5, 1.0, and 0.5 μg/mL) in DPBS using 4 irradiation cycles. The amount of Ag^+ released was measured by ICP-OES at different time intervals. During each cycle, aliquots were collected at time points: 0, 10, 20, 30, 45, and 60 min. The beginning of each cycle is indicated by an arrow in **Figure 3.3a**. A final aliquot was collected 12 hours after the first cycle. In general, the Ag^+ release profiles resemble a step function with the increase in Ag^+ release corresponding to the irradiation window (burst release = 20 mins) and indicating no release after around 30 min (steady phase) (**Figures 3.3a** and S6). This behavior was observed for all the concentrations. It is

also important to note that at 1.5 µg/mL concentration, ~700 µg/L of the cumulative Ag^+ release was achieved within the first two irradiation cycles (Figure S6). After two cycles, the Ag^+ release remains saturated for the same concentration, implying that the 3rd and 4th irradiation cycle provides minimal improvement in Ag^+ release. Hence, dual-step irradiation (2 irradiation cycles) suffices to achieve a higher cumulative Ag^+ release and can easily be implemented in bacterial inactivation experiments.

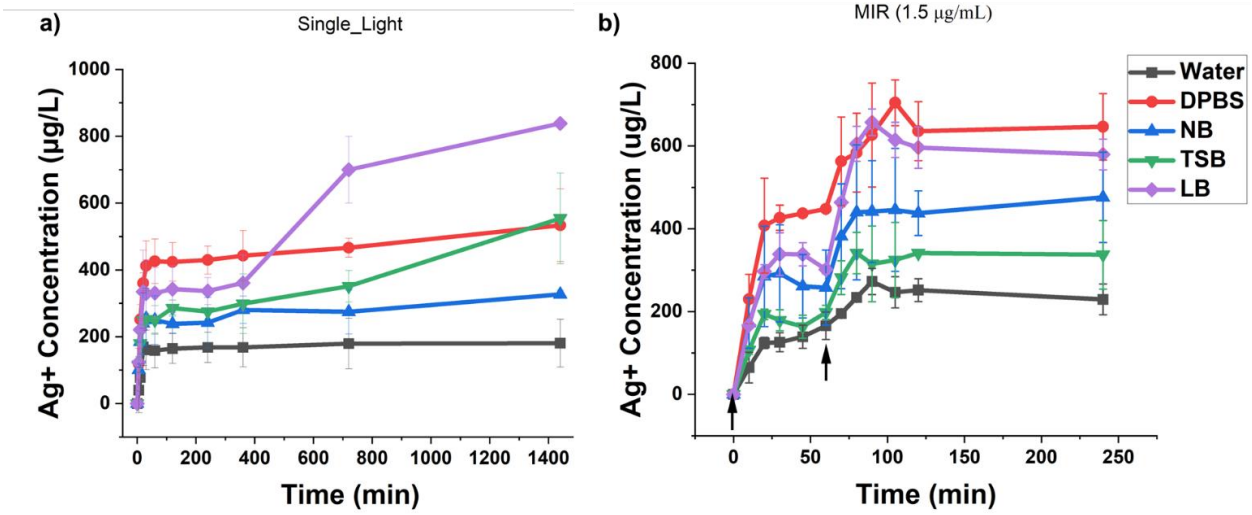

Figure 3.4 Ag^+ release kinetic for PpIX-AgNP (1.5 µg/mL) in bacterial culture media under a) single irradiation setup and b) dual-step irradiation setup. The arrows indicate the start of a MIS irradiation cycle (Irradiation time = 20 min).

The dual-step irradiation strategy was recorded for 4 hours and included two cycles of irradiation (**Figure 3.3b**). The maximum cumulative release of Ag^+ at the end of the experiment follows the expected concentration-dependent trend with 1.5 > 1.0 > 0.5 µg/mL. However, like the MIS experiments, the 0.5 µg/mL showed the maximum percentage of Ag^+ released to be ~40 %, followed by 1.0 µg/mL (~30 %) and 1.5 µg/mL (~25 %). The percent of Ag+ release for each concentration was calculated by recording the total Ag^+ amount (µg/L) post-digestion experiments

using ICP-OES (Table S5). The release rates for the two burst phases (B1 and B2) were calculated using linear curve fitting (Figure S7 and Table S6). The release rate (B1) gradually decreases with decreasing concentration, i.e., 1.5 µg/mL (21.50 µg L^{-1} min^{-1}) > 1.0 µg/mL (18.68 µg L^{-1} min-1) > 0.5 µg/mL (12.31 µg L^{-1} min^{-1}). Interestingly, the release rates in burst phase 2 (B2) are similar for all concentrations (7- 10 µg L^{-1} min^{-1}). Overall, the dual-step irradiation strategy can be applied to accelerate Ag^+ release in a controlled fashion. Moreover, we anticipate that this approach will maximize the release of Ag^+ in conditions with lower dosages of PpIX-AgNPs.

3.3.4 Investigation of Ag^+ release profile in varying bacterial culture media

Culture composition plays a vital role in Ag^+ release. Previous studies have reported that media composition influences Ag^+ release [68, 162, 163]. As far as we know, no study has reported the effect of media composition on Ag^+ release kinetics, especially for light-activated nanoparticles. In this study, we investigate the impact of different culture media, including NB, TSB, and LB, on the release of Ag^+ after a single and dual-step light irradiation. DPBS and water were considered as controls, as reported previously [94]. The study was tested for 24 hours using 1.5 µg/mL of PpIX-AgNPs. As seen in **Figure 3.4a**, in a single irradiation mode, a burst and a steady release phase are observed in all media conditions. In the burst phase, the cumulative Ag^+ release shows trends as DPBS> LB> TSB> NB > water. The release rate was calculated using a linear curve fitting, as indicated in Figure S8 and Table S7. The highest release rate was obtained for DPBS (23.66 µg L^{-1} min^{-1}), followed by LB (22.21 µg L^{-1} min^{-1}), NB (17.83 µg L^{-1} min^{-1}), TSB (12.34 µg L^{-1} min^{-1}), and finally water showing slowest release rate (8.26 µg L^{-1} min^{-1}). We have previously demonstrated that the ionic composition in the media drastically favors Ag^+ release; nevertheless,

in these experiments, the other components in the bacterial culture media also affect the Ag^+ release. The higher salt content (Table S4) in DPBS (0.95%) and LB (1%) drive the release, resulting in an Ag^+ concentration of ~361 µg/L and 334 µg/L, respectively, in the first 20 mins of irradiation. The lower release in TSB, NB, and water is due to lower salt content. It is known that protein content also plays a crucial role in Ag^+ release. Unlike the salt content, the higher protein content in TSB and NB may hinder the Ag^+ release. In the case of TSB, higher protein content (2%) results in the lowest release rate (12.34 µg L-1 min-1), resulting in an Ag^+ concentration of 248 µg/L in the burst phase. Our results confirm that NB, which has the intermediate protein (1.8%) and lowest salt content (0.6%), shows the lowest Ag^+ concentration (240 µg/L) among the culture media. Water, lacking salt and protein content, shows the lowest Ag^+ release (170 µg/L). The literature also noted that the presence of NaCl can passivate the AgNP surface, promoting the Ag^+ release, whereas the presence of protein can inhibit the Ag^+ release [68, 183, 195, 196]. Studies have explored the role of culture media in the release of Ag^+ and the antibacterial activity of AgNPs [163, 183].

The impact of the media on the Ag^+ release was slightly different at the end of the release experiment with the following trend: LB> DPBS~ TBS> NB > water. The Ag^+ release was superior in LB media (838 µg/L), followed by TSB (554 µg/L) and DPBS (534 µg/L). Additionally, culture media in TSB and LB showed increased Ag^+ release with kinetic rates of 0.14 µg L^{-1} min^{-1} and 0.39 µg L^{-1} min^{-1}, respectively. Both these media also show a sharp increase in Ag^+ release post-6-hour time point. However, the increased performance in the TSB relative to the burst phase can be attributed to intermediate salt content (0.8%), which drives the increase in Ag^+ concentration (554 µg/L) in the steady phase. DPBS and NB show a passive release rate of Ag^+ at 0.07 and 0.06 µg L^{-1} min^{-1}, with the lowest overall release observed in NB (326 µg/ L), among the culture media.

The higher protein and lower salt content contribute to this behavior. A dark control experiment (Figure S9) shows a minimal Ag+ release for NB and TSB compared to the light-irradiated counterpart. However, an interesting observation is that LB under dark conditions also indicates an increase in Ag^+ release in the steady phase that can be attributed to the higher salt content. This increased interaction of Ag^+ ions with oxygen-, nitrogen-, or sulfur-containing components such as tryptone and glucose may drive more Ag+ ions into the culture media via Le Chatelier's principle [197].

The dual-step irradiation strategy was designed to evaluate the role of culture media on Ag^+ release profiles. In the dual-step irradiation strategy, there are two burst phases, B1 and B2, which correspond to two cycles of irradiation (indicated by the arrow in **Figure 3.4b**). The Ag^+ release profiles were generated for the same concentration of 1.5 µg/ mL in varying culture conditions, which showed that higher release was achieved in dual-step mode within a shorter timespan (4 hours). For example, under a single irradiation setup in water, the max Ag^+ release of 180 µg/L was achieved, whereas in dual-step, the maximum Ag^+ release achieved is 230 µg/L within (4 hours) (Figure S10). These results varied in different media conditions, with maximum cumulative Ag^+ release at 4 hours following the trend, DPBS> LB> NB > TSB> Water (**Figure 3.4b**). Under dual-step, DPBS still shows highest Ag^+ release of ~646 µg/L with release rates of 9.93 µg L^{-1} min^{-1} (B1) and 6.61 µg L^{-1} min^{-1} (B2). For most media conditions, the B1 and B2 release rates were similar (Table S8, Figure S11). The B1 and B2 release rates were significantly varied only in NB, i.e., 12.59 µg L^{-1} min^{-1} and 7.79 µg L^{-1} min^{-1}. Figure S10 shows an apparent increase in Ag^+ concentration in dual-step irradiation strategy than single irradiation setup is demonstrated with trends in maximum Ag+ release as shown, i.e., DPBS> LB> NB> TSB> Water. This points to the advantage of using such a strategy for overcoming limitations related to hindered Ag^+ release due

to protein content, as seen in single irradiation (**Figure 3.4a**). TSB serves as an exception case in terms of the single vs dual-step Ag^{+} release, wherein TSB shows almost minimal release in all

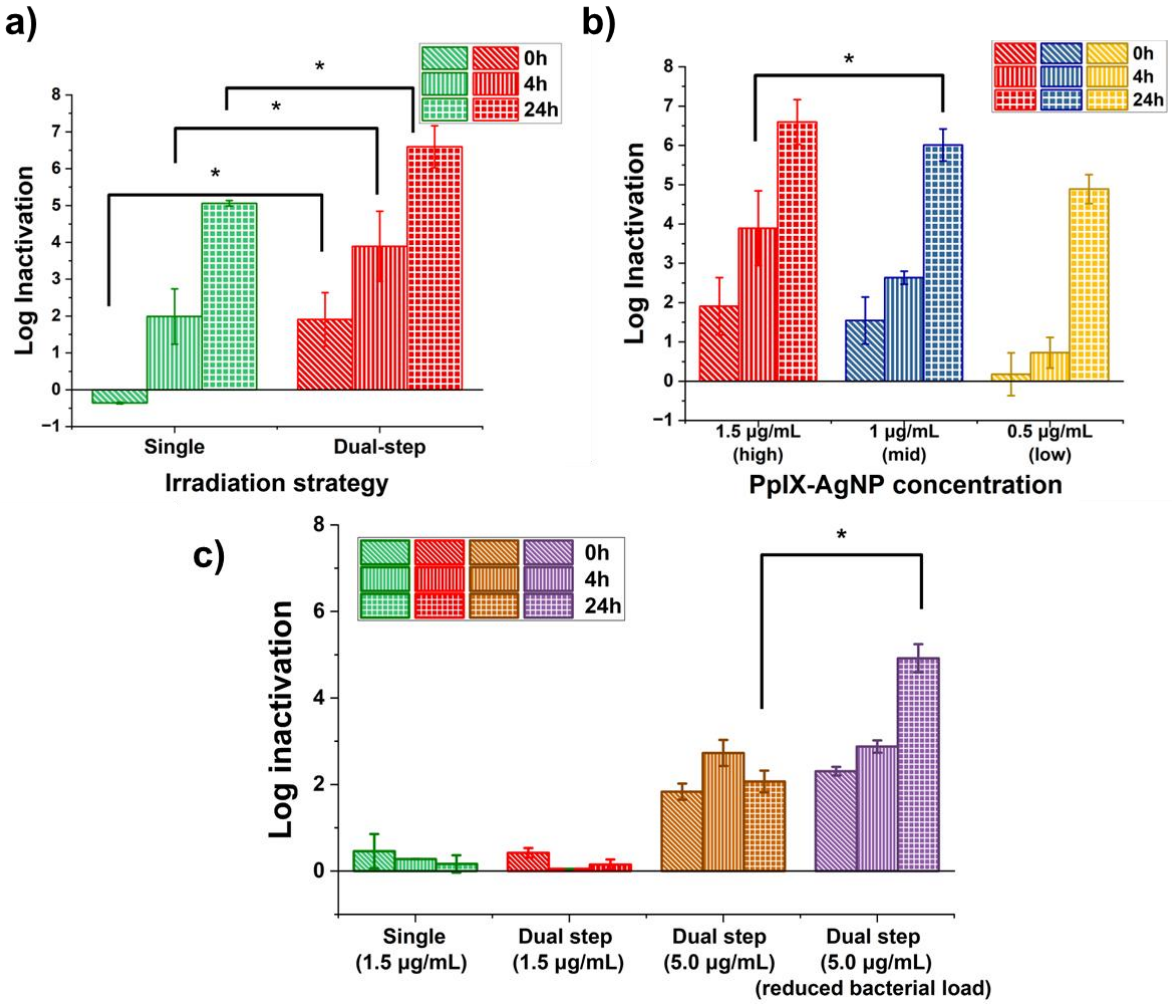

Figure 3.5 Antibacterial activity assessed in MRSA under variable light irradiation and culture conditions. The time point 0 h indicates the inactivation achieved after light irradiation for 20 min. The other two time points; 4 and 24 h show the antibacterial effect post-irradiation. The error bar is the standard deviation of three independent experimental replicates. a) The antibacterial activity of 1.5 µg/mL PpIX-AgNP in DPBS tested in single and dual-step irradiation setup. b) The antibacterial activity of varying concentrations of PpIX-AgNP in DPBS tested in a dual-step irradiation setup. c) The antibacterial activity of varying concentrations of PpIX-AgNP in NB.

burst phases (single or dual-step, i.e., B1 and B2), as seen in Table S8. However, TSB shows increased Ag^+ release in the steady phase (under single irradiation), **Figure 3.4a**. Considering that Ag^+ release was lowest in NB under single irradiation at 4 hours (242 µg/L), including the dual-step irradiation strategy doubles the Ag+ concentration (475 µg/L) within the same period. Thus, the dual-step irradiation strategy improves the Ag^+ release in NB. These results, along with the increased colloidal stability of PpIX-AgNP observed, make NB an excellent culture medium to demonstrate the antibacterial activity of PpIX-AgNP in a dual-step irradiation strategy.

3.3.5 Bacterial inactivation experiment

MRSA is one of the most common causes of ARB infections and is part of the 'nine bacteria of international concern' [3, 5, 25, 125, 164]. The antibacterial properties of PpIX-AgNPs at a concentration of 1.5 µg/mL were tested against MRSA (BAA-44 strain from ATCC) in DPBS under single and dual-step irradiation setup. Each irradiation cycle comprised 20 min irradiation of white light (400 -700 nm, 19 mW/cm^2), followed by 40 min of resting period in the absence of light at room temperature before the next cycle (Scheme S1). The bacterial log inactivation was determined by using the colony count method by collecting samples immediately after 0 h, 4 h, and 24 h post-irradiation [94]. As seen in **Figure 3.5a**, the dual-step irradiation achieved significantly better log reduction in the MRSA population compared to the single irradiation post 0 h, 4 h, and 24 hours of irradiation (p-value < 0.05). At the 24-hour post-irradiation timepoint, incorporating a dual-step irradiation setup increased the log inactivation of MRSA by ~1.53 logs from 5.0 to 6.6 log reduction as compared with single irradiation, which corresponds to about 30 times higher MRSA reduction ($p = 0.04$). The improved advantage of the dual-step irradiation strategy was more pronounced at 4 and 0 hours with ~ 2 log increase in reduction of MRSA population than single irradiation. The dual-step shows a 1.9 log reduction at 0 hours post-irradiation, indicating its

benefit of demonstrating antibacterial activity in a shorter period. We also performed control experiments using equivalent amounts of AgNPs (1.5 µg/mL) and cysPpIX (1 µM) concentrations corresponding to 1.5 µg/mL of PpIX-AgNP. Figure S12 shows that both AgNPs and PpIX-AgNPs achieved <1 log inactivation at 1.5 µg/mL concentration under dark conditions regardless of the incubation period. AgNPs achieved 2.17 log inactivation after 24 hours post-irradiation, which is negligible compared to the inactivation achieved by PpIX-AgNPs as described above. The control experiments with cysPpIX showed that 2.98 log inactivation was achieved immediately after 20 minutes of exposure, followed by 3.14 and 3.26 log inactivation after 4 h and 24 h, respectively (Figure S12). Unlike AgNPs, cysPpIX instantaneously exerts bacterial inactivation via the generation of ROS, i.e., photodynamic inactivation of MRSA.

To evaluate the relevance of the release of Ag^+ generated during dual-step irradiation, bacterial inactivation experiments were carried out in DPBS at different concentrations of PpIX-AgNPs, including 1.5 (high), 1.0 (mid), and 0.5 (low) µg/mL. We hypothesized that the dual-step irradiation setup would maximize the Ag^+ release efficiency to achieve improved antibacterial efficiency at 1.0 and 0.5 µg/mL concentrations of PpIX-AgNPs. In dark conditions, the dual-step irradiation setup at all concentrations shows minimal antibacterial activity at all post-irradiation incubation times (Figure S13). As seen in **Figure 3.5b**, after dual-step irradiation, a concentration-dependent trend in log reduction within 4 and 24 h post-irradiation time was observed with 1.5 > 1.0 > 0.5 µg/mL. The maximum log reduction in the MRSA population achieved at 24 h for the different concentrations was 6.59 log, 6.11 log, and 4.88 log. Interestingly, no significant difference between log reduction achieved at 1.5 and 1.0 µg/mL was observed, indicating that a lower concentration can effectively eliminate MRSA. Therefore, our findings demonstrate that introducing a dual-step irradiation strategy can reduce the number of PpIX-AgNPs by at least

33.3% (1.0 µg/mL) to achieve similar antibacterial efficacy as single irradiation. By lowering the PpIX-AgNP concentration by 67% (0.5 µg/mL), a maximum 4.8-log reduction in the MRSA population can be achieved. The effective light modulation of this system can have a major effect on decreasing the concentration of nanoparticles used to eliminate MRSA and reduce any potential side effects. Control experiments with AgNPs of equivalent concentrations were assessed to validate the dual-step irradiation setup further. Figure S14 depicts the results under dark and light conditions using AgNPs. In the absence of light, a minimal inactivation effect is observed for AgNPs; however, under light conditions, a log reduction of 3.2, 2.8, and 1.6 was determined at concentrations of AgNPs of 1.5, 1.0, and 0.5 µg/mL respectively, which is still significantly lower than those achieved by PpIX-AgNPs.

Previous studies have revealed that bacterial culture media negatively impacts the activity of metal ions and AgNPs [68, 162, 198]. We hypothesize that the dual-step irradiation strategy can overcome the limitations of AgNPs by enhancing the Ag+ release. Based on the favorable colloidal stability of PpIX-AgNPs in NB and the light-mediated controlled release of Ag^{+}, we tested the antibacterial action of PpIX-AgNPs against MRSA in NB medium at a concentration of 1.5 and 5.0 µg/mL. First, we evaluated the performance of the nanoplatform in overgrowth conditions of MRSA with an initial concentration of ~10^{8} CFU/mL. As seen in **Figure 3.5c**, at a concentration of 1.5 µg/mL, the PpIX-AgNP single and dual-step irradiation modes showed minimal inactivation (<1 log) in NB, corroborating the major impact of the cell medium on the performance of AgNPs [162, 198]. We increased the concentration of PpIX-AgNPs to 5.0 µg/mL and tested the antibacterial response under a dual-step irradiation setup. A 1.83, 2.73, and 2.00 log reduction in the MRSA population at 0, 4, and 24 h post-irradiation was determined. However, the cysPpIX concentration was also tested under the same conditions, resulting in a 5-log reduction across all

post-irradiation times (Figure S15). This can be attributed to increased sensitization of gram-positive bacteria to PDI [38, 40]. Next, we tested the effect of PpIX-AgNPs at a similar concentration (5 μg/mL) with a reduced initial bacterial load corresponding to ~10^7 CFU/mL (**Figure 3.5c**). Under these conditions, the inactivation of MRSA resulted in 2.31, 2.88, and 4.92 log reduction at 0, 4, and 24 h post-irradiation. These results point to an essential factor contributing to the antibacterial activity, i.e., initial bacterial load. It was observed that these light-activated PpIX-AgNPs work more effectively at lower bacterial loads. Most NP-based studies demonstrating antibacterial action against MRSA generally use initial bacterial cell density in 10^5-10^7 CFU/mL [23, 101, 199, 200]. Thus, significant optimization in terms of initial bacterial load is required to further explore the antibacterial properties of these light-activated silver nanoparticles.

3.4 Conclusions

In this work, we studied the role of culture media composition and light irradiation modulation strategy on Ag^+ release kinetics for PpIX-AgNP. These Ag^+ release profiles under varying light irradiation setups and culture conditions were correlated to the light-activated antibacterial action of PpX-AgNP in MRSA. The salt and protein content plays a major role in affecting the colloidal stability, wherein PpIX-AgNP in NB displayed the highest stability. The salt and protein content also influences the Ag^+ release kinetics, with media with high salt content such as DPBS and LB showing maximum release, and media with high protein content showing limited release (TSB and NB) under single irradiation. Furthermore, we hypothesized that modulating the irradiation strategy could also maximize the Ag^+ release and promote effective antibacterial action at lower concentrations. We successfully proved our hypothesis that a dual-step irradiation setup (2 irradiation cycles) can effectively increase Ag^+ release at lower concentrations, thereby requiring 33% and 67% lower PpIX-AgNP concentrations to achieve similar antibacterial action.

In DPBS, the dual-step irradiation resulted in a 6-log and 5-log reduction in the MRSA population at PpIX-AgNP concentrations that were 33% (1 µg/mL) and 67% (0.5 µg/mL) lower than the original concentration, i.e., 1.5 µg/mL. However, the antibacterial actions in NB were attenuated and required a higher PpIX concentration (5.0 µg/mL) and dual-step irradiation strategy at reduced bacterial load to achieve ~ 5-log reduction in MRSA population.

3.5 Appendix B (Supporting information)

3.5.1 Schemes

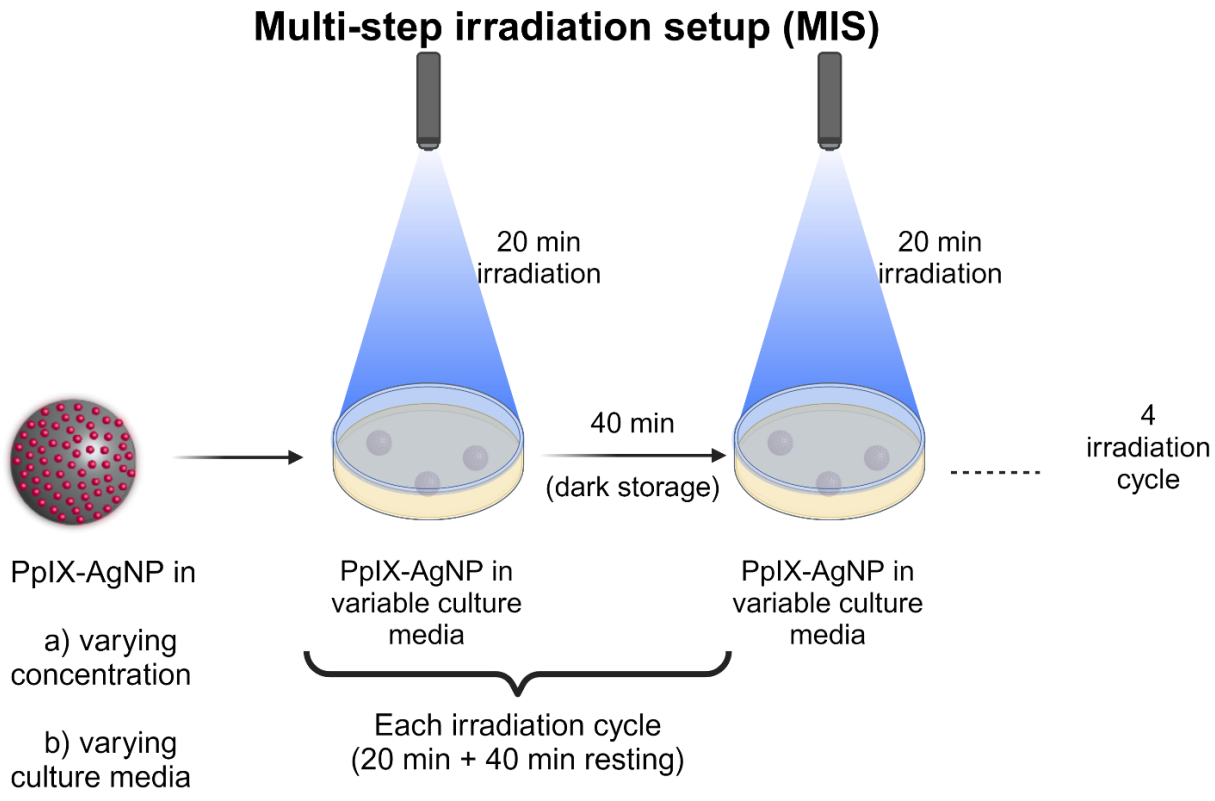

Scheme S1. Schematic explaining the experimental design for multi-step irradiation and dual-step irradiation setup.

3.5.2 Supporting Figures

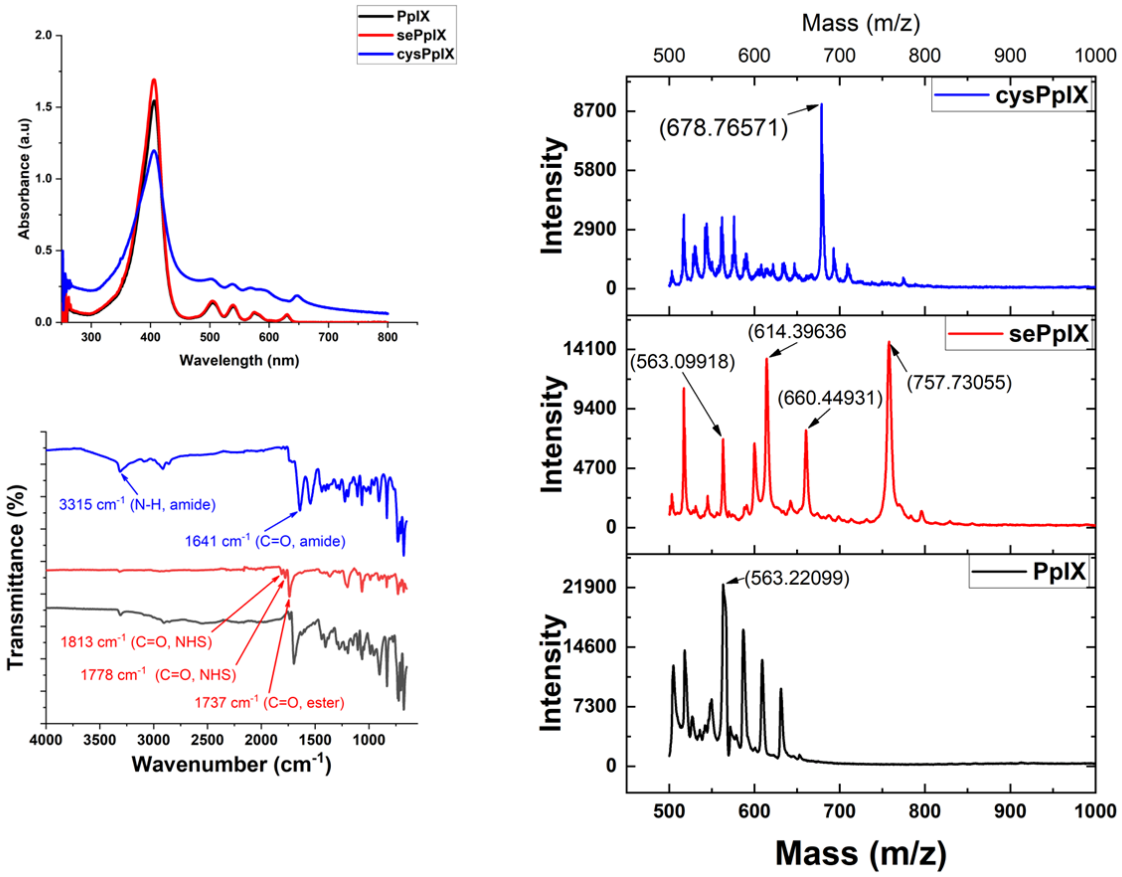

Figure S1. UV-Vis (DMF), FT-IR, MALDI-MS spectra for PpIX (black), sePpIX (red) and cysPpIX (blue). Expected m/z: $[PpIX]^+$ = 562.66 / Observed: m/z: $[PpIX]^+$ = 563.22; Expected m/z: $[sePpIX]^+$ = 756.84/Observed: m/z: $[sePpIX+2]^+$ = 757.73; Expected m/z: $[cysPpIX]^+$ = 680.93/ Observed: m/z: $[cysPpIX-2]^+$ = 678.76.

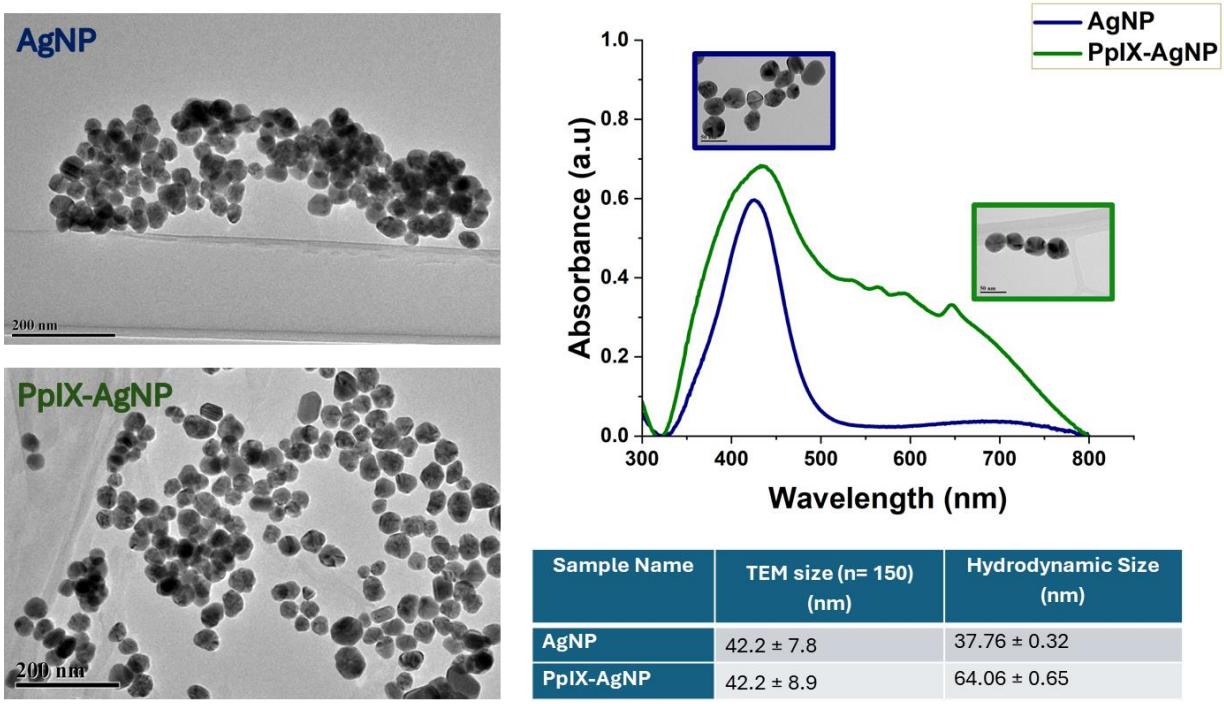

Sample Name	TEM size (n= 150) (nm)	Hydrodynamic Size (nm)
AgNP	42.2 ± 7.8	37.76 ± 0.32
PpIX-AgNP	42.2 ± 8.9	64.06 ± 0.65

Figure S2. TEM images, UV-Vis spectra (DMF), hydrodynamic size, and polydispersity index for AgNP and PpIX-AgNP.

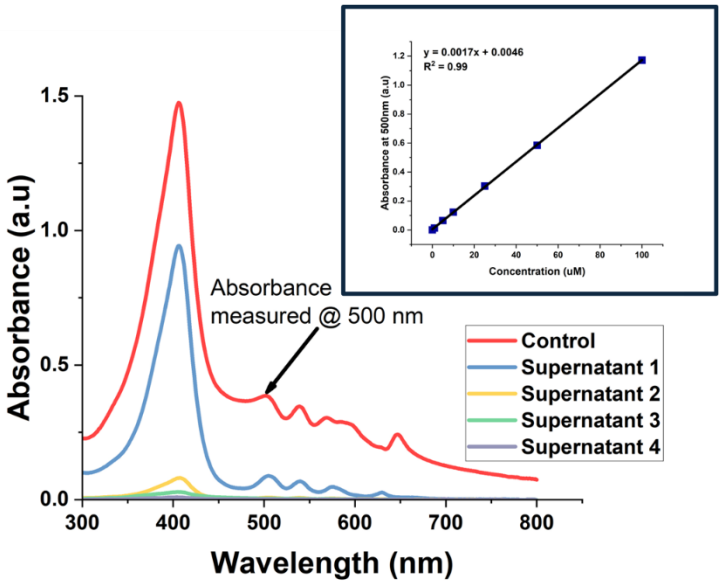

Figure S3. UV-Vis plot for supernatants collected before (control) and after (Supernatant 1-4) the reaction between cysPpIX and AgNP. (inlet) Calibration curve for the quantification of cysPpIX (generated using absorbance at 500 nM).

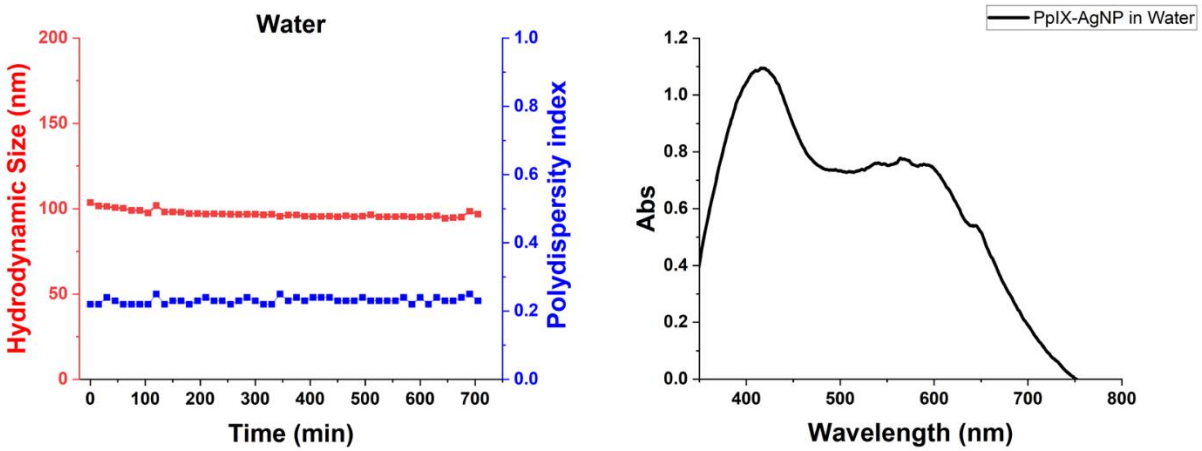

Figure S4. Colloidal stability of PpIX-AgNP in water. Time-resolved hydrodynamic size and PdI for 12 hours. UV-Vis of PpIX-AgNP in water (right).

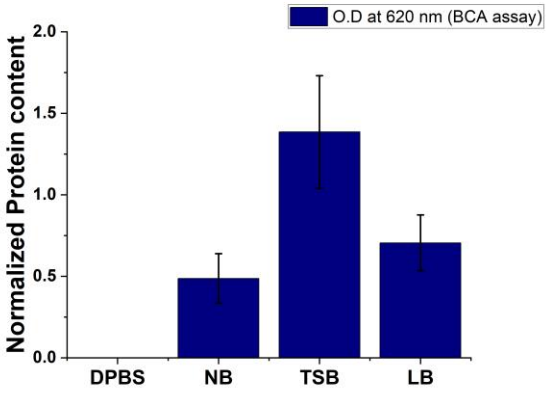

Figure S5. Qualitative assessment of protein content on PpIX-AgNP surface incubated in bacterial culture conditions post 24-hour incubation calculated using BCA assay.

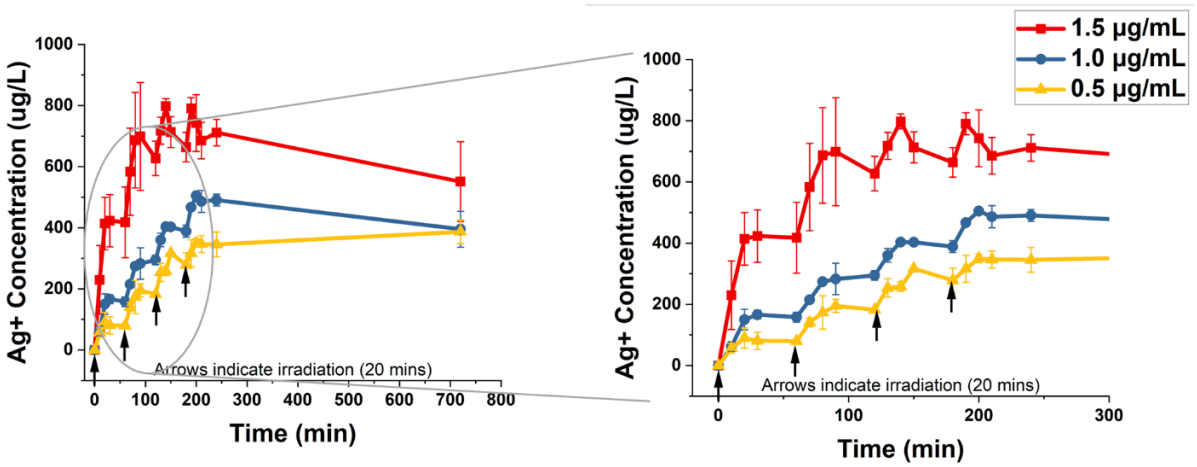

Figure S6. Cumulative Ag+ release kinetics for varying concentrations of PpIX-AgNP under multi-step irradiation (MIS) setup.

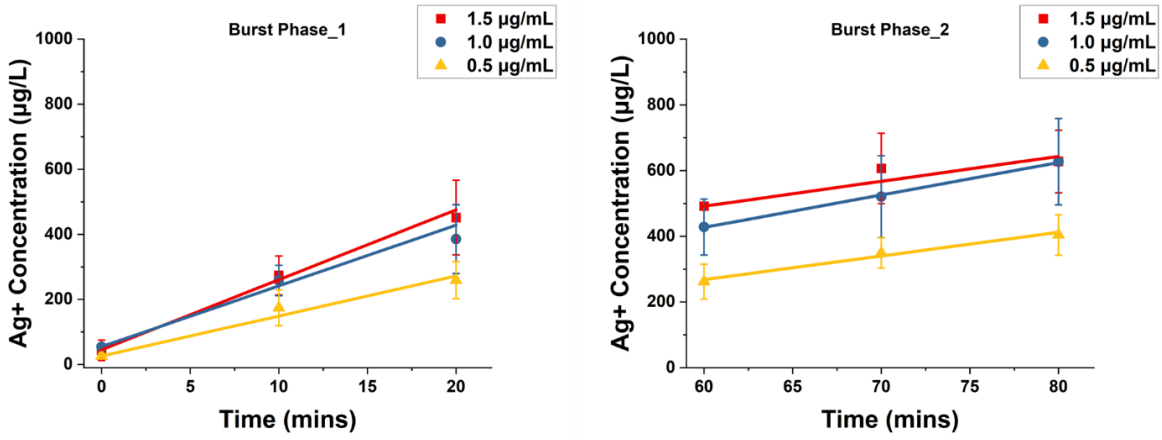

Figure S7. Kinetic release linear fitted plots for varying concentrations of PpIX-AgNP in DPBS under dual-step irradiation setup.

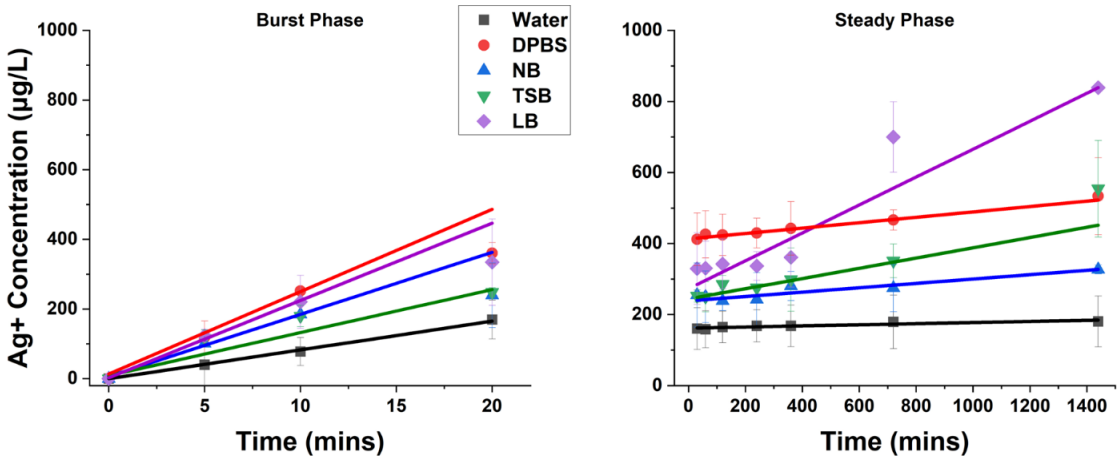

Figure S8. Kinetic release linear fitted plots for PpIX-AgNP in DPBS and bacterial culture conditions under single irradiation setup.

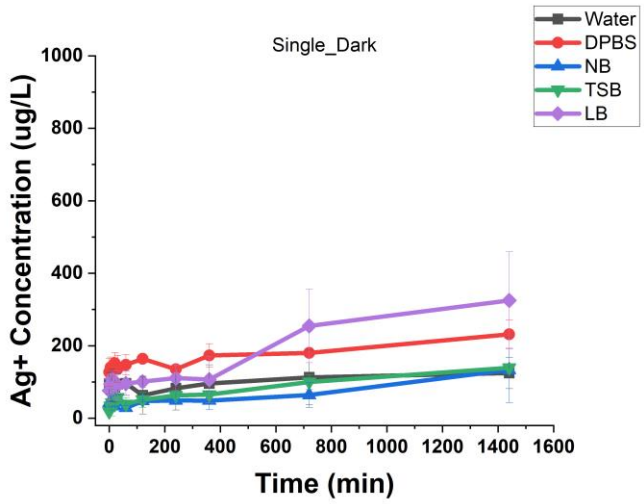

Figure S9. Ag^{+} release kinetics in the absence of light PpIX-AgNP in DPBS and bacterial culture conditions under the single irradiation setup.

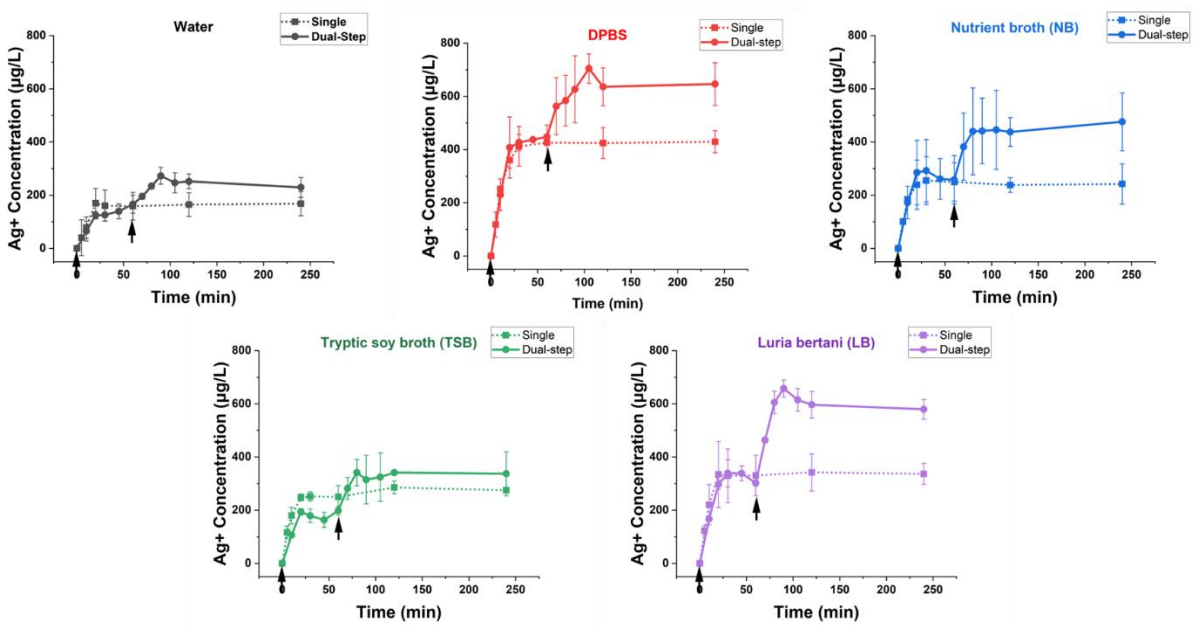

Figure S10. Comparison of Ag+ release kinetics for PpIX-AgNP (1.5 µg/mL) under single and dual-step irradiation setup for water, DPBS, and bacterial culture conditions.

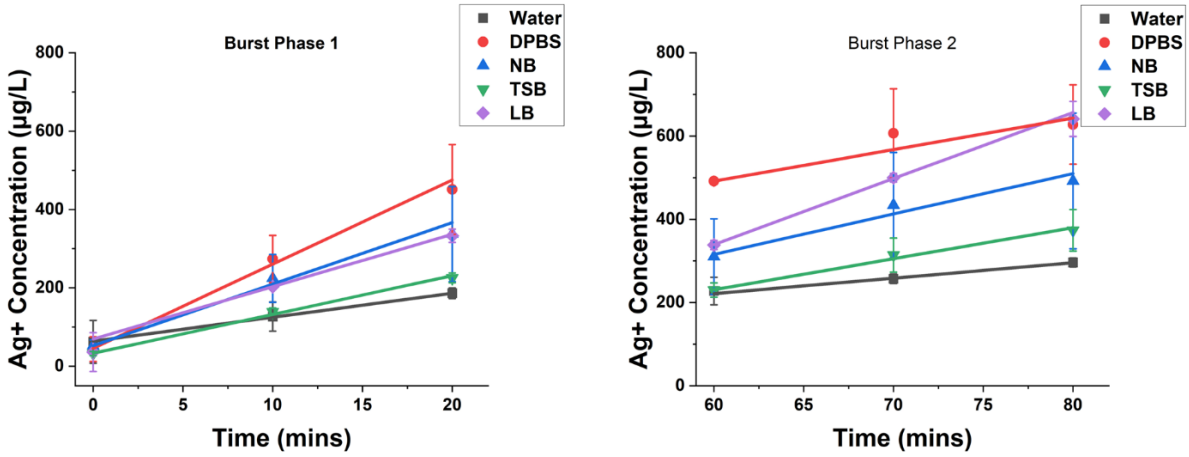

Figure S11. Kinetic release linear fitted plots for PpIX-AgNP in DPBS and bacterial culture conditions under dual-step irradiation setup.

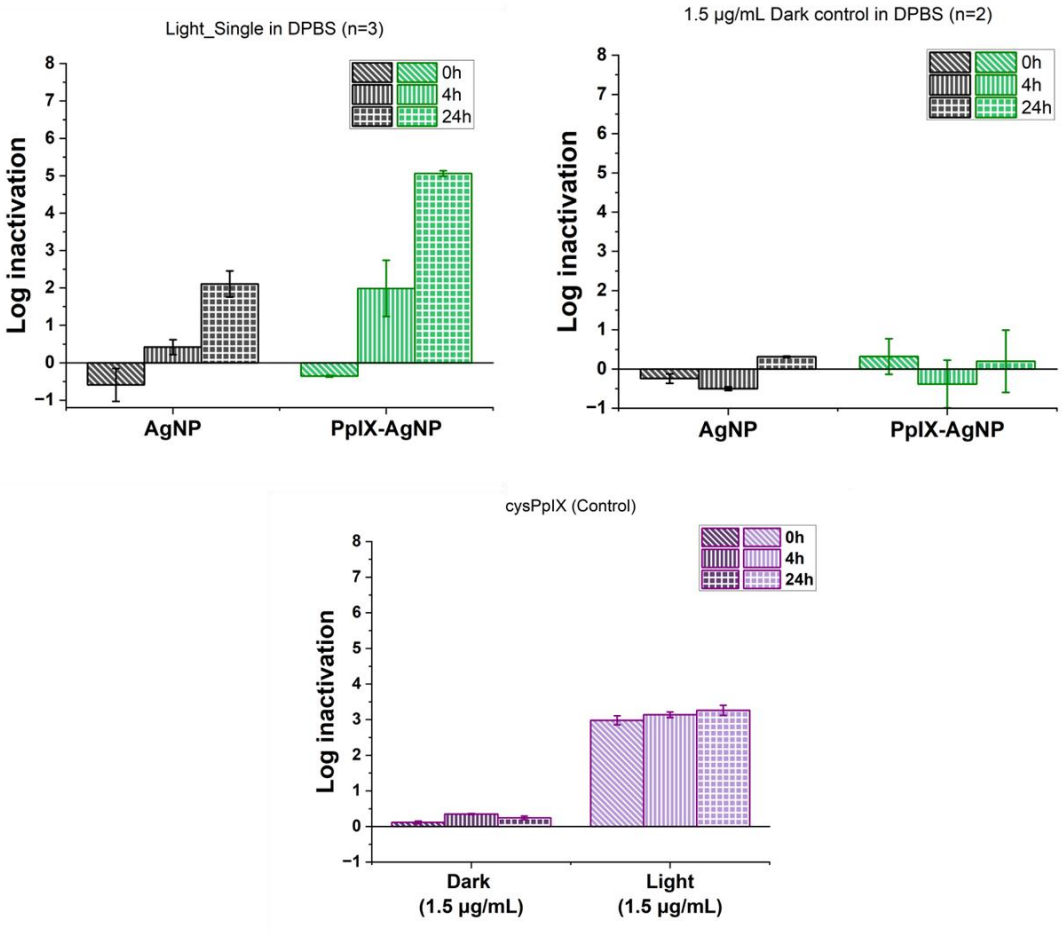

Figure S12. Antibacterial activity of light and dark controls for AgNP and cysPpIX tested in MRSA under single irradiation setup.

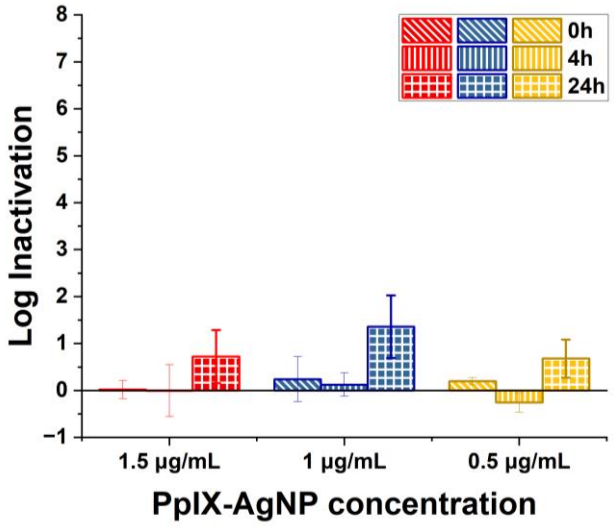

Figure S13. The antibacterial activity of varying concentrations of PpIX-AgNP in DPBS in the absence of light.

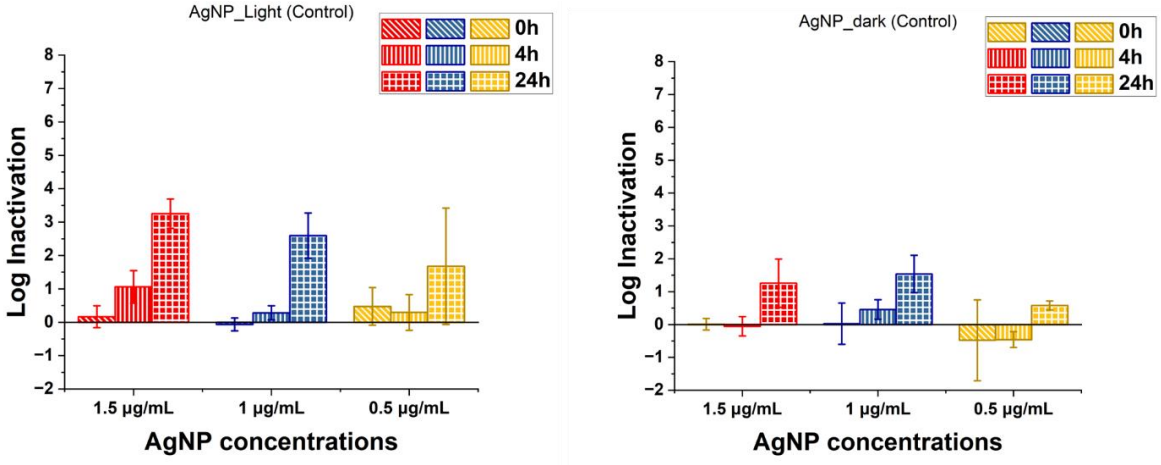

Figure S14. The antibacterial activity of varying concentrations of AgNP in DPBS under (left) dual-step irradiation setup and (right) in the absence of light i.e. dark control.

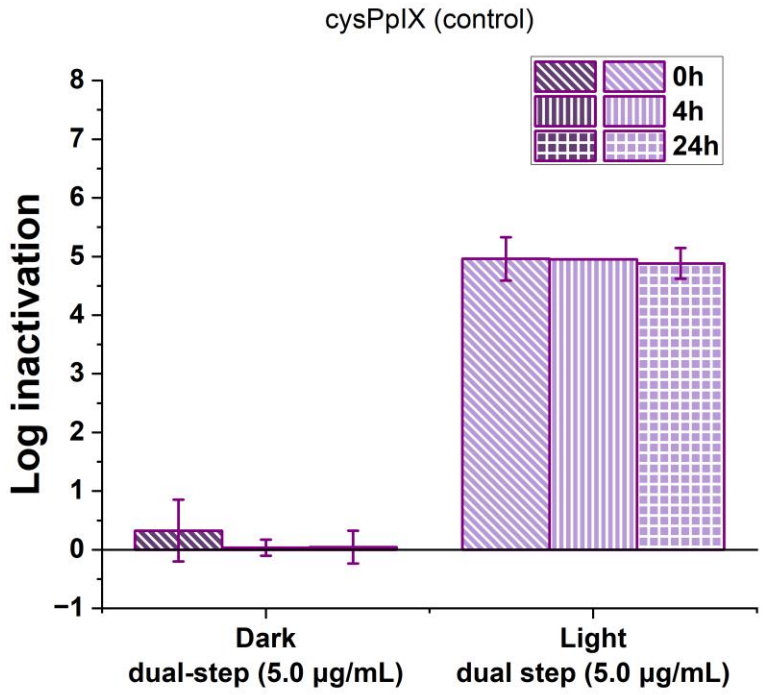

Figure S15. The antibacterial activity of PpIX-AgNP in NB under dual-step irradiation setup.

3.5.3 Supporting Tables

Table S1. TEM size, Hydrodynamic size, and ζ-potential for AgNP and PpIX-AgNP in DPBS (1 mM)

Sample Name	**TEM size (n= 150) (nm)**	**Hydrodynamic Size (nm)**	**ζ-potential (mV)**
AgNP	42.2 ± 7.8	37.76 ± 0.32	-47.10 ± 3.60
PpIX-AgNP	42.2 ± 8.9	64.06 ± 0.65	-56.70 ± 3.00

Table S2. Summary of ζ-potential for PpIX-AgNP in various culture media and DPBS at 0 hours and 24 hours.

Sample Name	**0 hour**	**24 hours**
DPBS (1 mM)	-38.4 ± 0.8 mV	-34.4 ± 4.1
DPBS (10 mM)	-21.4 ± 1.5 mV	-24.1 ± 1.8
NB	-17.8 ± 0.4 mV	-19.1 ± 0.7
TSB	-23.1 ± 1.8 mV	-21.1 ± 1.0
LB	-18.7 ± 1.3 mV	-16.5 ± 1.3

Table S3. Composition of bacterial culture media. (adjusted to 1L solution)

Ingredients	NB	Tryptic Soy Broth	Luria Broth	DPBS
Glucose	1 gram	2.5 grams	-	-
Peptone	15 grams	-	-	-
Sodium Chloride	6 grams	5 grams	10 grams	8 grams
Yeast Extract	3 grams	-	5 grams	-
Tryptone (SELECT)	-	17 grams	10 grams	-
Soytone (Soybean)	-	3 grams	-	-
Dipotassium Phosphate	-	2.5 grams	-	0.2 grams
Potassium chloride	-	-	-	0.2 grams
Sodium Phosphate (dibasic)	-	-	-	1.15 grams
Extra components such pH adjuster	pH 7.5 ± 0.2	pH 7.3 ± 0.2	pH 7.0; NaOH	

Table S4. Salt and protein content (in w/v %) in varying media conditions. The % of protein content includes peptone, tryptone, soytone, and yeast extract. In the case of % of the salt content includes sodium chloride, dipotassium phosphate, and potassium chloride.

Culture media	w/v % of salt	w/v % of protein
DPBS	0.95	0
NB	0.6	1.8
TSB	0.8	2
LB	1	1.5

Table S5. ICP-OES digestion results for varying concentrations of PpIX-AgNPs.

Sample Name	Total Ag^+ amount (ug/L)	
	Average	Std Dev
1.5 ug/mL PpIX-AgNP	2749.92	45.91

1.0 ug/mL PpIX-AgNP	1786.24	195.93
0.5 ug/mL PpIX-AgNP	931.56	25.98

Table S6. Kinetic release rates for dual-step irradiation of varying PpIX-AgNP concentration

Media	**Phase**	**Slope**	**R2**
1.5 ug/mL	Burst_1	21.50	1.00
	Burst_2	7.58	0.95
1.0 ug/mL	Burst_1	18.68	0.99
	Burst_2	9.87	1.00
0.5 ug/mL	Burst_1	12.31	0.99
	Burst_2	7.20	0.98

Table S7. Kinetic release rates for single irradiation in varying culture media

Media	**Phase**	**Slope**	**R^2**
Water	Burst	8.26	0.99
	Steady	0.02	0.90
DPBS	Burst	23.66	0.97
	Steady	0.07	0.98
NB	Burst	17.83	0.99
	Steady	0.06	0.98
TSB	Burst	12.34	0.98
	Steady	0.14	0.89
LB	Burst	22.21	0.98
	Steady	0.39	0.99

Table S8. Kinetic release rates for DIR irradiation in varying culture media

Media	**Phase**	**Slope**	**R^2**
Water	Burst_1	4.13	0.92
	Burst_2	3.55	1.00

DPBS	Burst_1	9.93	1.00
	Burst_2	6.61	0.82
NB	Burst_1	12.59	0.98
	Burst_2	7.79	0.94
TSB	Burst_1	7.77	1.00
	Burst_2	6.25	0.99
LB	Burst_1	10.64	1.00
	Burst_2	7.79	0.94

4 CHAPTER 4: PREVENTION OF BIOFILM FORMATION IN *V. CHOLERAE* AND INVESTIGATION OF TRANSPORT OF FLUORESCENT NANOPARTICLES WITHIN MOCK BIOFILMS

4.1 Introduction

Biofilms, prominently growing either on indwelling medical implants or dead/live tissue, account for up to 80% of all human bacterial infections contributing to the high mortality rates [29]. In biofilms, extracellular polymeric substance (EPS) serves as a physical barrier against the entry and antibacterial action of antibiotics. Bacteria within a biofilm are 1000 times more tolerant to antibiotics current treatment strategies require EPS-disrupting agents and high doses of antibiotic cocktails [201, 202] . This contributes to the aggressive use of antibiotics, which may lead to potential new resistance [27, 35, 36]. The current therapeutic challenges are attributed to limited penetration, slow or delayed diffusion, and altered microenvironment of EPS [35, 203]. Most bacterial biofilm development is associated with survival and persistence. Infectious bacterial strains that form biofilms on living tissues can worsen the infectious state within the body.

Cholera is an acute diarrheal disease that affects 3-5 million people annually, among which 100,000- 120,000 cases can be fatal [204]. *Vibrio cholerae* is a known water-borne gram negative bacteria, that can form biofilms during their aquatic (environment) and intestinal stage (human host) [205]. Vibrio polysaccharide (VPS), an exopolysaccharide, plays a crucial role in the formation of *V. cholerae* biofilms driving the generation of rugose and smooth strains [206, 207]. Among these, rugose strain is associated with the formation of corrugated colonies and mature biofilms [205]. The antibacterial action of AgNPs in *V. cholerae* is reported in the literature and mainly depends on the bacterial lifestyle (planktonic or biofilm). Recent reports have indicated that AgNP-based nanocomposites can eliminate planktonic bacteria and prevent biofilm formation at concentrations

as low as 4 μg/mL [208, 209]. The RT-PCR-based study reported here indicates that the presence of AgNP causes a significant decrease in vpsL expression (VPS production gene) [208]. Another study tested chitosan and alginate-stabilized AgNPs in mature *V. cholerae* biofilms and presented SEM analysis showing that chitosan-stabilized AgNPs successfully interacted and disrupted the EPS microstructure of rugose strain *V. cholerae* biofilms [210]. The authors tested and exposed both these AgNP types to mutant variants of rugose (non-biofilm strains) and concluded that the removal of the Bap1 gene increases the susceptibility of rugose strain to AgNPs. Owing to the advantage of AgNPs, we tested the PpIX-AgNPs in a rugose strain of *V. cholerae* to assess for the inhibition of biofilm formation. So far, there has been no study demonstrating the effect of PDI on *V. cholerae*.

Most PS-AgNP combinations so far tested in biofilms have focused mainly on inhibition rather than elimination [110, 113, 114]. In mature biofilm, the presence of a complex EPS layer is known to limit the penetration of NPs. The EPS of mature biofilms is composed of individual polysaccharides, proteins, lipids, and nucleic acids. The polysaccharide component makes up to 95% (by weight) of the EPS structure and is responsible for adhesion, and structural integrity [31]. Most reported methods to disrupt EPS involve targeting critical structural components of EPS and inactivating them using enzymes, and mucolytic agents to ensure disruption of eDNA, proteins, and polysaccharides [211-217]. NPs can play a crucial role in delivering these EPS-disrupting agents [30]. The ideal performance of NPs requires their successful accumulation within the EPS matrix. However, most of the NPs can only achieve attachment to the biofilm surface, because their transport within the biofilm is affected by the viscosity, cell density, and porosity of the EPS matrix [218]. The physicochemical characteristics of the NPs such as size, shape, surface charge, hydrophobicity, and functional groups, are major factors that have an impact on this interaction [30]. Li et al reported that positively charged QD with hydrophobic surface groups showed better

penetration compared to negatively or neutral-charged QD [219]. Several studies report that NPs with a size less than 100 nm with a positive charge and hydrophobic surface achieve better penetration and diffusion within biofilms [219-224]. Dunsing et al reported that post EPS disruption the diffusion coefficient of 20 and 60 nm NPs were close to that in water [224]. The cross-linking of EPS and bacterial cell density also influences the NPs migration within the biofilm [224, 225]. A fundamental understanding of the NP interaction and transport within EPS would help improve NP's ability to eliminate mature biofilms.

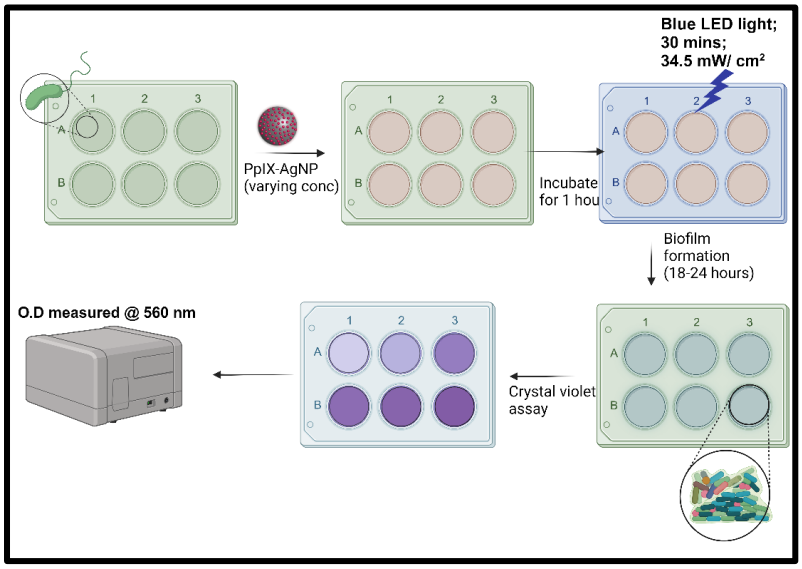

Figure 4.1 The optimized experimental setup for light-activated biofilm inhibition was quantified using crystal violet assay for PpIX-AgNPs.

We studied the light-activated biofilm inhibition activity of PpIX-AgNPs in *V. cholerae* (rugose strain). As seen in **Figure 4.1**, the experimental setup was optimized to test variable concentrations of PpIX-AgNPs in planktonic *V. cholerae*, and the biomass of the formed biofilms was quantified using crystal violet assay. Crystal violet staining assesses the total biomass of the biofilms [226]. The first section of the results focuses on the *V. cholerae* biofilm inhibition. The

application of NPs for the disruption and removal of mature biofilm requires a a deeper understanding of their interaction with the EPS matrix. To simulate an EPS matrix, a mock biofilm (calcium alginate matrix) was optimized and generated. Further, fluorescent nanoparticles (FNPs) and confocal laser scanning microscopy (CLSM) were employed to understand the transport and interaction of the NPs with the mock biofilm. The latter section of the results focuses on this.

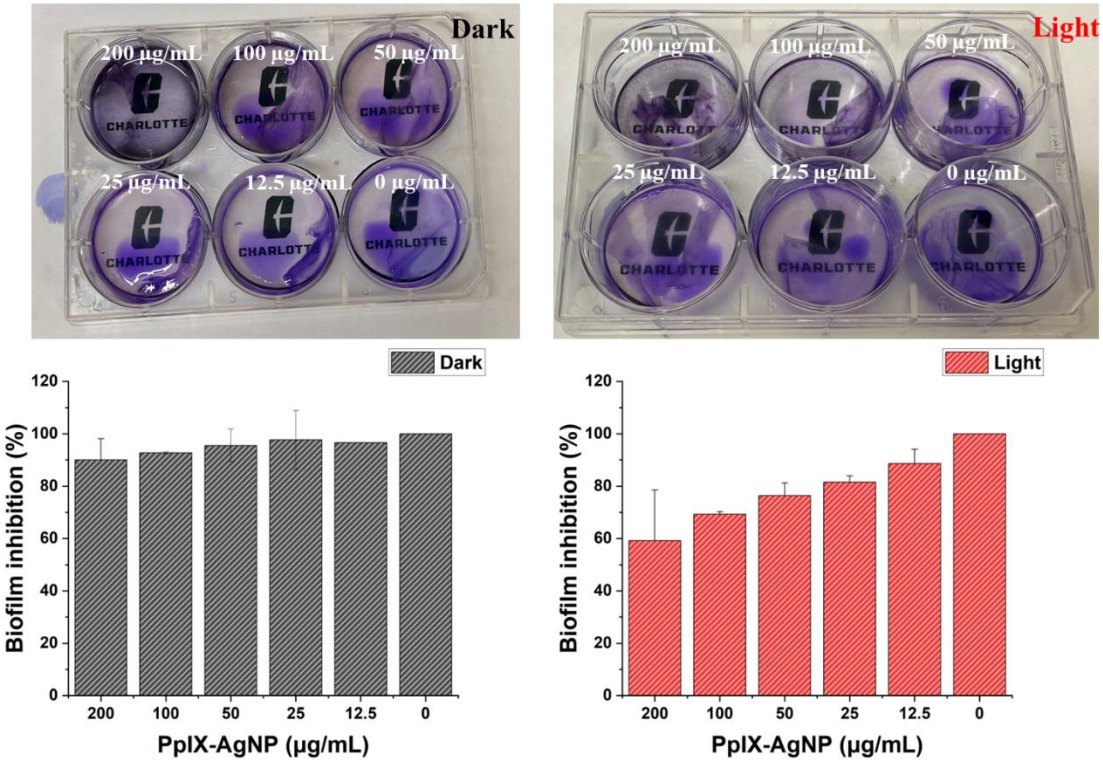

Figure 4.2 (top)Visual images of biofilms post crystal violet staining. (bottom) Biofilm formation post treatment with varying concentrations of PpIX-AgNPs tested in *V. cholerae* under light and dark conditions.

4.2 Results and Discussions

4.2.1 Light-activated PpIX-AgNPs for the inhibition of *V. cholerae* biofilms

The PpIX-AgNP synthesized and characterized in the previous chapters were tested in terms of biofilm inhibition in *V. cholerae* (rugose). The *V. cholerae* (initial cell density corresponding to O.D @ 600 nm) were exposed to various concentrations of PpIX-AgNP (in LB broth), i.e. 200 µg/mL, 100 µg/mL, 50 µg/mL, 25 µg/mL, and 12.5 µg/mL. The PpIX-AgNPs stocks for each concentration were prepared in DMF (at 100 higher concentration) and equal volume from each stock concentration was added to the 6-well plate containing the *V. cholerae* bacteria. The % of DMF in each well-kept constant at 2 % including the negative control (0 µg/mL). During the initial optimization, it was noted that DMF levels as low as 5% can reduce the bacterial level and interfere with the experimental setup. It should be noted that the highest concentration (200 µg/mL) resulted in the formation of a black precipitate (both dark and light conditions), as visualized in **Figure 4.2**. As shown in **Figure 4.2**, PpIX-AgNP in dark control shows minimal changes in biofilm formation among all PpIX-AgNP concentrations. For dark conditions, 200 µg/mL resulted in the lowest biofilm formation (90%). In light conditions, the increasing PpIX-AgNP concentration resulted in increased trends in inhibition of biofilm formation, with the maximum 60% achieved for PpIX-AgNP concentration = 200 µg/mL. To elucidate that PpIX-AgNP synergy is driving this biofilm inhibition, we tested AgNP and PpIX (or cysPpIX) at concentrations equivalent to PpIX-AgNP (100 µg/mL). The PpIX concentration tested here is 44 µM and AgNP concentration tested is 70 µg/mL. As seen in **Figure 4.3**, dark controls among all the treatments show no changes in the biofilm formation. However, under light irradiation, PpIX-AgNP (100 µg/mL) shows significant reduction in biofilm formation than PpIX

($p = 0.023$). This observed reduction for PpIX-AgNP treated bacteria is not statistically significant when compared to light-exposed AgNP ($p > 0.05$).

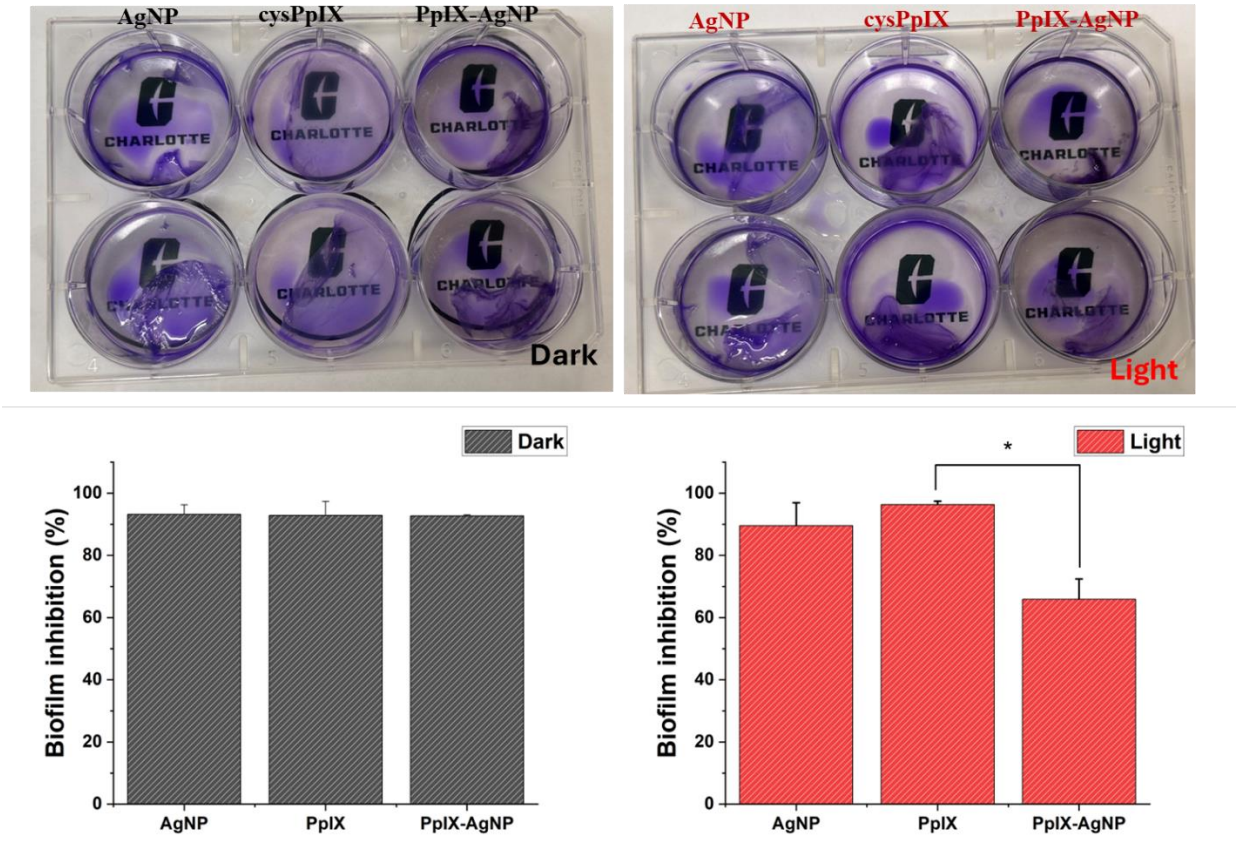

Figure 4.3 (top)Visual images of biofilm formed post crystal violet staining. (bottom) Biofilm formation post-treatment with AgNP (70 µg/mL), cysPpIX (44 µM)and, PpIX-AgNPs (100 µg/mL) tested in *V. cholerae* under light and dark conditions.

4.2.2 Optimization of Mock Biofilm Generation

Alginate matrix crosslinked with divalent cations such as Ca^{2+} were used to simulate the EPS structure of the biofilm based on previous reports [225]. Studies have indicated that the presence of Ca^{2+} affects the structure and thickness of most biofilms [224, 225, 227]. Reports have indicated that the calcium alginate matrix mimics the crosslinking mechanism and rheological behavior of real

biofilms [228]. Thus, these calcium alginate matrices crosslinked with Ca^{2+} were termed "mock biofilms" and used to investigate the transport of fluorescent NPs (FNP). The transport of NPs was monitored using confocal microscopy enabled with z-stacking.

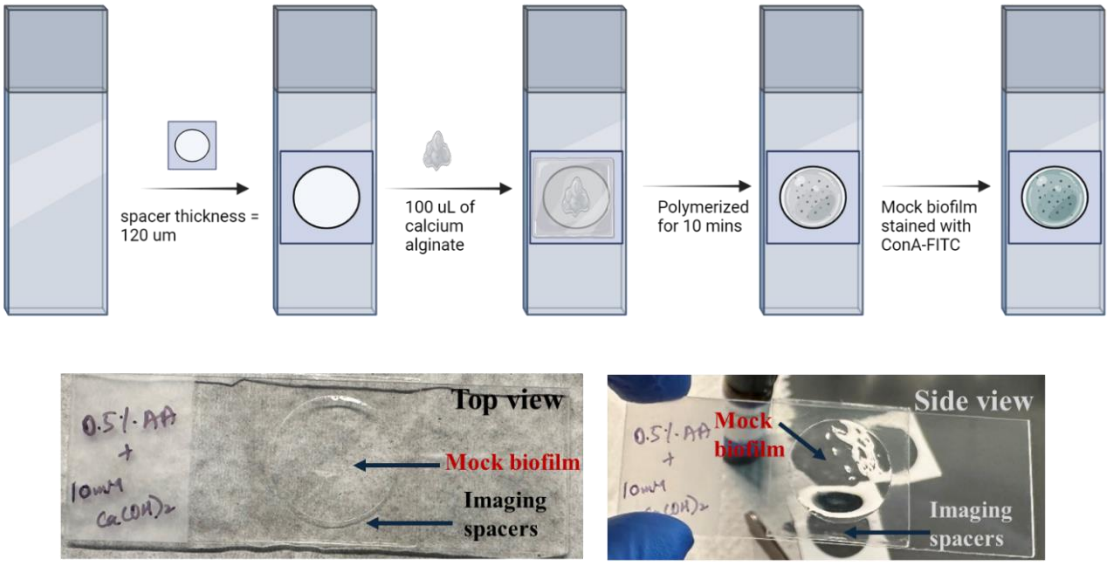

Figure 4.4 Mock biofilms were generated using the optimized protocol. (top) Schematic demonstrating the optimized protocol for the generation of mock biofilms. (bottom)The top view (left) and side view (right), show the location of spacers and mock biofilm.

The mock biofilm generation was first optimized by varying the concentration and ratio of alginic acid (AA) and calcium hydroxide ($Ca(OH)_2$). These variations (prepared in water) included, i) 0.25 % AA + 10 mM of $Ca(OH)_2$; ii) 0.5 % AA + 10 mM of $Ca(OH)_2$; iii) 0.25 % AA + 1 mM of $Ca(OH)_2$; and iv) 0.25 % AA + 10 mM of $Ca(OH)_2$. Among these, the variation (ii) resulted in the generation of calcium alginate with appropriate polymerization. Other ratios either didn't polymerize or didn't display extensive cross-linking making them difficult to handle (white layer formed). The mock biofilm generation was further adapted to use aqueous solutions of 0.5 % AA + 10 mM of $Ca(OH)_2$ such that the matrix is formed on a glass slide containing imaging

spacers (**Figure 4.4**). The imaging spacers ensured that the thickness of the mock biofilm was limited to 120 µm. To mimic the salt content in real biofilms, we attempted to make these mock biofilms in Dulbecco's phosphate buffer saline. However, it was observed that the presence of buffers with salt biofilm formation was hindered. Thus, mock biofilms were generated using aqueous solutions of AA and Ca $(OH)_2$, wherein the obtained calcium alginate matrix was mounted on a glass slide containing imaging spacers.

Furthermore, the staining of the mock biofilm was done using concanavalin A (ConA) linked to FITC. The ConA-FITC staining protocol was optimized to ensure even FITC staining across the mock biofilm. We tested two staining conditions, i) Con-A FITC stain mixed with calcium alginate matrix and then mounted on a glass slide; ii) mock biofilm was mounted first and then Con-A FITC was added on top and incubated for 6-12 hours. Among these two, as seen in **Figures 4.5a** and b, the second condition clearly shows successful staining across the mock biofilm area. The mean fluorescent intensity (MFI) calculated for the mock biofilms clearly shows that successful staining was accomplished across most of the z-height of the mock biofilm (**Figure 4.5c**). It should be noted that even staining of Con-A FITC was observed within a central region (as denoted in **Figure 4.5c**).

4.2.3 Investigation of FNP penetration and accumulation within mock biofilms

The Con-A FITC stained mock biofilms were exposed to FNP for variable periods and confocal images were obtained for each, to construct a time-based transport of FNPs across the mock biofilms. Post-generation of stained mock biofilms, the FMSN (100 µg/mL) was added on top of the mock biofilms and allowed to incubate for 3 hours, 6 hours, and 24 hours. Post respective incubation, the confocal images were generated to track the MFI for FNPs across the z-height. As shown in **Figures 4.6** a, b, and c, the FNPs show spikes in MFI at specific z-heights, whereas Con-

A staining remains consistent across the z-height. As seen in **Figure 4.6c**, at 3 hours most FNP seem to localize at 10 µm which moves further to 23 µm at 6 hours and finally reaches 45 µm at 24 hours. It should be noted that MFIs across the z-height resemble a Gaussian-like distribution (**Figure 4.6c**). The normalized values MFI indicate that the FNPs gradually move across the z-height of the mock biofilm. Based on this study, at 24 hours the maximum accumulation is achieved and FNPs can transport up to ~50 % of the total mock biofilm's thickness.

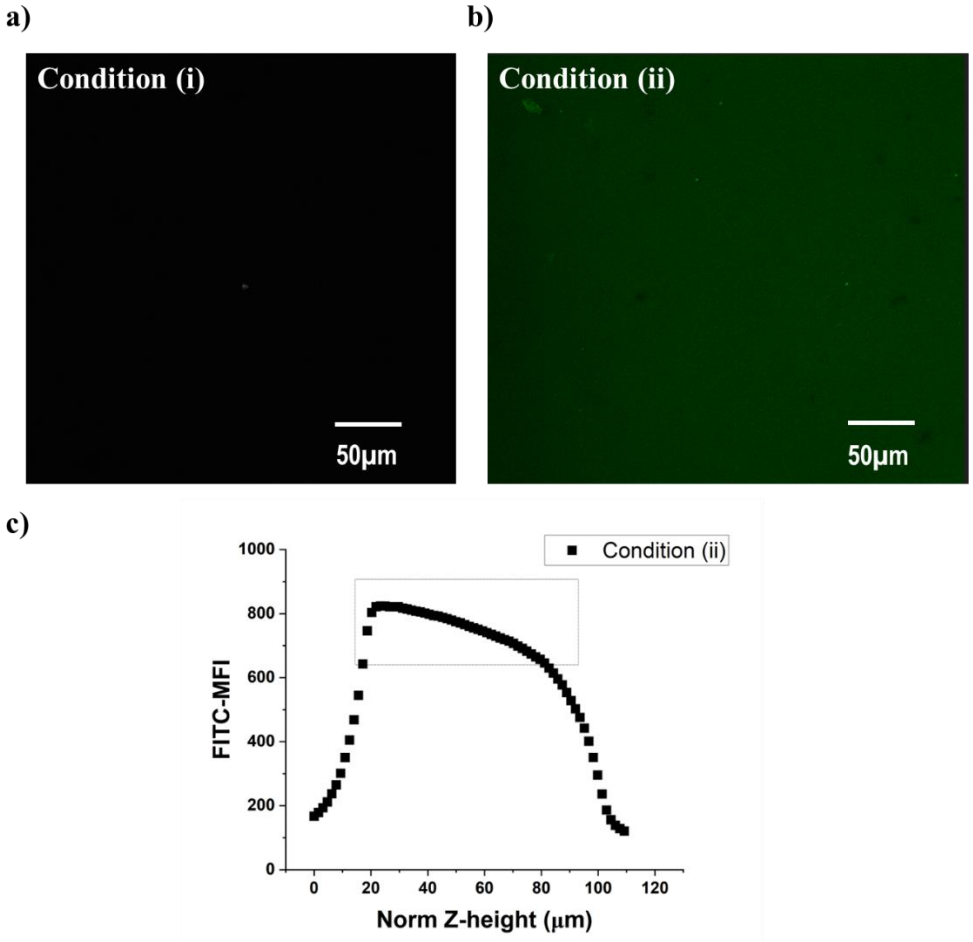

Figure 4.5 Confocal images for Con-A FITC stained mock biofilms testing two conditions. a) Con-A FITC stain mixed with mock biofilm and then mounted on a glass slide; b) mock biofilm

was mounted first and then Con-A FITC was added on top and incubated for 6-12 hours. c) MFI of FITC plotted against normalized z-height (condition ii tested).

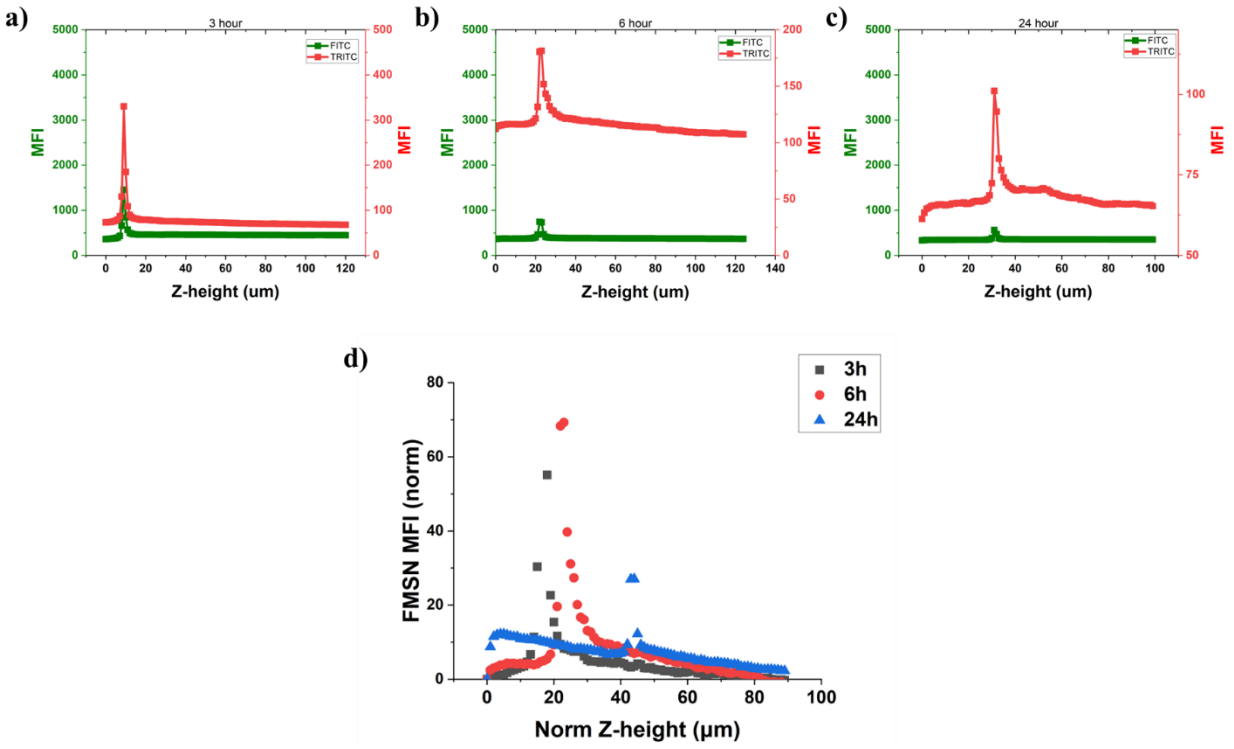

Figure 4.6 Transport of FNP across biofilms in terms of MFI post-incubation of a) 3 hours, b) 6 hours, and c) 24 hours. d) Normalized MFI plots for TRITC (FNPs) against normalized z-height indicating the distribution of FNPs across the mock biofilm for variable incubation times.

4.3 Experimental section

4.3.1 Materials and Instrumentation

The following chemicals and biological media were purchased from various suppliers: concentrated hydrochloric acid (Macron chemicals), nitric acid (Macron chemicals), protoporphyrin IX (Enzo Lifesciences). 1-Ethyl-3-(3-dimethylaminopropyl) carbodiimide hydrochloride (EDC) (Oakwood Chemicals), silver nitrate (AgNO3), cysteamine hydrochloride,

N-hydroxysuccinimide (NHS), dimethylamino pyridine (DMAP), N,N-Diisopropylethylamine (DIPEA), trisodium citrate dihydrate, (all from Sigma Aldrich), tannic acid (95%, Acros Organics), dimethyl sulfoxide, dimethylformamide (VWR chemicals) and dichloromethane (Alfa aesar), 1X Dulbecco's phosphate buffer saline (DPBS) (Corning), Luria Bertani (LB) broth, LB agar (VWR Life Science). All chemicals were of reagent grade purity or higher and were used as received. Biological media are certified nuclease-free. *Vibrio cholerae* O1 EITor (A1552) rugose variant was provided by Dr Troutman's lab. Crystal violet dye was purchased from Sigma Aldrich (Troutman Lab). Glacial acetic acid was obtained from VWR.

Cetyl trimethyl ammonium bromide (CTAB), Tetraethyl orthosilicate (TEOS), 1,3,5-trimethyl benzene (TMB, mesitylene), diethanolamine (DEA), Rhodamine B isothiocynate (TRITC), FITC - concavalin A conjugate, alginic acid sodium salt, calcium hydroxide were purchased from Sigma Aldrich. (3-aminopropyl)triethoxysilane was purchased from Alfa Aesar. Imaging spacers (thickness= 120 μm) were purchased from Grace Biolabs.

UV spectrophotometer was used to record the absorbance at 560 nm post crystal violet staining. For the confocal microscopy experiments, an Olympus FV1000 laser scanning confocal system was used. Mock biofilms were imaged using 60X (water immersion) objective (NA= 1.20), zoom of 2 at an image size of 1024 x 1024 (pixel). The z-height adjustments were varied at a resolution (step size) of 1 μm.

4.3.2 Biofilm inhibition test

A single bacterial colony of each strain was aseptically picked from the top of a glycerol stock of V. cholerae (rugose strain) using a sterile loop and inoculated into sterile LB broth media. Bacteria cells were grown overnight (~ 18 h) at 30 °C under continuous shaking. The overnight

cells were diluted with LB media to achieve an absorbance (@ 600 nm) of 0.5 O.D. In a 6 well plate, 2 mL of these cell suspension (O.D @ 600 nm = 0.5) was added along with 20 µL of varying concentrations of PpIX-AgNP stocks (concentration prepared in DMF). The respective PpIX-AgNP stocks were prepared in DMF such that the final concentrations in the well correspond to 200 µg/mL, 100 µg/mL, 50 µg/mL, 25 µg/mL, 12.5 µg/mL. For example, to achieve a final concentration of 100 µg/mL in the well, a stock of 5000 µg/mL in DMF was prepared. The stock solution gets diluted 50 times when 20 µL of this stock is added into a well containing 980 µL of bacterial culture in LB. The well with 20 µL of DMF was considered as negative control. The resulting DMF concentration in the final reaction volume was ≤ 2%. The plates were incubated in dark for 1 hour at 30 °C with intermittent shaking. Post incubation, the plates were irradiated for 30 minutes without stirring using a blue LED light source (450- 475 nm; 34.5 mW/cm^2). For the experimental group, a dark control plate was considered, which was kept in the dark. Post irradiation, the plates (treatment and dark control) were further incubated at 30 °C for 18 hours without shaking to allow biofilm growth. For control experiments, the above protocol was repeated with AgNP and cysPpIX concentration equivalent to 100 µg/mL, i.e., AgNP concentration is 70 µg/mL and cysPpIX (or PpIX) concentration is 44 µM.

4.3.3 Crystal violet assay

During this entire step, extra precautions were taken not to disturb the formed biofilm. The supernatant media in each well was carefully removed using a 1 mL micropipette without disturbing the biofilm formed at the bottom. Each well was rinsed with 1 mL of cold DPBS twice. To each well, 1 mL of 0.01 % crystal violet dye (in methanol) was added and incubated for 15- 20 mins. Following this, the crystal violet in each well was discarded and rinsed with 1 mL of DPBS. The remaining biofilm in each well was solubilized using 2 mL of 30 % glacial acetic acid, and

the absorbance was measured at 560 nm using a spectrophotometer. The following equation was used to evaluate the % biofilm inhibition for treatment conditions

Equation 4.1.

$$Biofilm\ formed\ (\%) = \frac{O.D\ at\ 560\ nm\ for\ treatment\ group}{O.D\ at\ 560\ nm\ for\ control\ group}$$

4.3.4 Synthesis of fluorescent NPs (FNPs)

The fluorescent NPs (FNP) were used for tracking their transport within the mock biofilm. The FNP used for this study are dendritic mesoporous silica nanoparticles tagged with fluorescent label, TRITC ($DMSN_{TRITC}$). To produce DMSNs, cetyltrimethylammonium bromide (CTAB) (390 mg, 1.07 mmol) was dissolved in ethanol (3.32 mL, 56.86 mmol) and nanopure water (21.6 mL) followed by the addition of diethanolamine (DEA) (41.4 µL, 0.428 mmol) under slow stirring at 60 ºC. Immediately, 1.0 mL of 1,3,5-trimethyl benzene was added to this solution and stirred for 4 hours. Tetraethyl orthosilicate (TEOS) (1.095 mL, 4.9 mmol) was then added dropwise over a period of 1-2 min. The mixture was further stirred for 18 h at 60 ºC. The nanoparticles were dialyzed against ethanol for 45 min. DMSNs were collected by centrifugation at 13,000 rpm for 15 min, washed three times with ethanol three times, and stored in ethanol. The surfactant template was extracted by washing the DMSNs in 1M HCl methanolic solution (10 mg of DMSNs in 1 mL of the acidic solution). The DMSNs were dispersed in the acidic solution and stirred for 10 h at 60 ºC. After the acid wash, DMSNs were collected via centrifugation and washed three times with ethanol. A second acid wash was performed under the same conditions for 6 h to optimize surfactant extraction. Finally, the surfactant-free DMSNs were washed with ethanol three times and stored in ethanol. The synthesis of FNP, (i.e. $DMSN_{TRITC}$) was carried out in two steps; first, TRITC (1.8 mg) was dissolved in 1 mL of dry DMF, APTES (5 µL, 21.3 µmol) was added and allowed to react for 3 h to afford TRITC-silane solution.

Second, DMSNs (100 mg) were dispersed in 30 mL of ethanol and allowed to stir at 60 °C. APTES (15 µL, 14.25 mg, 64.1 µmol) was mixed in 10 mL ethanol and then added dropwise to the DMSN dispersion. The reaction was mixed for 24 h at 60 °C. After the post-grafting process, TRITC-silane solution was added to the DMSN mixture and stirred for another 24 h at 60 °C under dark conditions. The FNPs were finally collected by centrifugation at 13,000 rpm for 15 min, washed with ethanol three times, and stored in ethanol.

4.3.5 Generation of mock biofilms for confocal imaging

Calcium alginate matrix (mock biofilms) were optimized and generated based on the modified version of previous reports [225]. All the solutions were prepared a day before the formation of mock biofilms. Briefly, 0.5 % (w/v) of alginate (alginic acid sodium salt) in water was prepared. Vigorous stirring and sonication were employed to dissolve the salt completely. An aqueous solution of calcium hydroxide with a concentration of 10 mM was prepared and stored at 4º C before use. Equal volumes (50 µL) of the alginic acid and $Ca(OH)_2$ were added on a strip of paraffin and mixed using a transfer pipette to form the mock biofilm. This mock biofilm was transferred to center of a glass slide containing the imaging spacer. This glass slide was covered with a cover glass wrapped in paraffin to spread the mock biofilm evenly. After 10 mins of contact, the cover glass was removed and the stained with 50 µL ConA-FITC (100 µg/mL) for 6 hours at 4º C. The cover glass wrapped in paraffin was placed on top to avoid drying issues. Post 6-hour incubation, FNPs (100 µg/mL) were added on the generated mock biofilm and incubated with for 3, 6 and 24 hours at 4º C. A separate mock biofilm sample (slide) was prepared for each time and post the respective incubation time the glass slide was prepared for confocal microscopy imaging. The NP tracking within the biofilm was performed using z-stack-enabled confocal microscopy.

4.3.6 Confocal Imaging and Analysis

The z-stack enabled confocal images of each sample were generated using an Olympus FV1000 laser scanning confocal system Samples were imaged using 60X (water immersion) objective (NA= 1.20), zoom of 2 at an image size of 1024 x 1024 (pixel). The FITC (corresponding to the mock biofilm) gain was kept consistent at 2.5 to ensure visualization across variable z-heights. The focus was adjusted to set the start and end z-height for each sample, based on the FITC intensity. The z-stack resolution was kept constant at 1.0 μm. The z-stack confocal image for each sample was exported in the multi-tiff format. Mean fluorescent intensity (MFI) for FITC and TRITC for each image within the z-stack, was calculated using ImageJ analysis. These calculated MFI were plotted against the respective normalized z-height.

4.3.7 Statistical analysis

Graphs and statistical analyses were performed using OriginPro 2024 (Academic Version). Statistical significance between treatment groups was calculated using a one-way analysis of variance (ANOVA), with the inclusion of Tukey test for mean comparison. All the statistical analyses were performed using OriginPro 2024 (Academic Version) with $\alpha = 0.05$ and reported as stars assigned to the p-values. The exact p values can be found within the main paper for the respective experiment.

4.4 Conclusions

In this chapter, we report a preliminary study evaluating the PpIX-AgNP's antibacterial action in (reported in the previous chapter) rugose (biofilm forming) strain of *V. cholerae*. The light-activated PpIX-AgNP displays 40% biofilm inhibition at a concentration 200 μg/mL and ~31% at 100 μg/mL. Furthermore, control experiments indicate that antibacterial action is driven by the PpIX and AgNP synergy. The mechanism driving the antibacterial synergy needs further validation

in terms of SEM and confocal analysis of biofilm formed post-light-assisted treatment of PpIX-AgNPs. In the latter section of the chapter, we successfully developed a protocol for the generation of mock biofilms, i.e., calcium alginate matrix. We further investigated the interaction of FNPs with the mock biofilm and evaluated the time-based transport of NP within these mock biofilms using CLSM. The FNPs show accumulation within 50 % distance of the mock biofilm post 24-hour incubation, indicating that NP transport is slow across the mock biofilms. However, these findings need to be validated by varying physiochemical parameters of the NP, such as size, surface charge, and surface functionalization.

4.5 Limitations

This chapter has limitations associated with the mock biofilms generation and investigation of NP transport within the mock biofilms that need to be pointed out. First, ensuring the mock biofilms generated are stored at 4 ºC is critical since the formed calcium alginate matrices (mock biofilms) are prone to drying effects at room temperature. During confocal microscopy analysis of mock biofilms, it should be noted that the FNPs were visible only at 60X water immersion magnification and not at 40X or 20X magnification. This can be associated with the lower concentration of the FNPs (100 µg/mL) introduced into the mock biofilms. As a result of high magnification, Z-stacked confocal images obtained here represent only a tiny area of the mock biofilms. Since the transport of NPs within biofilms is asymmetrical, obtaining the information representing a large area of the mock biofilms is crucial. This can be achieved by increasing the FNP concentrations or by capturing z-stack confocal images at multiple locations (x-y) within the mock biofilms. An alternative method would be to use a digital confocal instrument (PICO) with lower magnification (40X) and higher FNP concentrations to get detailed information corresponding to a maximum area of the mock biofilms to construct a 3-D visual graph representing the transport of NP within

the mock biofilms. Advanced image analysis tools can be implemented to remove background fluorescence associated with FITC and TRITC channels to ensure consistent fluorophore intensity. Finally, it is critical to reduce the resolution (1 μm used here) of the z-height data collected to obtain a better 3-D graph demonstrating the precise location of the FNPs within mock biofilms during these confocal image acquisition.

5 CHAPTER 5: CONCLUSIONS AND FUTURE DIRECTIONS

Nanoparticles such as AgNPs are an excellent candidate due to their unique optical and physiochemical properties and their innate broad-spectrum antibacterial activity. These properties combined the advantages of photodynamic inactivation (PDI) with AgNPs to demonstrate synergistic antibacterial activity. This research aims to develop light-activated silver nanoparticles by functionalizing photosensitizer (PS) on AgNP surface and investigate their light-responsive Ag^+ release kinetics to understand their role in the antibacterial synergy.

In Chapter 2, we synthesized, characterized, and demonstrated a light-activated PpIX-AgNP platform for eliminating ARBs, *MRSA,* and MDR *E. coli*. PpIX-AgNPs demonstrated broad-spectrum antibacterial action, resulting in > 7 log inactivation of MRSA and MDR *E. coli*. The ROS generated due to the irradiation of PpIX increased the release of Ag^+ from the surface of the PpIX-AgNPs. We also investigated the influence of the media composition on the release kinetics of Ag^+, wherein the light-activated PpIX-AgNPs in DPBS displayed 2.5 times higher Ag^+ release than in nanopure water. The cationic surface charge associated with PEI-PpIX-AgNP did not improve bacterial inactivation since it did not generate a similar Ag^+ release compared to PpIX-AgNP. The amount of released Ag^+ drives the inactivation of MDR *E. coli* and MRSA over electrostatic interaction from PpIX-AgNPs. In addition, PpIX-AgNPs overcame the limitations of PpIX molecules in the PDI of MDR *E. coli*. This light-activated PpIX-AgNP platform showed negligible cytotoxicity to HeLa cells at the bacterial inhibitory concentration after 24 h exposure. The successful formulation of light-activated PpIX-AgNPs with increased potential for Ag^+ release would reduce the MIC of AgNPs for therapeutic applications. However, these PpIX-AgNPs are known to be associated with poor colloidal stability in physiological conditions. This poor colloidal stability of these PpIX-AgNPs in realistic media, such as bacterial culture and bodily

fluids, may hinder their widespread antibacterial applications. Most of these PpIX-AgNPs are prone to precipitation or aggregation in culture media. Polymers such as PEI, polyvinylpyrrolidone (PVP), polyethylene glycol (PEG), and poly-L-lysine (PLL) can be employed via surface functionalization to improve colloidal stability. However, as seen in Chapter 2, it is crucial to note that any polymer functionalization of these PpIX-AgNPs can hinder Ag^+ release, thereby reducing its antibacterial properties. In the future, studies that enhance the colloidal stability of these PpIX-AgNP should consider evaluating the Ag^+ release kinetics as an essential design criterion. A study optimizing the polymer chain length, ratio, and molecular weight for optimal Ag^+ release can provide a robust light-activated platform. Furthermore, these PpIX-AgNP can be further studied for the light-activated elimination ARBs such as extended-spectrum β-lactamases (ESBL) producing *E. coli*, carbapenem-resistant *Pseudomonas aeruginosa* (CRPA) and vancomycin-resistant *Enterococcus faecium* (VRE). There have been reports that antibiotic-resistant genes (ARG) found in the environment can also be targeted using NPs. Considering the NP's extensive surface functionalization properties, the DNA sequence complementary to ARGs can be functionalized onto these PpIX-AgNP surfaces to ensure hybridization-based targeting of ARGs in water samples.

In Chapter 3, we evaluated the hypothesis that exposing PpIX-AgNP in a multi-step irradiation setup (MIS) could elevate the Ag^+ release and promote effective antibacterial action in *MRSA*. We proved our hypothesis that a dual-step irradiation setup (2 irradiation cycles) can effectively increase Ag^+ release efficiency, lowering the PpIX-AgNP concentration for antibacterial action. The lower concentration achieves a maximum AgNP to Ag^+ conversion efficiency of 40 %. MRSA inactivation results indicate that in DPBS, PpIX-AgNP concentrations as low as 1.0 and 0.5 μg/mL can result in up to 5-6 log inactivation. Additionally, we elucidate the critical role of culture

composition by assessing the colloidal stability of PpIX-AgNPs and generating their light-activated Ag^+ release kinetics in diverse bacterial cell culture media, i.e. Nutrient Broth, Tryptic Soy Broth, and Luria- Broth, post single and dual-step light irradiation. The salt and protein content plays a major role in influencing the colloidal stability and Ag^+ release kinetics, with media with high salt content such as DPBS and LB showing maximum release, and media with high protein content displaying limited release (TSB and NB). PpIX-AgNP in NB displayed the highest colloidal stability, and the inclusion of the dual-step irradiation mode doubled the Ag^+ release as compared to single irradiation in NB within 4 hours, thereby overcoming the limitation of lower Ag^+ release during the single irradiation setup. Finally, the antibacterial action of PpIX-AgNP (5 μg/mL) in NB against MRSA under dual-step irradiation mode displayed ~ 3-log inactivation. This response increased to a 5-log reduction when the initial bacterial load was reduced. The initial bacterial load plays a crucial role in demonstrating the antibacterial activity of any novel antimicrobials. Future experiments evaluating the correlation between reduced bacterial load (10^5-10^7 CFU/mL) and PpIX-AgNP concentration in realistic bacteria culture media such as NB can provide great insights for clinical applications. Including a dual-step irradiation setup can enable the controlled release of Ag^+, thereby applying these PpIX-AgNPs-based platforms for exploring light-controlled antibacterial applications. There is scope to modulate the light intensity and irradiation time to explore the application of these light-activated nanoparticles. For future experiments, comparing the MIC of silver cations with the Ag^+ release kinetics and electron imaging of bacteria can illuminate the exact mechanism driving the PS-AgNP antibacterial synergy. For their long-term wound-healing applications, it is also crucial to examine the colloidal stability and light-activated Ag^+ release of PpIX-AgNPs in a wound-like medium composed of bacterial culture media along with serum, hemolyzed blood, keratinocytes, and macrophages/

neutrophils. The effect of protein corona would be more pronounced in these conditions and would provide a realistic antibacterial action.

Chapter 4 presents preliminary work for applying these PpIX-AgNPs for biofilm inhibition and introducing a fluorescent-based approach utilizing confocal microscopy to understand the transport of NPs across mock biofilms. The light-activated PpIX-AgNP displays 40% biofilm inhibition at a concentration 200 µg/mL and ~31% at 100 µg/mL in Vibrio cholerae (rugose strain). Furthermore, control experiments indicate that antibacterial action is driven by the PpIX and AgNP synergy. The mechanism driving the antibacterial synergy needs further validation in terms of SEM and confocal analysis of biofilm formed post-light-assisted treatment of PpIX-AgNPs. We also investigated the interaction of FNPs with the mock biofilm and evaluated the time-based transport of NP within these mock biofilms using CLSM. The FNPs show accumulation within 50 % distance of the mock biofilm post 24-hour incubation, indicating that NP transport is slow across the mock biofilms. However, these findings need to be validated by varying physiochemical parameters of the NP, such as size, surface charge, and surface functionalization. A mock biofilm with inherent fluorescence properties, such as fluorescent alginate, can be generated to avoid an additional Con-A FITC staining of mock biofilms (associated with uneven staining). Biofilms are much more complex environments than bacteria and applying nanotechnology to combat biofilms requires detailed studies to understand the interaction and transport of NP with the biofilm matrix. Limitations associated with the confocal microscopy approach to study NP transport can be overcome by employing Raman active NPs such as silver nanoparticles for advanced tracking. Alternatively, a non-fluorescent method, such as quantitative phase imaging using silica nanoparticles, can assess NP diffusion within biofilms. In addition, the physiochemical properties of NP, such as AgNP, can be utilized to deliver multiple therapeutic agents, such as EPS-disrupting

mucolytic agents, such as polymyxin B, along with light-activated Ag^{+}-directed antibacterial action. We envision that the insights gained from this chapter would lead to developing a light-controlled therapeutic modality to eliminate biofilms for potential wound healing applications.

6 CHAPTER 6: REFERENCES

1. Ventola, C. L., The antibiotic resistance crisis: part 1: causes and threats. *P & T : a peer-reviewed journal for formulary management* **2015,** *40* (4), 277-283.
2. Brooks, B. D.; Brooks, A. E., Therapeutic strategies to combat antibiotic resistance. *Advanced Drug Delivery Reviews* **2014,** *78*, 14-27.
3. WHO World Priority List of Antibiotic-Resistant Bacteria to Guide Research, Discovery, and Development of New Antibiotics. . http://www.who.int/medicines/publications /WHO-PPL-Short_Summary_25Feb-ET_NM_WHO.pdf (accessed April 3,).
4. WHO Antimicrobial resistance global report on surveillance. https://apps.who.int/iris/bitstream/handle/10665/112642/9789241564748_eng.pdf;sequence=1 (accessed 17 March,).
5. CDC Antibiotic Resistance Threats in the United States. https://www.cdc.gov/drugresistance/pdf/threats-report/2019-ar-threats-report-508.pdf (accessed 17 March,).
6. (AMR), A. R. D., WHO Bacterial Priority Pathogens List, 2024: bacterial pathogens of public health importance to guide research, development and strategies to prevent and control antimicrobial resistance. . In *WHO Bacterial Priority Pathogens List, 2024*, Organization, W. H., Ed. Geneva: WHO, 2024.
7. WHO. Global Antimicrobial Resistance Surveillance System (GLASS. 2017.
8. Murray, C. J.; Ikuta, K. S.; Sharara, F.; Swetschinski, L.; Robles Aguilar, G.; Gray, A.; Han, C.; Bisignano, C.; Rao, P.; Wool, E.; Johnson, S. C.; Browne, A. J.; Chipeta, M. G.; Fell, F.; Hackett, S.; Haines-Woodhouse, G.; Kashef Hamadani, B. H.; Kumaran, E. A. P.; McManigal, B.; Agarwal, R.; Akech, S.; Albertson, S.; Amuasi, J.; Andrews, J.; Aravkin, A.; Ashley, E.; Bailey, F.; Baker, S.; Basnyat, B.; Bekker, A.; Bender, R.; Bethou, A.; Bielicki, J.; Boonkasidecha, S.; Bukosia, J.; Carvalheiro, C.; Castañeda-Orjuela, C.; Chansamouth, V.; Chaurasia, S.; Chiurchiù, S.; Chowdhury, F.; Cook, A. J.; Cooper, B.; Cressey, T. R.; Criollo-Mora, E.; Cunningham, M.; Darboe, S.; Day, N. P. J.; De Luca, M.; Dokova, K.; Dramowski, A.; Dunachie, S. J.; Eckmanns, T.; Eibach, D.; Emami, A.; Feasey, N.; Fisher-Pearson, N.; Forrest, K.; Garrett, D.; Gastmeier, P.; Giref, A. Z.; Greer, R. C.; Gupta, V.; Haller, S.; Haselbeck, A.; Hay, S. I.; Holm, M.; Hopkins, S.; Iregbu, K. C.; Jacobs, J.; Jarovsky, D.; Javanmardi, F.; Khorana, M.; Kissoon, N.; Kobeissi, E.; Kostyanev, T.; Krapp, F.; Krumkamp, R.; Kumar, A.; Kyu, H. H.; Lim, C.; Limmathurotsakul, D.; Loftus, M. J.; Lunn, M.; Ma, J.; Mturi, N.; Munera-Huertas, T.; Musicha, P.; Mussi-Pinhata, M. M.; Nakamura, T.; Nanavati, R.; Nangia, S.; Newton, P.; Ngoun, C.; Novotney, A.; Nwakanma, D.; Obiero, C. W.; Olivas-Martinez, A.; Olliaro, P.; Ooko, E.; Ortiz-Brizuela, E.; Peleg, A. Y.; Perrone, C.; Plakkal, N.; Ponce-De-Leon, A.; Raad, M.; Ramdin, T.; Riddell, A.; Roberts, T.; Robotham, J. V.; Roca, A.; Rudd, K. E.; Russell, N.; Schnall, J.; Scott, J. A. G.; Shivamallappa, M.; Sifuentes-Osornio, J.; Steenkeste, N.; Stewardson, A. J.; Stoeva, T.; Tasak, N.; Thaiprakong, A.; Thwaites, G.; Turner, C.; Turner, P.; Van Doorn, H. R.; Velaphi, S.; Vongpradith, A.; Vu, H.; Walsh, T.; Waner, S.; Wangrangsimakul, T.; Wozniak, T.; Zheng, P.; Sartorius, B.; Lopez, A. D.; Stergachis, A.; Moore, C.; Dolecek, C.; Naghavi, M., Global burden of bacterial antimicrobial resistance in 2019: a systematic analysis. *The Lancet* **2022,** *399* (10325), 629-655.

9. ONeill, J., Tackling drug-resistant infections globally: final report and recommendations. London: Review on Antimicrobial Resistance. In *Review on Antimicrobial resistance*, Health, D. o., Ed. 2016.
10. Willyard, C., The drug-resistant bacteria that pose the greatest health threats. *Nature* **2017,** *543* (7643), 15.
11. Poudel, A. N.; Zhu, S.; Cooper, N.; Little, P.; Tarrant, C.; Hickman, M.; Yao, G., The economic burden of antibiotic resistance: A systematic review and meta-analysis. *PLoS One* **2023,** *18* (5), e0285170.
12. Gupta, A.; Mumtaz, S.; Li, C.-H.; Hussain, I.; Rotello, V. M., Combatting antibiotic-resistant bacteria using nanomaterials. *Chemical Society Reviews* **2019,** *48* (2), 415-427.
13. Jackman, J. A.; Yoon, B. K.; Li, D.; Cho, N. J., Nanotechnology Formulations for Antibacterial Free Fatty Acids and Monoglycerides. *Molecules (Basel, Switzerland)* **2016,** *21* (3), 305.
14. Aruguete, D. M.; Kim, B.; Hochella, M. F., Jr.; Ma, Y.; Cheng, Y.; Hoegh, A.; Liu, J.; Pruden, A., Antimicrobial nanotechnology: its potential for the effective management of microbial drug resistance and implications for research needs in microbial nanotoxicology. *Environmental science. Processes & impacts* **2013,** *15* (1), 93-102.
15. Anderson, R.; Groundwater, P. W.; Todd, A.; Worsley, A., *Antibacterial agents: chemistry, mode of action, mechanisms of resistance and clinical applications*. John Wiley & Sons: 2012.
16. Berendonk, T. U.; Manaia, C. M.; Merlin, C.; Fatta-Kassinos, D.; Cytryn, E.; Walsh, F.; Bürgmann, H.; Sørum, H.; Norström, M.; Pons, M. N.; Kreuzinger, N.; Huovinen, P.; Stefani, S.; Schwartz, T.; Kisand, V.; Baquero, F.; Martinez, J. L., Tackling antibiotic resistance: the environmental framework. *Nature reviews. Microbiology* **2015,** *13* (5), 310-7.
17. Sorinolu, A. J.; Tyagi, N.; Kumar, A.; Munir, M., Antibiotic resistance development and human health risks during wastewater reuse and biosolids application in agriculture. *Chemosphere* **2021,** *265*, 129032.
18. Levy, S. B.; Marshall, B., Antibacterial resistance worldwide: causes, challenges and responses. *Nature medicine* **2004,** *10* (12 Suppl), S122-9.
19. Naylor, N. R.; Atun, R.; Zhu, N.; Kulasabanathan, K.; Silva, S.; Chatterjee, A.; Knight, G. M.; Robotham, J. V., Estimating the burden of antimicrobial resistance: a systematic literature review. *Antimicrobial Resistance & Infection Control* **2018,** *7* (1).
20. Godoy-Gallardo, M.; Eckhard, U.; Delgado, L. M.; de Roo Puente, Y. J. D.; Hoyos-Nogués, M.; Gil, F. J.; Perez, R. A., Antibacterial approaches in tissue engineering using metal ions and nanoparticles: From mechanisms to applications. *Bioactive Materials* **2021,** *6* (12), 4470-4490.
21. O'Connell, K. M.; Hodgkinson, J. T.; Sore, H. F.; Welch, M.; Salmond, G. P.; Spring, D. R. J. A. C. I. E., Combating multidrug-resistant bacteria: current strategies for the discovery of novel antibacterials. **2013,** *52* (41), 10706-10733.
22. Wang, S.; Gao, Y.; Jin, Q.; Ji, J., Emerging antibacterial nanomedicine for enhanced antibiotic therapy. *Biomaterials Science* **2020,** *8* (24), 6825-6839.
23. Qiao, Y.; He, J.; Chen, W. Y.; Yu, Y. H.; Li, W. L.; Du, Z.; Xie, T. T.; Ye, Y.; Hua, S. Y.; Zhong, D. N.; Yao, K.; Zhou, M., Light-Activatable Synergistic Therapy of Drug-Resistant Bacteria-Infected Cutaneous Chronic Wounds and Nonhealing Keratitis by Cupriferous Hollow Nanoshells. *Acs Nano* **2020,** *14* (3), 3299-3315.

24. Neethu, S.; Midhun, S. J.; Radhakrishnan, E. K.; Jyothis, M., Surface functionalization of central venous catheter with mycofabricated silver nanoparticles and its antibiofilm activity on multidrug resistant Acinetobacter baumannii. *Microbial Pathogenesis* **2020,** *138*.
25. Richards, S.-J.; Isufi, K.; Wilkins, L. E.; Lipecki, J.; Fullam, E.; Gibson, M. I. J. B., Multivalent antimicrobial polymer nanoparticles target mycobacteria and gram-negative bacteria by distinct mechanisms. **2018,** *19* (1), 256-264.
26. Cepas, V.; López, Y.; Muñoz, E.; Rolo, D.; Ardanuy, C.; Martí, S.; Xercavins, M.; Horcajada, J. P.; Bosch, J.; Soto, S. M., Relationship Between Biofilm Formation and Antimicrobial Resistance in Gram-Negative Bacteria. *Microbial Drug Resistance* **2019,** *25* (1), 72-79.
27. Lewis, K., Multidrug Tolerance of Biofilms and Persister Cells. Springer Berlin Heidelberg: 2008; pp 107-131.
28. Vert, M.; Doi, Y.; Hellwich, K.-H.; Hess, M.; Hodge, P.; Kubisa, P.; Rinaudo, M.; Schué, F., Terminology for biorelated polymers and applications (IUPAC Recommendations 2012) %J Pure and Applied Chemistry. **2012,** *84* (2), 377-410.
29. Davies, D., Understanding biofilm resistance to antibacterial agents. *Nature Reviews Drug Discovery* **2003,** *2* (2), 114-122.
30. Fulaz, S.; Vitale, S.; Quinn, L.; Casey, E., Nanoparticle–Biofilm Interactions: The Role of the EPS Matrix. *Trends in Microbiology* **2019,** *27* (11), 915-926.
31. Flemming, H.-C.; Wingender, J., The biofilm matrix. *Nature Reviews Microbiology* **2010,** *8* (9), 623-633.
32. Hou, J.; Veeregowda, D. H.; Belt-Gritter, B. v. d.; Busscher, H. J.; Mei, H. C. v. d.; McBain, A. J., Extracellular Polymeric Matrix Production and Relaxation under Fluid Shear and Mechanical Pressure in Staphylococcus aureus Biofilms. **2018,** *84* (1), e01516-17.
33. Srivastava, S.; Bhargava, A., Biofilms and human health. *Biotechnology Letters* **2016,** *38* (1), 1-22.
34. Pinto, R. M.; Soares, F. A.; Reis, S.; Nunes, C.; Van Dijck, P., Innovative Strategies Toward the Disassembly of the EPS Matrix in Bacterial Biofilms. *Frontiers in microbiology* **2020,** *11*, 952-952.
35. Lewis, K., Persister cells, dormancy and infectious disease. *Nature Reviews Microbiology* **2007,** *5* (1), 48-56.
36. Uruén, C.; Chopo-Escuin, G.; Tommassen, J.; Mainar-Jaime, R. C.; Arenas, J., Biofilms as Promoters of Bacterial Antibiotic Resistance and Tolerance. *Antibiotics* **2020,** *10* (1), 3.
37. Moan, J.; Peng, Q., An outline of the hundred-year history of PDT. *Anticancer Res* **2003,** *23* (5a), 3591-600.
38. Malik, Z., Photodynamic inactivation of antibiotic-resistant Gram-positive bacteria: Challenges and opportunities. *Translational Biophotonics* **2020,** *2* (1-2).
39. Malik, Z.; Ladan, H.; Nitzan, Y., Photodynamic inactivation of Gram-negative bacteria: problems and possible solutions. *J Photochem Photobiol B* **1992,** *14* (3), 262-6.
40. Jaber Ghorbani, D. R., Shahin Aghamiri, Alireza Teymouri, and Abbas Bahador, Photosensitizers in antibacterial photodynamic therapy: an overview. *LASER THERAPY* **2018,** *27* (4), 293-302.
41. Alves, E.; Faustino, M. A. F.; Neves, M. G. P. M. S.; Cunha, Â.; Nadais, H.; Almeida, A., Potential applications of porphyrins in photodynamic inactivation beyond the medical scope. *Journal of Photochemistry and Photobiology C: Photochemistry Reviews* **2015,** *22*, 34-57.

42. Warrier, A.; Mazumder, N.; Prabhu, S.; Satyamoorthy, K.; Murali, T. S., Photodynamic therapy to control microbial biofilms. *Photodiagnosis and Photodynamic Therapy* **2021,** *33*, 102090.
43. Vatansever, F.; De Melo, W. C. M. A.; Avci, P.; Vecchio, D.; Sadasivam, M.; Gupta, A.; Chandran, R.; Karimi, M.; Parizotto, N. A.; Yin, R.; Tegos, G. P.; Hamblin, M. R., Antimicrobial strategies centered around reactive oxygen species – bactericidal antibiotics, photodynamic therapy, and beyond. *FEMS Microbiology Reviews* **2013,** *37* (6), 955-989.
44. Hamblin, M. R., Antimicrobial photodynamic inactivation: a bright new technique to kill resistant microbes. *Current Opinion in Microbiology* **2016,** *33*, 67-73.
45. Kashef, N.; Huang, Y.-Y.; Hamblin, M. R., Advances in antimicrobial photodynamic inactivation at the nanoscale. **2017,** *6* (5), 853-879.
46. Hurst, A. N.; Scarbrough, B.; Saleh, R.; Hovey, J.; Ari, F.; Goyal, S.; Chi, R. J.; Troutman, J. M.; Vivero-Escoto, J. L., Influence of Cationic meso-Substituted Porphyrins on the Antimicrobial Photodynamic Efficacy and Cell Membrane Interaction in Escherichia coli. *International Journal of Molecular Sciences* **2019,** *20* (1).
47. Beirão, S.; Fernandes, S.; Coelho, J.; Faustino, M. A. F.; Tomé, J. P. C.; Neves, M. G. P. M. S.; Tomé, A. C.; Almeida, A.; Cunha, A., Photodynamic Inactivation of Bacterial and Yeast Biofilms With a Cationic Porphyrin. *Photochemistry and Photobiology* **2014,** *90* (6), 1387-1396.
48. Morley, S.; Griffiths, J.; Philips, G.; Moseley, H.; O'Grady, C.; Mellish, K.; Lankester, C. L.; Faris, B.; Young, R. J.; Brown, S. B.; Rhodes, L. E., Phase IIa randomized, placebo-controlled study of antimicrobial photodynamic therapy in bacterially colonized, chronic leg ulcers and diabetic foot ulcers: a new approach to antimicrobial therapy. *British Journal of Dermatology* **2013,** *168* (3), 617-624.
49. Pucelik, B.; Dąbrowski, J. M., Chapter Three - Photodynamic inactivation (PDI) as a promising alternative to current pharmaceuticals for the treatment of resistant microorganisms. In *Advances in Inorganic Chemistry*, van Eldik, R.; Hubbard, C. D., Eds. Academic Press: 2022; Vol. 79, pp 65-108.
50. Mei, L.; Zhu, S.; Liu, Y.; Yin, W.; Gu, Z.; Zhao, Y., An overview of the use of nanozymes in antibacterial applications. *Chemical Engineering Journal* **2021,** *418*, 129431.
51. Wyszogrodzka, G.; Marszałek, B.; Gil, B.; Dorożyński, P., Metal-organic frameworks: mechanisms of antibacterial action and potential applications. *Drug Discovery Today* **2016,** *21* (6), 1009-1018.
52. Slavin, Y. N.; Asnis, J.; Häfeli, U. O.; Bach, H., Metal nanoparticles: understanding the mechanisms behind antibacterial activity. *Journal of Nanobiotechnology* **2017,** *15* (1).
53. Wang, L.; Hu, C.; Shao, L., The antimicrobial activity of nanoparticles: present situation and prospects for the future. *International Journal of Nanomedicine* **2017,** *Volume 12*, 1227-1249.
54. Bruna, T.; Maldonado-Bravo, F.; Jara, P.; Caro, N., Silver Nanoparticles and Their Antibacterial Applications. *International Journal of Molecular Sciences* **2021,** *22* (13), 7202.
55. Rolband, L.; Godakhindi, V.; Vivero-Escoto, J. L.; Afonin, K. A., Demonstrating the Synthesis and Antibacterial Properties of Nanostructured Silver. *J Chem Educ* **2023,** *100* (9), 3547-3555.
56. Iravani, S.; Korbekandi, H.; Mirmohammadi, S. V.; Zolfaghari, B., Synthesis of silver nanoparticles: chemical, physical and biological methods. *Res Pharm Sci* **2014,** *9* (6), 385-406.

57. Das, C. G. A.; Kumar, V. G.; Dhas, T. S.; Karthick, V.; Govindaraju, K.; Joselin, J. M.; Baalamurugan, J., Antibacterial activity of silver nanoparticles (biosynthesis): A short review on recent advances. *Biocatalysis and Agricultural Biotechnology* **2020,** *27*.
58. Rai, M. K.; Deshmukh, S. D.; Ingle, A. P.; Gade, A. K., Silver nanoparticles: the powerful nanoweapon against multidrug-resistant bacteria. *Journal of Applied Microbiology* **2012,** *112* (5), 841-852.
59. Franci, G.; Falanga, A.; Galdiero, S.; Palomba, L.; Rai, M.; Morelli, G.; Galdiero, M., Silver nanoparticles as potential antibacterial agents. *Molecules* **2015,** *20* (5), 8856-74.
60. Flores-Lopez, L. Z.; Espinoza-Gomez, H.; Somanathan, R., Silver nanoparticles: Electron transfer, reactive oxygen species, oxidative stress, beneficial and toxicological effects. Mini review. *Journal of Applied Toxicology* **2019,** *39* (1), 16-26.
61. Osonga, F. J.; Akgul, A.; Yazgan, I.; Akgul, A.; Eshun, G. B.; Sakhaee, L.; Sadik, O. A., Size and Shape-Dependent Antimicrobial Activities of Silver and Gold Nanoparticles: A Model Study as Potential Fungicides. *Molecules* **2020,** *25* (11), 2682.
62. Pareek, V.; Gupta, R.; Panwar, J., Do physico-chemical properties of silver nanoparticles decide their interaction with biological media and bactericidal action? A review. *Mater Sci Eng C Mater Biol Appl* **2018,** *90*, 739-749.
63. Menichetti, A.; Mavridi-Printezi, A.; Mordini, D.; Montalti, M., Effect of Size, Shape and Surface Functionalization on the Antibacterial Activity of Silver Nanoparticles. *Journal of Functional Biomaterials* **2023,** *14* (5), 244.
64. Pal, S.; Tak, Y. K.; Song, J. M., Does the antibacterial activity of silver nanoparticles depend on the shape of the nanoparticle? A study of the Gram-negative bacterium Escherichia coli. *Appl Environ Microbiol* **2007,** *73* (6), 1712-20.
65. Stabryla, L. M.; Moncure, P. J.; Millstone, J. E.; Gilbertson, L. M., Particle-Driven Effects at the Bacteria Interface: A Nanosilver Investigation of Particle Shape and Dose Metric. *ACS Applied Materials & Interfaces* **2023,** *15* (33), 39027-39038.
66. Raza, M. A.; Kanwal, Z.; Rauf, A.; Sabri, A. N.; Riaz, S.; Naseem, S. Size- and Shape-Dependent Antibacterial Studies of Silver Nanoparticles Synthesized by Wet Chemical Routes *Nanomaterials* [Online], 2016.
67. Cheon, J. Y.; Kim, S. J.; Rhee, Y. H.; Kwon, O. H.; Park, W. H., Shape-dependent antimicrobial activities of silver nanoparticles. *International Journal of Nanomedicine* **2019,** *Volume 14*, 2773-2780.
68. Vazquez-Muñoz, R.; Bogdanchikova, N.; Huerta-Saquero, A., Beyond the Nanomaterials Approach: Influence of Culture Conditions on the Stability and Antimicrobial Activity of Silver Nanoparticles. *ACS Omega* **2020,** *5* (44), 28441-28451.
69. Bélteky, P.; Rónavári, A.; Igaz, N.; Szerencsés, B.; Tóth, I. Y.; Pfeiffer, I.; Kiricsi, M.; Kónya, Z., Silver nanoparticles: aggregation behavior in biorelevant conditions and its impact on biological activity. *International Journal of Nanomedicine* **2019,** *14* (null), 667-687.
70. Gunawan, C.; Marquis, C. P.; Amal, R.; Sotiriou, G. A.; Rice, S. A.; Harry, E. J., Widespread and Indiscriminate Nanosilver Use: Genuine Potential for Microbial Resistance. *ACS Nano* **2017,** *11* (4), 3438-3445.
71. Silver, S., Bacterial silver resistance: molecular biology and uses and misuses of silver compounds. *FEMS Microbiol Rev* **2003,** *27* (2-3), 341-53.
72. Panáček, A.; Kvítek, L.; Smékalová, M.; Večeřová, R.; Kolář, M.; Röderová, M.; Dyčka, F.; Šebela, M.; Prucek, R.; Tomanec, O.; Zbořil, R., Bacterial resistance to silver nanoparticles and how to overcome it. *Nature Nanotechnology* **2018,** *13* (1), 65-71.

73. Stabryla, L. M.; Johnston, K. A.; Diemler, N. A.; Cooper, V. S.; Millstone, J. E.; Haig, S.-J.; Gilbertson, L. M., Role of bacterial motility in differential resistance mechanisms of silver nanoparticles and silver ions. *Nature Nanotechnology* **2021,** *16* (9), 996-1003.
74. Wu, K.; Li, H.; Cui, X.; Feng, R.; Chen, W.; Jiang, Y.; Tang, C.; Wang, Y.; Wang, Y.; Shen, X.; Liu, Y.; Lynch, M.; Long, H., Mutagenesis and Resistance Development of Bacteria Challenged by Silver Nanoparticles. *Antimicrobial Agents and Chemotherapy* **2022,** *66* (10), e00628-22.
75. Silver, S.; Phung, L. T.; Silver, G., Silver as biocides in burn and wound dressings and bacterial resistance to silver compounds. *Journal of Industrial Microbiology & Biotechnology* **2006,** *33* (7), 627-634.
76. Hou, X.; Yang, L.; Liu, J.; Zhang, Y.; Chu, L.; Ren, C.; Huang, F.; Liu, J., Silver-decorated, light-activatable polymeric antimicrobials for combined chemo-photodynamic therapy of drug-resistant bacterial infection. *Biomater Sci* **2020,** *8* (22), 6350-6361.
77. Sun, P.; Ye, L.; Tan, X.; Peng, J.; Zhao, L.; Zhou, Y., Silver Nanoparticle-Assisted Photodynamic Therapy for Biofilm Eradication. *ACS Applied Nano Materials* **2022**.
78. Bourgonje, C. R.; da Silva, D. R. C.; McIlroy, E.; Calvert, N. D.; Shuhendler, A. J.; Scaiano, J. C., Silver nanoparticles with exceptional near-infrared absorbance for photoenhanced antimicrobial applications. *Journal of Materials Chemistry B* **2023,** *11* (26), 6114-6122.
79. Gamage McEvoy, J.; Zhang, Z., Antimicrobial and photocatalytic disinfection mechanisms in silver-modified photocatalysts under dark and light conditions. *Journal of Photochemistry and Photobiology C: Photochemistry Reviews* **2014,** *19*, 62-75.
80. Mao, B. H.; Chen, Z. Y.; Wang, Y. J.; Yan, S. J., Silver nanoparticles have lethal and sublethal adverse effects on development and longevity by inducing ROS-mediated stress responses. *Scientific Reports* **2018,** *8*.
81. Mota, D. R.; Lima, G. A. S.; Oliveira, H. P. M.; Pellosi, D. S., Pluronic-loaded Silver Nanoparticles/Photosensitizers Nanohybrids: Influence of the Polymer Chain Length on Metal-enhanced Photophysical Properties. *Photochemistry and Photobiology* **2022,** *98* (1), 175-183.
82. Barooah, N.; Bhasikuttan, A. C.; Sudarsan, V.; Choudhury, S. D.; Pal, H.; Mohanty, J., Surface functionalized silver nanoparticle conjugates: demonstration of uptake and release of a phototherapeutic porphyrin dye. *Chemical Communications* **2011,** *47* (32), 9182.
83. Mahajan, P. G.; Dige, N. C.; Vanjare, B. D.; Eo, S.-H.; Seo, S.-Y.; Kim, S. J.; Hong, S.-K.; Choi, C.-S.; Lee, K. H., A potential mediator for photodynamic therapy based on silver nanoparticles functionalized with porphyrin. *Journal of Photochemistry and Photobiology A: Chemistry* **2019,** *377*, 26-35.
84. Lismont, M.; Dreesen, L.; Heinrichs, B.; Paez, C. A., Protoporphyrin IX-Functionalized AgSiO2 Core-Shell Nanoparticles: Plasmonic Enhancement of Fluorescence and Singlet Oxygen Production. *Photochemistry and Photobiology* **2016,** *92* (2), 247-256.
85. Masilela, N.; Nyokong, T., The interaction of silver nanoparticles with low symmetry cysteinyl metallophthalocyanines and their antimicrobial effect. *Journal of Photochemistry and Photobiology A: Chemistry* **2013,** *255*, 1-9.
86. Elashnikov, R.; Radocha, M.; Panov, I.; Rimpelova, S.; Ulbrich, P.; Michalcova, A.; Svorcik, V.; Lyutakov, O., Porphyrin-silver nanoparticles hybrids: Synthesis, characterization and antibacterial activity. *Materials Science and Engineering: C* **2019,** *102*, 192-199.
87. Silva, M. M.; Mota, D. R.; Silva, C. B.; De Oliveira, H. P. M.; Pellosi, D. S., Synthesis of Pluronic-based silver nanoparticles/methylene blue nanohybrids: Influence of the metal shape on photophysical properties. *Materials Science and Engineering: C* **2020,** *114*, 110987.

88. Pellosi, D. S.; De Jesus, P. d. C. C.; Tedesco, A. C., Spotlight on the delivery of photosensitizers: different approaches for photodynamic-based therapies. *Expert Opinion on Drug Delivery* **2017,** *14* (12), 1395-1406.
89. Hu, B.; Cao, X.; Nahan, K.; Caruso, J.; Tang, H.; Zhang, P., Surface plasmon-photosensitizer resonance coupling: an enhanced singlet oxygen production platform for broad-spectrum photodynamic inactivation of bacteria. *Journal of Materials Chemistry B* **2014,** *2* (40), 7073-7081.
90. Wang, P.; Tang, H.; Zhang, P., Plasmonic Nanoparticle-based Hybrid Photosensitizers with Broadened Excitation Profile for Photodynamic Therapy of Cancer Cells. *Scientific Reports* **2016,** *6* (1), 34981.
91. Murphy, S.; Huang, L. B.; Kamat, P. V., Charge-Transfer Complexation and Excited-State Interactions in Porphyrin-Silver Nanoparticle Hybrid Structures. *Journal of Physical Chemistry C* **2011,** *115* (46), 22761-22769.
92. Xu, Z.; Zhang, C.; Wang, X.; Liu, D., Release Strategies of Silver Ions from Materials for Bacterial Killing. *ACS Applied Bio Materials* **2021,** *4* (5), 3985-3999.
93. Xu, Z.; Zhang, C.; Yu, Y.; Li, W.; Ma, Z.; Wang, J.; Zhang, X.; Gao, H.; Liu, D., Photoactive Silver Nanoagents for Backgroundless Monitoring and Precision Killing of Multidrug-Resistant Bacteria. *Nanotheranostics* **2021,** *5* (4), 472-487.
94. Sorinolu, A. J.; Godakhindi, V.; Siano, P.; Vivero-Escoto, J. L.; Munir, M., Influence of silver ion release on the inactivation of antibiotic resistant bacteria using light-activated silver nanoparticles. *Materials Advances* **2022,** *3* (24), 9090-9102.
95. Chen, J.; Yang, L.; Chen, J.; Liu, W.; Zhang, D.; Xu, P.; Dai, T.; Shang, L.; Yang, Y.; Tang, S.; Zhang, Y.; Lin, H.; Chen, Z.; Huang, M., Composite of silver nanoparticles and photosensitizer leads to mutual enhancement of antimicrobial efficacy and promotes wound healing. *Chemical Engineering Journal* **2019,** *374*, 1373-1381.
96. Malá, Z.; Žárská, L.; Bajgar, R.; Bogdanová, K.; Kolář, M.; Panáček, A.; Binder, S.; Kolářová, H., The application of antimicrobial photodynamic inactivation on methicillin-resistant S. aureus and ESBL-producing K. pneumoniae using porphyrin photosensitizer in combination with silver nanoparticles. *Photodiagnosis and Photodynamic Therapy* **2021,** *33*, 102140.
97. Nakonieczna, J.; Rapacka-Zdonczyk, A.; Kawiak, A.; Bielawski, K. P.; Grinholc, M., Sub-lethal photodynamic inactivation renders Staphylococcus aureus susceptible to silver nanoparticles. *Photochemical & Photobiological Sciences* **2013,** *12* (9), 1622-1627.
98. Li, R.; Chen, J.; Cesario, T. C.; Wang, X.; Yuan, J. S.; Rentzepis, P. M., Synergistic reaction of silver nitrate, silver nanoparticles, and methylene blue against bacteria. **2016,** *113* (48), 13612-13617.
99. Elashnikov, R.; Lyutakov, O.; Ulbrich, P.; Svorcik, V., Light-activated polymethylmethacrylate nanofibers with antibacterial activity. *Materials Science and Engineering: C* **2016,** *64*, 229-235.
100. Lyutakov, O.; Hejna, O.; Solovyev, A.; Kalachyova, Y.; Svorcik, V., Polymethylmethacrylate doped with porphyrin and silver nanoparticles as light-activated antimicrobial material. *Rsc Advances* **2014,** *4* (92), 50624-50630.
101. Ahmadov, T. O.; Ding, R.; Zhang, J.; Wang, P.; Tang, H.; Zhang, P., Silver nanoparticle-enhanced hybrid photosensitizer for photoinactivation of multidrug-resistant Staphylococcus aureus (MRSA). *RSC Advances* **2016,** *6* (59), 54318-54321.

102. Wijesiri, N.; Yu, Z.; Tang, H.; Zhang, P., Antifungal photodynamic inactivation against dermatophyte Trichophyton rubrum using nanoparticle-based hybrid photosensitizers. *Photodiagnosis Photodyn Ther* **2018,** *23*, 202-208.
103. Kuthati, Y.; Kankala, R. K.; Busa, P.; Lin, S.-X.; Deng, J.-P.; Mou, C.-Y.; Lee, C.-H., Phototherapeutic spectrum expansion through synergistic effect of mesoporous silica trio-nanohybrids against antibiotic-resistant gram-negative bacterium. *Journal of Photochemistry and Photobiology B: Biology* **2017,** *169*, 124-133.
104. Zhang, K.; Li, X.; Yu, C.; Wang, Y., Promising Therapeutic Strategies Against Microbial Biofilm Challenges. **2020,** *10*.
105. Dai, X.; Chen, X.; Zhao, J.; Zhao, Y.; Guo, Q.; Zhang, T.; Chu, C.; Zhang, X.; Li, C., Structure–Activity Relationship of Membrane-Targeting Cationic Ligands on a Silver Nanoparticle Surface in an Antibiotic-Resistant Antibacterial and Antibiofilm Activity Assay. *ACS Applied Materials & Interfaces* **2017,** *9* (16), 13837-13848.
106. Guo, J.; Qin, S.; Wei, Y.; Liu, S.; Peng, H.; Li, Q.; Luo, L.; Lv, M., Silver nanoparticles exert concentration-dependent influences on biofilm development and architecture. *Cell Proliferation* **2019,** *52* (4).
107. Martinez-Gutierrez, F.; Boegli, L.; Agostinho, A.; Sánchez, E. M.; Bach, H.; Ruiz, F.; James, G., Anti-biofilm activity of silver nanoparticles against different microorganisms. *Biofouling* **2013,** *29* (6), 651-660.
108. Sonawnae, A.; Jena; Mohanty; Mallick; Jacob, Toxicity and antibacterial assessment of chitosan-coated silver nanoparticles on human pathogens and macrophage cells. *International Journal of Nanomedicine* **2012**, 1805.
109. Goswami, S. R.; Sahareen, T.; Singh, M.; Kumar, S., Role of biogenic silver nanoparticles in disruption of cell–cell adhesion in Staphylococcus aureus and Escherichia coli biofilm. *Journal of Industrial and Engineering Chemistry* **2015,** *26*, 73-80.
110. Misba, L.; Kulshrestha, S.; Khan, A. U., Antibiofilm action of a toluidine blue O-silver nanoparticle conjugate onStreptococcus mutans: a mechanism of type I photodynamic therapy. *Biofouling* **2016,** *32* (3), 313-328.
111. Aydın, H.; Er, K.; Kuştarcı, A.; Akarsu, M.; Gençer, G.; Er, H.; Felek, R., Antibacterial activity of silver nanoparticles activated by photodynamic therapy in infected root canals. *Dental and Medical Problems* **2020,** *57* (4), 393-400.
112. Fletcher, P.; Deluiz, D.; Tinoco, E. M. B.; Ricci, J. L.; Tarnow, D. P.; Tinoco, J. M., Human Histologic Evidence of Reosseointegration Around an Implant Affected with Peri-implantitis Following Decontamination with Sterile Saline and Antiseptics: A Case History Report. *International Journal of Periodontics & Restorative Dentistry* **2017,** *37* (4), 499-508.
113. Parasuraman, P.; R. Y, T.; Shaji, C.; Sharan, A.; Bahkali, A. H.; Al-Harthi, H. F.; Syed, A.; Anju, V. T.; Dyavaiah, M.; Siddhardha, B., Biogenic Silver Nanoparticles Decorated with Methylene Blue Potentiated the Photodynamic Inactivation of Pseudomonas aeruginosa and Staphylococcus aureus. *Pharmaceutics* **2020,** *12* (8), 709.
114. Ghasemi, M.; Khorsandi, K.; Kianmehr, Z., Photodynamic inactivation with curcumin and silver nanoparticles hinders Pseudomonas aeruginosa planktonic and biofilm formation: evaluation of glutathione peroxidase activity and ROS production. *World Journal of Microbiology and Biotechnology* **2021,** *37* (9).
115. Kassab, A.; Dabous, O.; Morsy, M., A novel management of streptococcal pharyngotonsillar infections by laser-activated silver nanoparticles and methylene blue

conjugate, in vitro study. *International Journal of Pediatric Otorhinolaryngology* **2017,** *100*, 114-118.
116. Shabangu, S. M.; Babu, B.; Soy, R. C.; Oyim, J.; Amuhaya, E.; Nyokong, T., Susceptibility of Staphylococcus aureus to porphyrin-silver nanoparticle mediated photodynamic antimicrobial chemotherapy. *Journal of Luminescence* **2020,** *222*.
117. Mamun, M. M.; Sorinolu, A. J.; Munir, M.; Vejerano, E. P., Nanoantibiotics: Functions and Properties at the Nanoscale to Combat Antibiotic Resistance. **2021,** *9* (348).
118. Abed, N.; Saïd-Hassane, F.; Zouhiri, F.; Mougin, J.; Nicolas, V.; Desmaële, D.; Gref, R.; Couvreur, P., An efficient system for intracellular delivery of beta-lactam antibiotics to overcome bacterial resistance. *Scientific Reports* **2015,** *5* (1), 13500.
119. Gao, W.; Thamphiwatana, S.; Angsantikul, P.; Zhang, L. J. W. i. r. n.; nanobiotechnology, Nanoparticle approaches against bacterial infections. **2014,** *6* (6), 532-547.
120. Abdellatif, A. A.; Alturki, H. N.; Tawfeek, H. M. J. S. r., Different cellulosic polymers for synthesizing silver nanoparticles with antioxidant and antibacterial activities. **2021,** *11* (1), 1-18.
121. Cao, F.; Ju, E.; Zhang, Y.; Wang, Z.; Liu, C.; Li, W.; Huang, Y.; Dong, K.; Ren, J.; Qu, X. J. A. n., An efficient and benign antimicrobial depot based on silver-infused MoS2. **2017,** *11* (5), 4651-4659.
122. Mijnendonckx, K.; Leys, N.; Mahillon, J.; Silver, S.; Van Houdt, R. J. B., Antimicrobial silver: uses, toxicity and potential for resistance. **2013,** *26* (4), 609-621.
123. Yan, X.; He, B.; Liu, L.; Qu, G.; Shi, J.; Hu, L.; Jiang, G. J. M., Antibacterial mechanism of silver nanoparticles in Pseudomonas aeruginosa: proteomics approach. **2018,** *10* (4), 557-564.
124. Elashnikov, R.; Radocha, M.; Panov, I.; Rimpelova, S.; Ulbrich, P.; Michalcova, A.; Svorcik, V.; Lyutakov, O. J. M. S.; C, E., Porphyrin-silver nanoparticles hybrids: synthesis, characterization and antibacterial activity. **2019,** *102*, 192-199.
125. Salomoni, R.; Léo, P.; Montemor, A.; Rinaldi, B.; Rodrigues, M. J. N., science; applications, Antibacterial effect of silver nanoparticles in Pseudomonas aeruginosa. **2017,** *10*, 115.
126. Siriwardana, K.; Suwandaratne, N.; Perera, G. S.; Collier, W. E.; Perez, F.; Zhang, D. J. T. J. o. P. C. C., Contradictory dual effects: organothiols can induce both silver nanoparticle disintegration and formation under ambient conditions. **2015,** *119* (36), 20975-20984.
127. Ho, C. M.; Yau, S. K. W.; Lok, C. N.; So, M. H.; Che, C. M. J. C. A. A. J., Oxidative dissolution of silver nanoparticles by biologically relevant oxidants: a kinetic and mechanistic study. **2010,** *5* (2), 285-293.
128. Shabangu, S. M.; Babu, B.; Soy, R. C.; Oyim, J.; Amuhaya, E.; Nyokong, T. J. J. o. L., Susceptibility of Staphylococcus aureus to porphyrin-silver nanoparticle mediated photodynamic antimicrobial chemotherapy. **2020,** *222*, 117158.
129. Xie, X.; Mao, C.; Liu, X.; Zhang, Y.; Cui, Z.; Yang, X.; Yeung, K. W.; Pan, H.; Chu, P. K.; Wu, S. J. A. a. m.; interfaces, Synergistic bacteria killing through photodynamic and physical actions of graphene oxide/Ag/collagen coating. **2017,** *9* (31), 26417-26428.
130. Ghasemi, M.; Khorsandi, K.; Kianmehr, Z. J. W. J. o. M.; Biotechnology, Photodynamic inactivation with curcumin and silver nanoparticles hinders Pseudomonas aeruginosa planktonic and biofilm formation: evaluation of glutathione peroxidase activity and ROS production. **2021,** *37* (9), 1-10.

131. Malá, Z.; Žárská, L.; Bajgar, R.; Bogdanová, K.; Kolář, M.; Panáček, A.; Binder, S.; Kolářová, H. J. P.; Therapy, P., The application of antimicrobial photodynamic inactivation on methicillin-resistant S. aureus and ESBL-producing K. pneumoniae using porphyrin photosensitizer in combination with silver nanoparticles. **2021,** *33*, 102140.
132. Almeida, A.; Cunha, A.; Faustino, M.; Tomé, A.; Neves, M. J. P. i. o. m. p. m.; applications, e., Porphyrins as antimicrobial photosensitizing agents. **2011,** *11*, 83-160.
133. Vzorov, A. N.; Dixon, D. W.; Trommel, J. S.; Marzilli, L. G.; Compans, R. W. J. A. a.; chemotherapy, Inactivation of human immunodeficiency virus type 1 by porphyrins. **2002,** *46* (12), 3917-3925.
134. Reisner, B. S.; Woods, G. L. J. J. o. c. m., Times to detection of bacteria and yeasts in BACTEC 9240 blood culture bottles. **1999,** *37* (6), 2024-2026.
135. Bastus, N. G.; Merkoci, F.; Piella, J.; Puntes, V., Synthesis of Highly Monodisperse Citrate-Stabilized Silver Nanoparticles of up to 200 nm: Kinetic Control and Catalytic Properties. *Chemistry of Materials* **2014,** *26* (9), 2836-2846.
136. Brittle, S. W.; Baker, J. D.; Dorney, K. M.; Dagher, J. M.; Ebrahimian, T.; Higgins, S. R.; Pavel Sizemore, I. E., Measuring the Silver Composition of Nanocolloids by Inductively Coupled Plasma–Optical Emission Spectroscopy: A Laboratory Experiment for Chemistry and Engineering Students. *Journal of Chemical Education* **2015,** *92* (6), 1061-1065.
137. Mays, C.; Garza, G. L.; Waite-Cusic, J.; Radniecki, T. S.; Navab-Daneshmand, T. J. W. r. X., Impact of biosolids amendment and wastewater effluent irrigation on enteric antibiotic-resistant bacteria–a greenhouse study. **2021,** *13*, 100119.
138. Weinstein, M. P.; Limbago, B.; Patel, J.; Mathers, A.; Campeau, S.; Mazzulli, T.; Eliopoulos, G.; Patel, R.; Galas, M.; Richter, S. J. W., PA: Clinical; Institute, L. S., M100 performance standards for antimicrobial susceptibility testing. **2018**.
139. Hurst, A. N.; Scarbrough, B.; Saleh, R.; Hovey, J.; Ari, F.; Goyal, S.; Chi, R. J.; Troutman, J. M.; Vivero-Escoto, J. L., Influence of Cationic meso-Substituted Porphyrins on the Antimicrobial Photodynamic Efficacy and Cell Membrane Interaction in Escherichia coli. *International journal of molecular sciences* **2019,** *20* (1).
140. Juneja, R.; Lyles, Z.; Vadarevu, H.; Afonin, K. A.; Vivero-Escoto, J. L., Multimodal Polysilsesquioxane Nanoparticles for Combinatorial Therapy and Gene Delivery in Triple-Negative Breast Cancer. *ACS Applied Materials & Interfaces* **2019,** *11* (13), 12308-12320.
141. Vivero-Escoto, J. L.; Vega, D. L., Stimuli-responsive protoporphyrin IX silica-based nanoparticles for photodynamic therapy in vitro. *RSC Adv.* **2014,** *4* (28), 14400-14407.
142. Aktara, M. N.; Nayim, S.; Sahoo, N. K.; Hossain, M., The synthesis of thiol-stabilized silver nanoparticles and their application towards the nanomolar-level colorimetric recognition of glutathione. *New Journal of Chemistry* **2019,** *43* (34), 13480-13490.
143. Toh, H. S.; Batchelor-Mcauley, C.; Tschulik, K.; Compton, R. G., Chemical interactions between silver nanoparticles and thiols: a comparison of mercaptohexanol against cysteine. *Science China Chemistry* **2014,** *57* (9), 1199-1210.
144. Zhang, X.-F.; Liu, Z.-G.; Shen, W.; Gurunathan, S., Silver Nanoparticles: Synthesis, Characterization, Properties, Applications, and Therapeutic Approaches. *International Journal of Molecular Sciences* **2016,** *17* (9), 1534.
145. Siano, P.; Johnston, A.; Loman-Cortes, P.; Zhin, Z.; Vivero-Escoto, J. L., Evaluation of Polyhedral Oligomeric Silsesquioxane Porphyrin Derivatives on Photodynamic Therapy. *Molecules* **2020,** *25* (21).

146. Chen, J.; Yang, L.; Chen, J.; Liu, W.; Zhang, D.; Xu, P.; Dai, T.; Shang, L.; Yang, Y.; Tang, S. J. C. E. J., Composite of silver nanoparticles and photosensitizer leads to mutual enhancement of antimicrobial efficacy and promotes wound healing. **2019,** *374*, 1373-1381.
147. Yang, W.; Wang, C.; Arrighi, V., Effects of amine types on the properties of silver oxalate ink and the associated film morphology. *Journal of Materials Science: Materials in Electronics* **2018,** *29* (24), 20895-20906.
148. Das, K.; Roychoudhury, A., Reactive oxygen species (ROS) and response of antioxidants as ROS-scavengers during environmental stress in plants. **2014,** *2*.
149. Caires, C. S.; Farias, L. A.; Gomes, L. E.; Pinto, B. P.; Gonçalves, D. A.; Zagonel, L. F.; Nascimento, V. A.; Alves, D. C.; Colbeck, I.; Whitby, C. J. M. S.; C, E., Effective killing of bacteria under blue-light irradiation promoted by green synthesized silver nanoparticles loaded on reduced graphene oxide sheets. **2020,** *113*, 110984.
150. Kittler, S.; Greulich, C.; Diendorf, J.; Koller, M.; Epple, M. J. C. o. m., Toxicity of silver nanoparticles increases during storage because of slow dissolution under release of silver ions. **2010,** *22* (16), 4548-4554.
151. Le Ouay, B.; Stellacci, F. J. N. t., Antibacterial activity of silver nanoparticles: A surface science insight. **2015,** *10* (3), 339-354.
152. Loza, K.; Diendorf, J.; Sengstock, C.; Ruiz-Gonzalez, L.; Gonzalez-Calbet, J.; Vallet-Regi, M.; Köller, M.; Epple, M. J. J. o. M. C. B., The dissolution and biological effects of silver nanoparticles in biological media. **2014,** *2* (12), 1634-1643.
153. Zhang, W.; Yao, Y.; Li, K.; Huang, Y.; Chen, Y. J. E. P., Influence of dissolved oxygen on aggregation kinetics of citrate-coated silver nanoparticles. **2011,** *159* (12), 3757-3762.
154. Dougherty, T. J.; Gomer, C. J.; Henderson, B. W.; Jori, G.; Kessel, D.; Korbelik, M.; Moan, J.; Peng, Q., Photodynamic Therapy. *JNCI Journal of the National Cancer Institute* **1998,** *90* (12), 889-905.
155. Agostinis, P.; Berg, K.; Cengel, K. A.; Foster, T. H.; Girotti, A. W.; Gollnick, S. O.; Hahn, S. M.; Hamblin, M. R.; Juzeniene, A.; Kessel, D.; Korbelik, M.; Moan, J.; Mroz, P.; Nowis, D.; Piette, J.; Wilson, B. C.; Golab, J., Photodynamic therapy of cancer: An update. *CA: A Cancer Journal for Clinicians* **2011,** *61* (4), 250-281.
156. Wilkinson, F.; Helman, W. P.; Ross, A. B., Rate Constants for the Decay and Reactions of the Lowest Electronically Excited Singlet State of Molecular Oxygen in Solution. An Expanded and Revised Compilation. **1995,** *24*, 663-677.
157. Hatz, S.; Poulsen, L.; Ogilby, P. R., Time-resolved Singlet Oxygen Phosphorescence Measurements from Photosensitized Experiments in Single Cells: Effects of Oxygen Diffusion and Oxygen Concentration. *Photochemistry and Photobiology* **2008,** *84* (5), 1284-1290.
158. Klaper, M.; Fudickar, W.; Linker, T., Role of Distance in Singlet Oxygen Applications: A Model System. *Journal of the American Chemical Society* **2016,** *138* (22), 7024-7029.
159. Le Ouay, B.; Stellacci, F., Antibacterial activity of silver nanoparticles: A surface science insight. *Nano Today* **2015,** *10* (3), 339-354.
160. Yin, R.; Agrawal, T.; Khan, U.; Gupta, G. K.; Rai, V.; Huang, Y.-Y.; Hamblin, M. R. J. N., Antimicrobial photodynamic inactivation in nanomedicine: small light strides against bad bugs. **2015,** *10* (15), 2379-2404.
161. Laborda, F.; Jiménez-Lamana, J.; Bolea, E.; Castillo, J. R., Selective identification, characterization and determination of dissolved silver(i) and silver nanoparticles based on single particle detection by inductively coupled plasma mass spectrometry. *Journal of Analytical Atomic Spectrometry* **2011,** *26* (7), 1362.

162. Johnston, K. A.; Stabryla, L. M.; Smith, A. M.; Gan, X. Y.; Gilbertson, L. M.; Millstone, J. E., Impacts of broth chemistry on silver ion release, surface chemistry composition, and bacterial cytotoxicity of silver nanoparticles. *Environmental Science: Nano* **2018,** *5* (2), 304-312.
163. De Leersnyder, I.; De Gelder, L.; Van Driessche, I.; Vermeir, P., Influence of growth media components on the antibacterial effect of silver ions on Bacillus subtilis in a liquid growth medium. *Scientific Reports* **2018,** *8* (1).
164. Weese, J. S. J. I. j., Methicillin-resistant Staphylococcus aureus in animals. **2010,** *51* (3), 233-244.
165. Agnihotri, S.; Mukherji, S.; Mukherji, S., Size-controlled silver nanoparticles synthesized over the range 5–100 nm using the same protocol and their antibacterial efficacy. *RSC Advances* **2014,** *4* (8), 3974-3983.
166. Agarwal, A.; Gupta, S.; Sharma, R., Reactive oxygen species (ROS) measurement. In *Andrological evaluation of male infertility*, Springer: 2016; pp 155-163.
167. Phaniendra, A.; Jestadi, D. B.; Periyasamy, L. J. I. j. o. c. b., Free radicals: properties, sources, targets, and their implication in various diseases. **2015,** *30* (1), 11-26.
168. Merchat, M.; Bertolini, G.; Giacomini, P.; Villaneuva, A.; Jori, G. J. J. o. P.; Biology, P. B., Meso-substituted cationic porphyrins as efficient photosensitizers of gram-positive and gram-negative bacteria. **1996,** *32* (3), 153-157.
169. Martínez, J. L., Antibiotics and antibiotic resistance genes in natural environments. *Science (New York, N.Y.)* **2008,** *321* (5887), 365-7.
170. Hasan, N.; Cao, J.; Lee, J.; Hlaing, S. P.; Oshi, M. A.; Naeem, M.; Ki, M.-H.; Lee, B. L.; Jung, Y.; Yoo, J.-W. J. P., Bacteria-targeted clindamycin loaded polymeric nanoparticles: Effect of surface charge on nanoparticle adhesion to MRSA, antibacterial activity, and wound healing. **2019,** *11* (5), 236.
171. Nederberg, F.; Zhang, Y.; Tan, J. P.; Xu, K.; Wang, H.; Yang, C.; Gao, S.; Guo, X. D.; Fukushima, K.; Li, L. J. N. c., Biodegradable nanostructures with selective lysis of microbial membranes. **2011,** *3* (5), 409-414.
172. Zhang, X.-Z.; Zeng, X.; Sun, Y.-X.; Zhuo, R.-X. J. B. M. i. M., Bioactive materials in gene therapy. **2011**, 179-219.
173. Meng, F.; Kwon, S.; Wang, J.; Yeo, Y., Immunoactive drug carriers in cancer therapy. In *Biomaterials for Cancer Therapeutics*, Elsevier: 2020; pp 53-94.
174. Gomes, A. T.; Neves, M. G.; Cavaleiro, J. A. J. A. d. A. B. d. C., Cancer, photodynamic therapy and porphyrin-type derivatives. **2018,** *90*, 993-1026.
175. Granville, D. J.; McManus, B.; Hunt, D. J. H.; Histopathology, Photodynamic therapy: shedding light on the biochemical pathways regulating porphyrin-mediated cell death. **2001,** *16* (1), 309-317.
176. Alt, V.; Bechert, T.; Steinrücke, P.; Wagener, M.; Seidel, P.; Dingeldein, E.; Domann, E.; Schnettler, R. J. B., An in vitro assessment of the antibacterial properties and cytotoxicity of nanoparticulate silver bone cement. **2004,** *25* (18), 4383-4391.
177. Chakraborty, N.; Jha, D.; Roy, I.; Kumar, P.; Gaurav, S. S.; Marimuthu, K.; Ng, O.-T.; Lakshminarayanan, R.; Verma, N. K.; Gautam, H. K., Nanobiotics against antimicrobial resistance: harnessing the power of nanoscale materials and technologies. *Journal of Nanobiotechnology* **2022,** *20* (1).

178. Hajipour, M. J.; Fromm, K. M.; Ashkarran, A. A.; Jimenez de Aberasturi, D.; de Larramendi, I. R.; Rojo, T.; Serpooshan, V.; Parak, W. J.; Mahmoudi, M., Antibacterial properties of nanoparticles. *Trends Biotechnol* **2012,** *30* (10), 499-511.
179. Shkodenko, L.; Kassirov, I.; Koshel, E., Metal Oxide Nanoparticles Against Bacterial Biofilms: Perspectives and Limitations. *Microorganisms* **2020,** *8* (10), 1545.
180. Durán, N.; Silveira, C. P.; Durán, M.; Martinez, D. S. T., Silver nanoparticle protein corona and toxicity: a mini-review. *Journal of Nanobiotechnology* **2015,** *13* (1).
181. Argentiere, S.; Cella, C.; Cesaria, M.; Milani, P.; Lenardi, C., Silver nanoparticles in complex biological media: assessment of colloidal stability and protein corona formation. *Journal of Nanoparticle Research* **2016,** *18* (8).
182. Mohammad-Beigi, H.; Hayashi, Y.; Zeuthen, C. M.; Eskandari, H.; Scavenius, C.; Juul-Madsen, K.; Vorup-Jensen, T.; Enghild, J. J.; Sutherland, D. S., Mapping and identification of soft corona proteins at nanoparticles and their impact on cellular association. *Nature Communications* **2020,** *11* (1).
183. Loza, K.; Sengstock, C.; Chernousova, S.; Köller, M.; Epple, M., The predominant species of ionic silver in biological media is colloidally dispersed nanoparticulate silver chloride. *RSC Advances* **2014,** *4* (67), 35290.
184. Gnanadhas, D. P.; Ben Thomas, M.; Thomas, R.; Raichur, A. M.; Chakravortty, D., Interaction of Silver Nanoparticles with Serum Proteins Affects Their Antimicrobial Activity In Vivo. *Antimicrobial Agents and Chemotherapy* **2013,** *57* (10), 4945-4955.
185. Miclăuş, T.; Beer, C.; Chevallier, J.; Scavenius, C.; Bochenkov, V. E.; Enghild, J. J.; Sutherland, D. S., Dynamic protein coronas revealed as a modulator of silver nanoparticle sulphidation in vitro. *Nature Communications* **2016,** *7* (1), 11770.
186. Deng, K.; Yu, H.; Li, J. M.; Li, K. H.; Zhao, H. Y.; Ke, M.; Huang, S. W., Dual-step irradiation strategy to sequentially destroy singlet oxygen-responsive polymeric micelles and boost photodynamic cancer therapy. *Biomaterials* **2021,** *275*, 120959.
187. Midekessa, G.; Godakumara, K.; Ord, J.; Viil, J.; Lättekivi, F.; Dissanayake, K.; Kopanchuk, S.; Rinken, A.; Andronowska, A.; Bhattacharjee, S.; Rinken, T.; Fazeli, A., Zeta Potential of Extracellular Vesicles: Toward Understanding the Attributes that Determine Colloidal Stability. *ACS Omega* **2020,** *5* (27), 16701-16710.
188. Bhattacharjee, S., DLS and zeta potential – What they are and what they are not? *Journal of Controlled Release* **2016,** *235*, 337-351.
189. Mahmoudi, M.; Landry, M. P.; Moore, A.; Coreas, R., The protein corona from nanomedicine to environmental science. *Nature Reviews Materials* **2023,** *8* (7), 422-438.
190. Malinsky, M. D.; Kelly, K. L.; Schatz, G. C.; Van Duyne, R. P., Chain length dependence and sensing capabilities of the localized surface plasmon resonance of silver nanoparticles chemically modified with alkanethiol self-assembled monolayers. *Journal of the American Chemical Society* **2001,** *123* (7), 1471-1482.
191. Duan, J.; Park, K.; MacCuspie, R. I.; Vaia, R. A.; Pachter, R., Optical properties of rodlike metallic nanostructures: insight from theory and experiment. *The Journal of Physical Chemistry C* **2009,** *113* (35), 15524-15532.
192. Elghanian, R.; Storhoff, J. J.; Mucic, R. C.; Letsinger, R. L.; Mirkin, C. A., Selective colorimetric detection of polynucleotides based on the distance-dependent optical properties of gold nanoparticles. *Science* **1997,** *277* (5329), 1078-1081.

193. Peng, S.; McMahon, J. M.; Schatz, G. C.; Gray, S. K.; Sun, Y., Reversing the size-dependence of surface plasmon resonances. *Proceedings of the National Academy of Sciences* **2010,** *107* (33), 14530-14534.
194. Maccuspie, R. I., Colloidal stability of silver nanoparticles in biologically relevant conditions. *Journal of Nanoparticle Research* **2011,** *13* (7), 2893-2908.
195. Wigginton, N. S.; Titta, A. d.; Piccapietra, F.; Dobias, J.; Nesatyy, V. J.; Suter, M. J. F.; Bernier-Latmani, R., Binding of Silver Nanoparticles to Bacterial Proteins Depends on Surface Modifications and Inhibits Enzymatic Activity. *Environmental Science & Technology* **2010,** *44* (6), 2163-2168.
196. Boehmler, D. J.; O'Dell, Z. J.; Chung, C.; Riley, K. R., Bovine Serum Albumin Enhances Silver Nanoparticle Dissolution Kinetics in a Size- and Concentration-Dependent Manner. *Langmuir* **2020,** *36* (4), 1053-1061.
197. Maurer-Jones, M. A.; Mousavi, M. P. S.; Chen, L. D.; Bühlmann, P.; Haynes, C. L., Characterization of silver ion dissolution from silver nanoparticles using fluorous-phase ion-selective electrodes and assessment of resultant toxicity to Shewanella oneidensis. *Chemical Science* **2013,** *4* (6), 2564.
198. Rewak-Soroczynska, J.; Dorotkiewicz-Jach, A.; Drulis-Kawa, Z.; Wiglusz, R. J., Culture Media Composition Influences the Antibacterial Effect of Silver, Cupric, and Zinc Ions against Pseudomonas aeruginosa. *Biomolecules* **2022,** *12* (7).
199. Akram, F.; El-Tayeb, T.; Abou-Aisha, K.; El-Azizi, M., A combination of silver nanoparticles and visible blue light enhances the antibacterial efficacy of ineffective antibiotics against methicillin-resistant Staphylococcus aureus (MRSA). *Annals of Clinical Microbiology and Antimicrobials* **2016,** *15*.
200. Ye, J.; Hou, F.; Chen, G.; Zhong, T.; Xue, J.; Yu, F.; Lai, Y.; Yang, Y.; Liu, D.; Tian, Y.; Huang, J., Novel copper-containing ferrite nanoparticles exert lethality to MRSA by disrupting MRSA cell membrane permeability, depleting intracellular iron ions, and upregulating ROS levels. *Frontiers in Microbiology* **2023,** *14*.
201. Bi, Y.; Xia, G.; Shi, C.; Wan, J.; Liu, L.; Chen, Y.; Wu, Y.; Zhang, W.; Zhou, M.; He, H.; Liu, R., Therapeutic strategies against bacterial biofilms. *Fundamental Research* **2021,** *1* (2), 193-212.
202. Gebreyohannes, G.; Nyerere, A.; Bii, C.; Sbhatu, D. B., Challenges of intervention, treatment, and antibiotic resistance of biofilm-forming microorganisms. *Heliyon* **2019,** *5* (8), e02192.
203. Stewart, P. S.; William Costerton, J., Antibiotic resistance of bacteria in biofilms. *The Lancet* **2001,** *358* (9276), 135-138.
204. Teschler, J. K.; Zamorano-Sánchez, D.; Utada, A. S.; Warner, C. J.; Wong, G. C.; Linington, R. G.; Yildiz, F. H., Living in the matrix: assembly and control of Vibrio cholerae biofilms. *Nat Rev Microbiol* **2015,** *13* (5), 255-68.
205. Fong Jiunn, C. N.; Yildiz Fitnat, H., The rbmBCDEF Gene Cluster Modulates Development of Rugose Colony Morphology and Biofilm Formation in Vibrio cholerae. *Journal of Bacteriology* **2007,** *189* (6), 2319-2330.
206. Fong, J. C. N.; Syed, K. A.; Klose, K. E.; Yildiz, F. H., Role of Vibrio polysaccharide (vps) genes in VPS production, biofilm formation and Vibrio cholerae pathogenesis. *Microbiology (Reading)* **2010,** *156* (Pt 9), 2757-2769.

207. Yildiz, F.; Fong, J.; Sadovskaya, I.; Grard, T.; Vinogradov, E., Structural Characterization of the Extracellular Polysaccharide from Vibrio cholerae O1 El-Tor. *PLoS ONE* **2014,** *9* (1), e86751.
208. Meza-Villezcas, A.; Gallego-Hernández, A. L.; Yildiz, F. H.; Jaime-Acuña, O. E.; Raymond-Herrera, O.; Huerta-Saquero, A., Effect of antimicrobial nanocomposites on Vibrio cholerae lifestyles: Pellicle biofilm, planktonic and surface-attached biofilm. *PLOS ONE* **2019,** *14* (6), e0217869.
209. Gahlawat, G.; Shikha, S.; Chaddha, B. S.; Chaudhuri, S. R.; Mayilraj, S.; Choudhury, A. R., Microbial glycolipoprotein-capped silver nanoparticles as emerging antibacterial agents against cholera. *Microbial Cell Factories* **2016,** *15* (1), 25.
210. Abriat, C.; Gazil, O.; Heuzey, M.-C.; Daigle, F.; Virgilio, N., The Polymeric Matrix Composition of Vibrio cholerae Biofilms Modulate Resistance to Silver Nanoparticles Prepared by Hydrothermal Synthesis. *ACS Applied Materials & Interfaces* **2021,** *13* (30), 35356-35364.
211. Chen, K.-J.; Lee, C.-K., Twofold enhanced dispersin B activity by N-terminal fusion to silver-binding peptide for biofilm eradication. *International Journal of Biological Macromolecules* **2018,** *118*, 419-426.
212. Fanaei Pirlar, R.; Emaneini, M.; Beigverdi, R.; Banar, M.; B. Van Leeuwen, W.; Jabalameli, F., Combinatorial effects of antibiotics and enzymes against dual-species Staphylococcus aureus and Pseudomonas aeruginosa biofilms in the wound-like medium. *PLOS ONE* **2020,** *15* (6), e0235093.
213. Weldrick, P. J.; Hardman, M. J.; Paunov, V. N., Enhanced Clearing of Wound-Related Pathogenic Bacterial Biofilms Using Protease-Functionalized Antibiotic Nanocarriers. *ACS Applied Materials & Interfaces* **2019,** *11* (47), 43902-43919.
214. Daboor, S. M.; Rohde, J. R.; Cheng, Z., Disruption of the extracellular polymeric network of Pseudomonas aeruginosa biofilms by alginate lyase enhances pathogen eradication by antibiotics. *Journal of Cystic Fibrosis* **2021,** *20* (2), 264-270.
215. Chen, Z.; Ji, H.; Liu, C.; Bing, W.; Wang, Z.; Qu, X., A Multinuclear Metal Complex Based DNase-Mimetic Artificial Enzyme: Matrix Cleavage for Combating Bacterial Biofilms. *Angewandte Chemie International Edition* **2016,** *55* (36), 10732-10736.
216. Tetz, G. V.; Artemenko, N. K.; Tetz, V. V., Effect of DNase and Antibiotics on Biofilm Characteristics. *Antimicrobial Agents and Chemotherapy* **2009,** *53* (3), 1204-1209.
217. Zhao, T.; Liu, Y., N-acetylcysteine inhibit biofilms produced by Pseudomonas aeruginosa. *BMC Microbiology* **2010,** *10* (1), 140.
218. Miller, K. P.; Wang, L.; Benicewicz, B. C.; Decho, A. W., Inorganic nanoparticles engineered to attack bacteria. *Chemical Society Reviews* **2015,** *44* (21), 7787-7807.
219. Li, X.; Yeh, Y.-C.; Giri, K.; Mout, R.; Landis, R. F.; Prakash, Y. S.; Rotello, V. M., Control of nanoparticle penetration into biofilms through surface design. *Chemical Communications* **2015,** *51* (2), 282-285.
220. Gupta, A.; Landis, R. F.; Li, C.-H.; Schnurr, M.; Das, R.; Lee, Y.-W.; Yazdani, M.; Liu, Y.; Kozlova, A.; Rotello, V. M., Engineered Polymer Nanoparticles with Unprecedented Antimicrobial Efficacy and Therapeutic Indices against Multidrug-Resistant Bacteria and Biofilms. *Journal of the American Chemical Society* **2018,** *140* (38), 12137-12143.
221. Duncan, B.; Li, X.; Landis, R. F.; Kim, S. T.; Gupta, A.; Wang, L.-S.; Ramanathan, R.; Tang, R.; Boerth, J. A.; Rotello, V. M., Nanoparticle-Stabilized Capsules for the Treatment of Bacterial Biofilms. *ACS Nano* **2015,** *9* (8), 7775-7782.

222. Qayyum, S.; Khan, A. U., Nanoparticles vs. biofilms: a battle against another paradigm of antibiotic resistance. *MedChemComm* **2016,** *7* (8), 1479-1498.
223. Hiebner, D. W.; Barros, C.; Quinn, L.; Vitale, S.; Casey, E., Surface functionalization-dependent localization and affinity of SiO2 nanoparticles within the biofilm EPS matrix. *Biofilm* **2020,** *2*, 100029.
224. Dunsing, V.; Irmscher, T.; Barbirz, S.; Chiantia, S., Purely Polysaccharide-Based Biofilm Matrix Provides Size-Selective Diffusion Barriers for Nanoparticles and Bacteriophages. *Biomacromolecules* **2019,** *20* (10), 3842-3854.
225. Rodríguez-Suárez, J. M.; Butler, C. S.; Gershenson, A.; Lau, B. L. T., Heterogeneous Diffusion of Polystyrene Nanoparticles through an Alginate Matrix: The Role of Cross-linking and Particle Size. *Environmental Science & Technology* **2020,** *54* (8), 5159-5166.
226. Feoktistova, M.; Geserick, P.; Leverkus, M., Crystal Violet Assay for Determining Viability of Cultured Cells. *Cold Spring Harb Protoc* **2016,** *2016* (4), pdb.prot087379.
227. Körstgens, V.; Flemming, H.-C.; Wingender, J.; Borchard, W., Influence of calcium ions on the mechanical properties of a model biofilm of mucoid Pseudomonas aeruginosa. *Water science and technology : a journal of the International Association on Water Pollution Research* **2001,** *43*, 49-57.
228. Wloka, M.; Rehage, H.; Flemming, H. C.; Wingender, J., Rheological properties of viscoelastic biofilm extracellular polymeric substances and comparison to the behavior of calcium alginate gels. *Colloid and Polymer Science* **2004,** *282* (10), 1067-1076.